All Wired Up: An Exploration of the Electrical Properties of Microtubules and Tubulin

by
Aarat Pratyaksh Kalra

A thesis submitted in partial fulfillment of the requirements for the degree of
Doctor of Philosophy

Department of Physics
University of Alberta

Abstract

Microtubules are hollow, cylindrical polymers of the protein α, β tubulin, that interact mechano-chemically with a variety of macromolecules. Due to their mechanically robust nature, microtubules have gained attention as tracks for precisely directed transport of nanomaterials within lab-on-a-chip devices. Largely because of the unusually negative charge on the tail-like C-termini of tubulin, recent work demonstrates that these biopolymers are also involved in a broad spectrum of intracellular electrical signaling.

This thesis discusses the electrochemical properties of microtubules. Impedance spectroscopy was used to measure the impedance of microtubule networks at physiologically relevant tubulin concentrations. While polymerized microtubules increased solution capacitance, it was seen that unpolymerized tubulin at the same concentrations did not. This work indicates the role of microtubules as potential intracellular ion storage devices.

Next, we aimed to understand how tubulin and microtubules respond to the presence of dimethyl sulfoxide (DMSO), a solvent commonly used in the fabrication of organic optoelectronic devices. Dynamic light scattering (DLS) and fluorescence microscopy showed that the effective size of tubulin increases in the presence of increasing DMSO volume fractions due to the formation of oligomers. In the presence of >80 % DMSO however, zeta potential experiments showed that tubulin reversibly acquired a net positive charge, causing it to form two-dimensional sheets and aggregates instead of cylindrical microtubules. Fluorescence microscopy showed that tubulin sheets and aggregates co-localize with g-C_3N_4 sheets while microtubule do not, further verifying the presence of a positive surface charge. This study

illustrates that tubulin and its polymers, in addition to being mechanically robust, are also electrically tunable. These findings indicate the utility of DLS for monitoring early-state microtubule polymerization and tubulin oligomerization. Experiments in the future, using different contact geometries can be used to determine the solid-state properties of microtubules, and their properties in different solvents, for applications within electrically oriented nanodevices.

Preface

The work presented here was completed at the Department of Physics of the University of Alberta. This thesis is based on material that was previously published.

Chapter 2 of this thesis has published as a review article, Kalra Aarat P., Eakins Boden B., Patel Sahil D., Rezania Vahid, Tuszynski Jack A., Shankar Karthik. "All Wired Up: An Exploration of the Electrical Properties of Microtubules and Tubulin." *ACS Nano* (2020). I designed and wrote the manuscript. Boden B. Eakins and Sahil D. Patel contributed to manuscript edits. Karthik Shankar and Jack A. Tuszynski were supervisory authors.

Chapter 3 has been published as a research article, Kalra, Aarat P., Patel Sahil D., Bhuiyan Asadullah F., Jordane Preto, Scheuer Kyle G., Mohammed Usman, Lewis John D., Rezania Vahid, Shankar Karthik, and Tuszynski Jack A. "Investigation of the Electrical Properties of Microtubule Ensembles under Cell-Like Conditions." *Nanomaterials* 10, no. 2 (2020): 265. I was responsible for experimental design, data collection, analysis of results and manuscript composition. Sahil D. Patel and Asadullah F. Bhuiyan assisted with the data collection and contributed to manuscript edits. Jordane Preto and Vahid Rezania provided theoretical insight and edited the manuscript. Karthik Shankar and Jack A. Tuszynski were supervisory authors.

Chapter 4 has been published as a research article, Kalra, Aarat P., Kar Piyush, Preto Jordane, Rezania Vahid, Dogariu Aristide, Lewis John D., Tuszynski Jack A., Shankar Karthik. "Behavior of α, β tubulin in DMSO-containing electrolytes." *Nanoscale Advances* 1, no. 9 (2019): 3364-3371. I was responsible for experimental design, data collection, analysis of results and manuscript composition. Piyush Kar assisted with the data collection and

contributed to manuscript edits. Jordane Preto performed simulations shown in Figure 4.3 and the results shown in Table 4.2. Jordane Preto and Vahid Rezania provided theoretical insight and edited the manuscript. Jack A. Tuszynski and Karthik Shankar were supervisory authors.

Chapter 5 has been published as a research article, Kalra Aarat P., Patel Sahil D., Eakins Boden B., Riddell Saralyn, Kumar Pawan, Winter Philip, Preto Jordane, Carlson Kris W., Lewis John D., Rezania Vahid, Tuszynski Jack A., Shankar Karthik. "Revealing and attenuating the electrostatic properties of tubulin and its polymers" *Small* 2003560 (2020). I was responsible for experimental design, performing all experiments, analysis of results and manuscript composition. Sahil D. Patel performed simulations shown in Figure 5.1f. Boden Eakins performed simulations shown in Figure 5.3b. Sahil D. Patel and Boden B. Eakins assisted with the data collection and contributed to manuscript edits. Karthik Shankar and Jack A. Tuszynski were supervisory authors.

To my mother, for her infinite love

The genius thing we did was, we didn't give up.

Jay Z

Acknowledgements

First of all, I would like to thank my supervisor, Prof. Jack Tuszynski, for his outstanding mentorship. My Ph.D. has been a wonderful experience, largely due to his leadership style. Prof. Tuszynski has been a strong role model for me, and I hope that I too, will one day be as good a scientist and human being as him. Prof. Karthik Shankar, my co-supervisor, offered brilliant expertise and excellent guidance. His tireless answering of all my questions helped me make the difficult transition from biology to physics. I profusely thank Prof. Vahid Rezania and Prof. Al Meldrum, members of my Supervisory Committee, for extending their full support whenever I required it, gradually becoming extensions of my supervisors. I am extremely grateful too, to Prof. Frank Hegmann, who taught a wonderful course that introduced me to Condensed Matter systems and, in so doing, monumentally broadened my horizons. I thank Prof. Roger Penrose, for spending a large amount of time with me, discussing microtubule biophysics. These discussions with him greatly inspired me and motivated me to work harder. I must also acknowledge the financial support I have received from Alberta Innovates and the University of Alberta Graduate Students' Association.

My work was made enjoyable, in large part due to the company of Sahil Patel, who experimented alongside me for three years. Several late-night discussions, Skype conversations and coffee sessions were spent with us discussing 'important' details such as the best colors to make diagrams and figures in, writing styles and job applications! His work ethic and positive personality were deeply motivating and inspiring. Boden Eakins, Asadullah Bhuiyan and Jack Xiao helped me greatly with experiments for which I offer them my profuse thanks. I am grateful to Philip Winter and Sara Omar for enduring me during my first few months in Alberta,

and listening to my rants about administrative problems as a new graduate student. My time in Edmonton was made extremely pleasant by the cheerful and family-like atmosphere of the lab. For this, my deepest gratitude to Ajay Manuel, Clayton Bell, Sahar Arbabimoghadam, Ehsan Vahidzadeh, Saralyn Riddell, Francesco Gentile, Ujwal Thakur, Prakash Bhandari, Maral Aminpour, Ryan Kisslinger, Arun Raturi, Najia Mahdi, Mahshad Moshari and Piyush Kar. I will miss their company. During my graduate studies, Dr. Zeev Bomzon was always willing to help with any manuscripts that had to be reviewed and gave me useful life advice that immensely motivated me, and that I will always adhere to. Dr. Bomzon went as far as arranging a postdoctoral fellowship for me at a world-renown university, an act that I will forever cherish. Drs. Jordane Preto and Pawan Kumar were go-to people when I faced experimental problems and never failed me; I thank them from the bottom of my heart.

Finally, I offer my thanks and apologies to my family back home, for bearing outbursts on everything from the unavailability of vegetarian food in Edmonton to its long and snowy winters. My father, himself a professor of Electrical Engineering, offered unswerving support, often interrogating me with physics-related questions which, though highly frustrating at the time, helped improved my basics. His charismatic persona inspires me tremendously. My siblings Amolak and Amrita could always be relied upon to provide unhelpful advice and many laughs. My older sister Dr. Saatviki Gupta mentored me with my first paper and showed me how to present and write in an academic setting. I am greatly indebted to my paternal uncle and aunt, Mr. Saran Kumar Kalra and Mrs Girija Kalra, who allowed me to stay with them in Agra for two years during my undergraduate research. I would also like to thank Prof. Dayal Pyari Srivastava of the DEI Department of Physics for her support, advice and great kindness. Dr. Shiroman Prakash, who was part of our household at IIT Kanpur and has been a profound influence and role model. And finally, my mother, who has always held me to the highest of standards and who I am eternally indebted to.

Table of Contents

List of Tables

List of Figures

List of Abbreviations

MT	Microtubule
MAP	Microtubule Associated Protein
P4VB	Dineopentoxyl-phenylenedivinylene
TBA	Tubulin-binding agent
DMSO	Dimethyl sulfoxide
GTP	Guanosine triphosphate
GDP	Guanosine diphosphate
GMPCPP	guanylyl-(a,b(3)-methylene-diphosphonate
EB1	End-binding protein 1
CNT	Carbon nanotube
ATP	Adenosine triphosphate
OLED	Organic Light Emitting Diode
OPV	Organic Photovoltaics
MCAK	Mitotic centromere-associated kinesin
G-C_3N_4	Graphitic carbon nitride
DLS	Dynamic Light Scattering
ZP	Zeta potential
TTField	Tumour treating electric fields
EMCCD	Electron multiplying charge coupled device
ISFET	ion-sensitive field-effect transistor
SPM	Scanning probe microscopy
LBM	lipid bilayer membranes
RIE	Reactive ion etching
nsEP	Nanosecond Electropulses
BRB80	Bradley's reconstitution buffer with 80 mM PIPES
PDB	Protein data bank
EGTA	Ethylene glycol tetra-acetic acid
PIPES	Piperazine-N,N′-bis(2-ethanesulfonic acid)
FTO	Fluorine doped Tin Oxide

1. Introduction

Eukaryotic cells host a diverse array of macromolecules that interact with each other to continually undergo changes in structure and composition. While the biochemical interactions of these macromolecules, with each other and with externally introduced perturbations, are the subject of extensive research, their electrical properties have only recently gained considerable interest.

This interest in the electrical properties stems from several reasons: Understanding the electrical properties of biological materials will bolster efforts in designing biocompatible devices. Indeed, the performance of devices such as OLEDs (Organic Light Emitting Diodes) [1] and OPVs (Organic Photovoltaics) [2] has already been shown to be enhanced by the presence of biomaterials [3]. The utilization of biologically sourced materials within the electronics industry will allow the fabrication of biodegradable devices. Finally, a deeper understanding of the electrical interactions between biomacromolecules will enable the development of modalities that target disease-treatment. Indeed, recent examples of such an approach include the utilization of electric fields to reduce the spread of cancer [4]. While such applications are clearly exciting, a deeper understanding of the electrical underpinnings of biomacromolecules will shed light on further roles that they could play in the future of both nanoelectronics and nanomedicine.

This thesis focuses on microtubules – filamentous, 25 nm wide polymers composed of the globular protein α, β-tubulin that play a variety of roles within eukaryotic cells. Microtubules are crucial for cell function, forming the mechanical core of cilia and flagella, [5-6] preparing cues for intracellular organelle positioning, [7-8] providing forces required for proper chromosomal segregation [9] and forming a network of tracks for intracellular macromolecular transport. [10-11] The highly negative electrostatic charge (~50 *e*) and large dipole moment (3500-4000 D depending on the isotype) of tubulin allow microtubules to play unexpected electrical roles within the cell which will be discussed in the thesis. [12] For example, the presence of microtubule networks in solution has been shown to increase capacitance, [13] individual microtubules have been displayed to act as amplifiers of ionic signals *in Vitro*, [14-15] are modelled to act as intracellular nanowires capable of propagating ionic signals along their length [16-17] and have been proposed to regulate ciliary 'beating' movement through cation-

based interactions with microtubule associated proteins. [18] Both simulations and experimental observations suggest that their interesting electrical properties enable them to act as good conduits for the transmission of electrical information within the cell. This thesis shows expands on previous work, showing that unlike unpolymerized tubulin, microtubules increase solution capacitance at physiologically relevant tubulin concentrations and ionic strengths. This work also displays both biochemical and electrical responses of tubulin to the presence of DMSO in solution. Thus, this work attempts to cover gaps in our understanding of the electrical properties of tubulin and microtubules, while also seeking the potential utilization of these nanostructures within devices. Such work will help develop tubulin-based nanoscale devices in the future. While it is now clear that the interactions of microtubules with MAPs and tubulin-interacting drugs alter their electrical properties, [19-21] future work should examine how counterionic condensation around these biopolymers can be altered through bulk solution properties such viscosity, ionic strength and macromolecular crowding. Understanding the interplay between MAP binding, ionic interactions, microtubules and electric fields within the cell will, in addition to being useful from a fundamental science standpoint, also be beneficial for prospective medical applications.

This thesis is based on articles that have either been published or are in the process of being published. Chapter 2 presents a systematic review of recent literature on the electrical properties of microtubules. Chapter 3 reports my work on the experimental determination of microtubule network capacitance. With a view to utilize tubulin within electronic devices, Chapter 4 attempts to determine the biochemical response of tubulin to increasingly large DMSO volume fractions. In Chapter 5, work to determine the electrical properties of tubulin and microtubules in DMSO containing solutions is reported. The thesis concludes with Chapter 6, which is a brief overview of the research results presented in my Ph.D. and presents preliminary data to determine the local pH around microtubules and tubulin. Future directions of work are also discussed in Chapter 6.

2. An overview of the bioelectrical properties of microtubules and tubulin[1]

ABSTRACT

Microtubules are hollow, cylindrical polymers of the protein α, β tubulin, that interact mechano-chemically with a variety of macromolecules. Due to their mechanically robust nature, microtubules have gained attention as tracks for precisely directed transport of nanomaterials within lab-on-a-chip devices. Primarily due to the unusually negative tail-like C-termini of tubulin, recent work demonstrates that these biopolymers are also involved in a broad spectrum of intracellular electrical signaling. Microtubules and their electrostatic properties are discussed in this review, followed by an evaluation of how these biopolymers respond mechanically to electrical stimuli, through microtubule migration, electro-rotation and C-termini conformation changes. Literature focusing on how microtubules act as nanowires capable of intracellular ionic transport, charge storage, and ionic signal amplification is reviewed, illustrating how these biopolymers attenuate ionic movement in response to electrical stimuli. The review ends with a discussion on the important questions, challenges and future opportunities for intracellular microtubule-based electrical signaling.

INTRODUCTION

Microtubules (MTs) are slender pipe-like polymers of the protein α, β-tubulin, that form a network of tracks for intracellular macromolecular transport. They establish morphological transitions during neuronal development and exert synchronized mechanical pulling forces for chromosomal segregation during mitosis. Interacting closely with actin filaments and intermediate filaments, MTs form a network of cooperating polymers known as the

[1] This chapter was published as a review article, Kalra Aarat P., Eakins Boden B., Patel Sahil D., Rezania Vahid, Tuszynski Jack A., Shankar Karthik. "All Wired Up: An exploration of the electrical properties of microtubules and tubulin." *ACS Nano* (2020).

cytoskeleton, which provides mechanical support for the maintenance of cell shape and rigidity.

A MT has a cylindrical structure consisting of 13 vertically stacked columns (protofilaments) of tubulin dimers assembled in a head-to-tail manner, resulting in a 15 nm wide hollow core known as the lumen, and a 25 nm wide outer diameter (Figure 1a). Freely diffusing GTP (guanosine triphosphate)-bound tubulin dimers (GTP-tubulin) in solution are assembly-competent and bind to a protofilament end, causing MT elongation. GTP-tubulin dimers that bind to the MT end are incorporated into the so-called MT lattice and eventually hydrolyze GTP bound to the b-monomer into GDP (guanosine diphosphate) while GTP bound to the a-monomer does not hydrolyze to GDP. The hydrolysis of GTP-tubulin to GDP-tubulin is thought to induce mechanical strain causing a conformational change, which results in abrupt MT shortening ('catastrophe'). Catastrophes involve tubulin oligomers 'peeling off' protofilament ends, sometimes leading to complete MT disassembly. Following a catastrophe, re-elongation events ('rescue') restart MT growth until another catastrophe occurs, leading MTs to exist in a state of dynamic instability. [22-24] Within a cell, dynamic instability is tightly regulated by families of microtubule-associated proteins (MAPs). The MAP tau, for example, is a wire-like protein that links several tubulin dimers within a protofilament or between neighboring MTs (*e.g.* in a neuronal cell) and stabilizes MTs against catastrophe.[25-26] The MAP MCAK (mitotic centromere-associated kinesin) however, has the opposite function: MCAK molecules cause MT shortening by unbinding GTP-tubulin from the MT end.[27] While MAPs control the ratio of polymerized and unpolymerized tubulin within the cell, it is worth noting that not all MAPs attenuate dynamic instability. Kinesin-1 (henceforth referred to as kinesin), for example, utilizes energy from ATP (adenosine triphosphate) hydrolysis to 'walk' in a processive manner along the outer MT surface toward the plus (growing) end of a MT while transporting organelles such as mitochondria across the cell. While one end of kinesin (the motor 'head' domain) interacts with tubulin and hydrolyses ATP, the other end (the 'tail' domain) interacts with the cargo macromolecule.[28-29] Several drugs and anesthetic molecules also bind to tubulin, mimicking the action of MAPs. The binding of the chemotherapeutic agent paclitaxel, for example, leads to dramatically increased MT nucleation and structural stability.[30-31] The action of laulimalide, an investigational cancer chemotherapeutic agent,[32] also achieves a similar effect. On the other hand, the introduction of colchicine, which is used as an oral treatment for gout,[33] leads to inhibition of tubulin binding at the MT end, resulting in destabilization of the MT network.[34] Together, MAPs and drugs that interact with tubulin

(collectively called tubulin binding agents, or TBAs) form a diverse set of chemical agents that modulate MT interactions with the rest of the cell.

Several intracellular roles of MTs, such as scaffolding, macromolecular cargo transport and force generation for chromosomal segregation, rely on their mechanical properties: The persistence length of a MT is estimated to be between 1 and 10 mm,[35] indicating that they are approximately 100 times stiffer than actin filaments and, especially, intermediate filaments,[36] while their longitudinal Young's modulus is 1-5 GPa, similar to that of rigid plastics.[37-39] The high stiffness of these biopolymers has prompted comparisons to carbon nanotubes (CNTs), which have comparable dimensions.[40] Similar to CNTs, MTs *in Vitro* can be chemically conjugated to a variety of macromolecules, including synthetic proteins, quantum dots,[41] and magnetic nanoparticles.[42] The ease of labelling MTs with chemical agents, the intracellular abundance of tubulin, the high mechanical strength of MTs, the directionality of kinesin-based transport and the ready formation of MTs at room temperature have prompted a thrust to develop highly controllable mechanically-based MT nanodevices.[35, 43] Several transport devices that utilize MT-kinesin systems, such as photolithography-based 'rectifiers'[44-45] and 'concentrator' devices[46] have already been fabricated, with the goal of overcoming obstacles posed by the 'big fingers' of nanotechnological instrumentation, [47] (Figure 3 c, d). However, due to the cumbersome nature of the lithographic process, optical and chemical techniques to control MT transport are also being explored.[48-50] In the past few years, MTs have also found use as transporters on non-topographical surfaces,[48] three-dimensional microstructures such as bridges and pillars, [51-52] and inside larger inorganic tubes (as a 'tube within a tube'; Figure 3 e).[53] In a 'tube within a tube' the outer inorganic tubes have tunable dimensions, which present a promising potential as MT-based guides for directional transport. The mechanical strength of MTs has enabled their use in force-meters[54] and stiff substrates atop which CNT gliding can take place.[55] Larger MT-based superstructures (such as MT loops, asters and tori) have also been assembled, with potential use as nanopatterning agents (Figure 3 f).[56-57] Kinesin-driven MT transport has also been used to solve nondeterministic-polynomial-time (NP)-complete problems, which are encoded in an all-on-chip platform, providing a lower energy consumption and heat dissipation compared to other parallel computing approaches, including DNA computation, quantum computation, and microfluidic-based computation.[58] The kinesin-MT system is thus viewed as a promising biodegradable (and potentially biocompatible) tool for the future of nanofluidics.

MTs have interesting electrical properties that have only recently begun to be utilized in molecular devices. Electrostatically, a tubulin dimer carries a bare (vacuum) charge of – 52 *e* under physiological pH (from the 3RYF structure), about 46 % (– 24 *e*) of which is localized at the tail-like C-termini attached to each monomer (Figure 2.1 b, c). This charge is conferred by aspartic- and glutamic acid residues, which together constitute approximately 49 % of the C-termini amino acid sequences (Figure 2.1 d). Due to this skewed charge distribution, each monomer acquires a permanent dipole moment of approximately 4000 D (Figure 2.1 c). Within a MT, the radially symmetric arrangement of tubulin amplifies the protein dipole moment, especially its longitudinal component (Figure 2.1 a), causing MTs to acquire electrostatic polarity, predominantly along the MT axis, and a length-dependent net dipole moment.

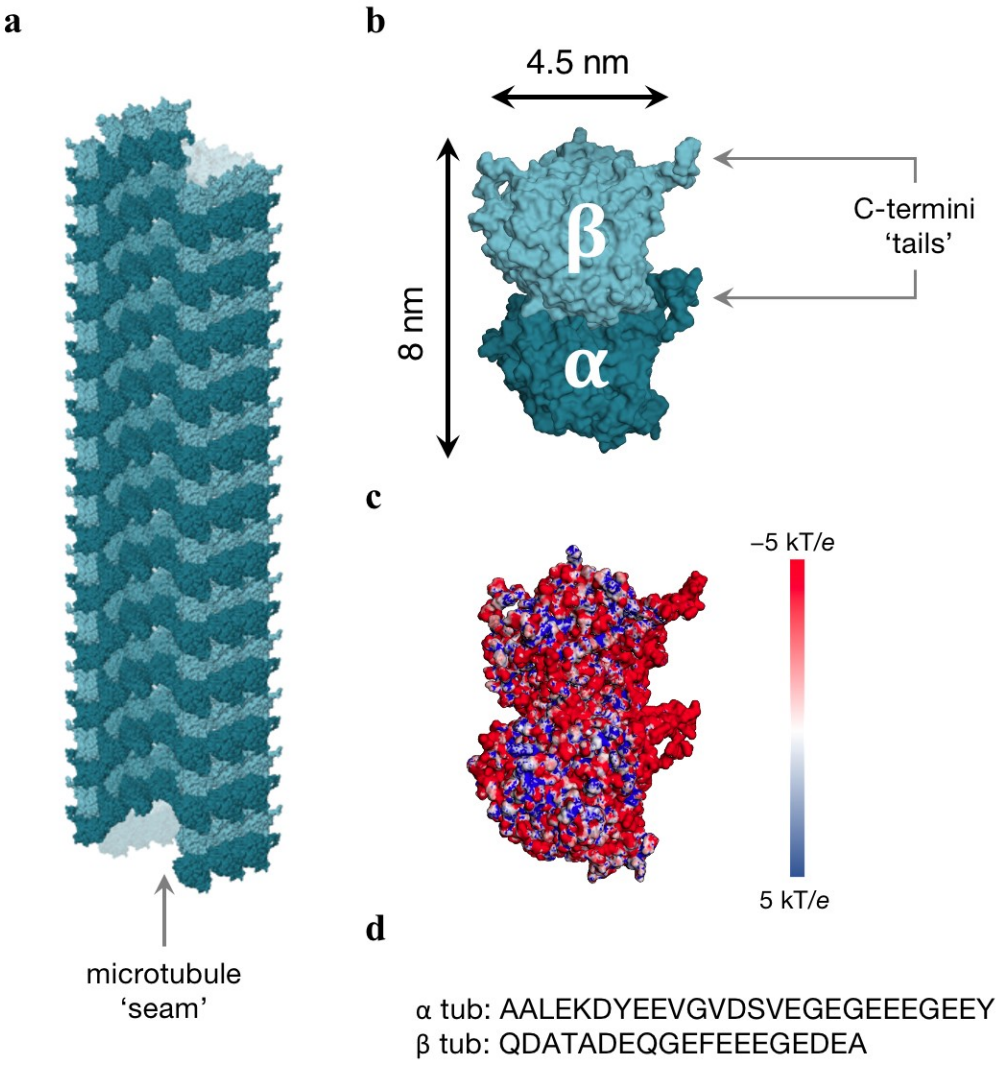

Figure 2.1. (a) The structure of MTs, displaying its cylindrical cross section and head to tail arrangement of tubulin dimers. (b) The structure of a tubulin dimer, showing C-termini tails, adapted from protein sequence 3RYF.59 (c) An electrostatic map of

tubulin, displaying the spatial distribution of negatively charged residues on the surface (c) An electrostatic map of tubulin showing its dipole moment. Image created using APBS and PDB2PQR software.60-61 (d) The amino acid sequence of the C-termini tails in the α (26 residues) and β (19 residues) subunits of tubulin as represented by homology modelling of 3RYF. In the 3RYF tubulin sequence, Aspartic acid (D) and Glutamic acid (E) together constitute 48.9 % of the C-termini amino acid sequence.

Recent efforts to fabricate nanodevices that utilize the interesting and highly unusual electrical properties of tubulin show great promise for bio-nanotechnology.[62-63] By comparison, a better understanding of the electrical properties of biomaterials such as melanin and DNA have enabled their utilization in devices such as OLEDs and solar cells.[1, 3] However, due to the lack of understanding of MT bioelectricity, extension from such devices has not been possible as of yet. However, MTs and tubulin have been modeled to act as targets for the action of electric-field based cancer treatment and wound healing modalities.[64-68] Indeed, if the potential of MTs as biological analogues of CNTs is to be explored, a thorough examination of their responses to electrical stimulation will be required.

Historically, when they were imaged in live cells in 1953, MTs were considered important for chromosomal movement in cell division.[69] With findings from the 1960s and 1970s based on the successful *in Vitro* purification of tubulin,[70-71] showing that taxol had a MT stabilizing effect,[31] and that the C-termini tails were highly acidic,[72-73] the electrical properties of MTs gradually came into focus. While there were indications that MTs and tubulin interacted in a nontrivial manner with external electric fields,[74-75] the intracellular significance of their electrical properties, and its device potential remained poorly understood. However, by the turn of the millennium, as nanofabrication and device miniaturization attained industrial relevance, MTs began being noticed as potential macromolecular transport devices.[76] An all-atom simulation allowed the mapping of the electrostatic potential and showed the difference in electrostatic potential between the plus and minus ends of a MT.[60] Subsequently, MTs have been experimentally and theoretically shown to play important roles such as charge storage and transport within physiologically relevant environments.[14, 77-78] While their high mechanical stability has led to their utilization in a variety of nanodevices, their interesting electrical properties have found use within sorters and direction-specific transport.[45, 62-63, 79-80] More recently, MTs have been discussed as molecular targets for treatment modalities based on electric fields.[4, 64, 67-68, 81] In the future, undoubtedly more work will be devoted to their

utilization within nanodevices outside the cell, as well as their roles as targets for electrically based disease treatment.

This review showcases the state of the field in MT electrical properties, reviewing both applications within nanodevices as well as potential roles within the cell. While emphasis is placed on recent findings and illustrating the directions of future work, historically important work has also been pointed out to provide chronological perspective.

MICROTUBULES AS INTRACELLULAR SENSORS

The utilization of MT-based transport nanodevices has largely been realized through kinesin-conjugated migration. The macromolecule to be transported is first conjugated to kinesin, after which perfusion of the macromolecule-kinesin construct onto a MT-coated substrate is performed, causing kinesin's processive movement, or 'gliding' on MT tracks.[57, 82-84] A reversed configuration can also be used, in which the substrate is coated with kinesin molecules attached by their tail domains, while their MT-interacting head domains are exposed to solution (Figure 2.2 a, b). Upon the perfusion of MTs into the chamber, the exposed head domains bind to tubulin, causing ATP to hydrolyze and kinesin to 'step' forward. This leads to MT movement on the kinesin-coated substrate, eventually resulting in the desired macromolecular migration.

Irrespective of its configuration, each MT moves in a random direction governed by the Brownian motion of its tip on a kinesin-coated substrate. Thus, transport of cargo in one specific direction is hard to achieve and has been an area of focused research over the last two decades. The application of an external electric field resolves this hurdle, causing the highly negative MT tip to orient along electric field lines, causing mechanical deflection and migration of the entire MT.[45, 85] This behavior was utilized to create rectifiers capable of transporting gold nanowires across tens of micrometers,[85] and sorting devices with accuracies in excess of 90 % for kinesin-driven MTs steering under one-dimensional electric fields (Figure 2.3 a, b).[79-80] The use of MT electrostatics to tune their mechanical response in accordance with the requirements of the nanosystem adds immense versatility. For example, the electrostatic charge on a MT tip was successfully controlled by labelling it with double-stranded DNA, the presence of which resulted in significantly different radii of curvature, depending on the size of DNA used for labelling.[63]. A recent study created a MT-based sorting device on a kinesin-coated glass substrate to study MTs polymerized in the presence of a slowly-hydrolyzable GTP-analogue

(GMPCPP[86]), which are known to be stiffer than those polymerized in the presence of GTP (Figure 2.3 e). The authors subsequently managed to sort a mixture of GMPCPP and GTP polymerized MTs using non-uniform electric fields, based on the extent to which they bent.[62-63] To explore the potential of electrically based MT transport devices, a deeper understanding of the response of kinesin processivity in the presence of a wide variety external electric field parameters is required.

Device fabrication based on the mechanical response of MTs to electric fields has also enabled insights into their electrical properties (such as electrophoretic mobility and zeta potential) which have been shown to depend strongly on buffer conditions (pH and ionic strength).[87] Due to extensive counterionic condensation on the MT surface, the effective charge per tubulin (including surfaces that are incorporated into the MT wall) when it is within the MT lattice, is much lower than the bare tubulin charge of – 52 *e* at pH 6.9. Measurements of the electrophoretic mobility of MTs (values shown in Table 1) have allowed for calculation of the effective charge of a dimer in a MT to be – 23 ± 2 *e* under physiological conditions.[79] Earlier publications reported measured tubulin mobilities (values also shown in Table 1) but concluded that the effective charge of tubulin was only – 12 ± 2 *e*[80] or even as low as – 0.2 *e* [87-88] under physiological conditions. However, the calculation of –12 ± 2 *e* uses a simplistic model for the MT geometry and the calculation of – 0.2 *e* neglects the retardation effect (the additional drag force caused by positive counter-ions around, but not condensed on, the MT) and considers MT motion to be hydrodynamic.[87-88] Therefore, counterionic condensation should be considered to screen roughly half of the bare charge of a MT. Interestingly, the effective charge is higher when a tubulin dimer is within the MT lattice as opposed to when it is in solution, indicating that tubulin polymerization alters its electrostatic charge distribution, and that free tubulin in solution is electrically distinct from that embedded within the MT lattice (as polymerized tubulin). Also, the isoelectric point of tubulin within a MT was measured to be pH 4.2;[87] however previous experiments showed that the isoelectric point of free tubulin is slightly above pH 5.[89-90] Such findings indicate the importance of the tubulin polymerization state *i.e.* free tubulin as opposed to that within a MT lattice (polymerized tubulin) on its biophysical characteristics. Future work will quantify how the polymerization state of tubulin changes the concentration of free ions and the electrical properties of a solution containing tubulin.

A multitude of mechanical responses to electrical signals result from the length-dependent dipole moment of a MT. Early indications of this dipole moment came when, upon exposing a solution containing unpolymerized tubulin dimers to a.c. electric fields (10 Hz, 25 mV/cm), MT formation along electric field lines of force was observed.[75] The existence of a permanent dipole moment was confirmed when MTs that were initially oriented in random directions on a glass substrate re-oriented when exposed to d.c. electric fields.[91] Successful electro-rotation of MTs in the presence of a.c. electric fields (200 kHz-2 MHz, $< 2.1 \times 10^5$ V m^{-1}) highlighted the significance of induced dipoles present within a MT. Induced dipoles were reported in response to external electric fields as resulting from a shift either in the electron densities in the tubulin dimer or in the counterion distribution condensed around the MT surface. Thus, an induced dipole, as well as the MT's permanent dipole, need to be considered when analyzing motion where alternating electric fields are present in the sample with tubulin or MTs.

Many of the interesting electrical properties of MTs are a result of the brush-like C-termini tails, which are about 4 nm in length (when fully stretched out) and protrude from the outer MT surface. At physiological pH values, each tail adopts a stretched random coil conformation, extending outwards into the solution, due to electrostatic repulsion among their constituent negatively charged amino acids (Figure 2.5 a, b[95]) and away from the mainly negatively charged surface of a MT. As the solution's pH is lowered, amino acid protonation leads to a decrease in the absolute charge, causing the tail to bend inwards with parts of it forming helical motifs.[96-97] Even local temperature changes can supply enough thermal energy to cause C-termini conformational changes; these result in the C-termini mechanically oscillating like a 'jack-in the-box'.[73] The presence of C-termini increases electrostatic repulsion between (otherwise less negative) neighboring tubulin dimers, lowering MT elongation rates. At lower pH values, favoring of the kinked conformation and amino acid protonation results in a reduction in the electrostatic repulsion between neighboring tubulin causing an enhancement of MT elongation.[98]

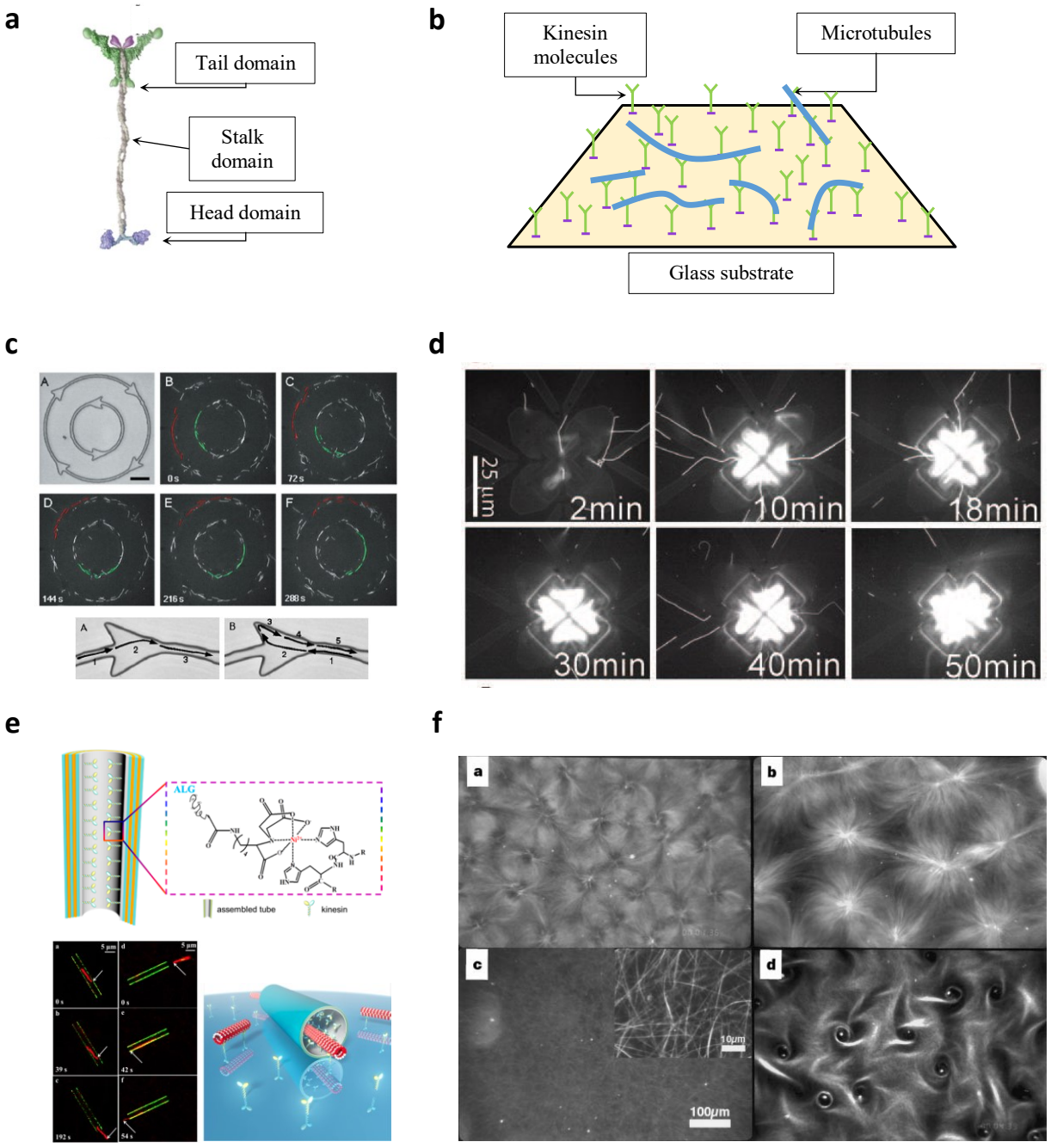

Figure 2.2. MTs as nature's mesoscale devices. (a) The structure of kinesin, displaying the three functional domains. The head domain binds to tubulin, whereas the tail domain interacts with the cargo macromolecule to be transported. The head and tail domains are connected by the Stalk domain. Reproduced with permission from ref 92. Copyright 2003 Elsevier B. V. (b) MTs (blue rod-shaped structures) are transported by the collective action of kinesins (green 'Y' shaped structures). (c) A MT-based rectifier device shows that the direction of MT gliding can be dictated using photolithographically etched, arrow-shaped patterns in the photoresist SAL600.

Reproduced with permission from ref 44. Copyright 2001 Biophysical Society. (d) A MT concentrator device can be used to focus MT gliding into a pre-determined area through the use of several rectifier devices. Reproduced with permission from ref 46. Copyright 2014 American Chemical Society. (e) Transporting MTs as a 'tube within a tube' through kinesin-coating on the inner wall of inorganic nanotubes. Reproduced with permission from ref 53. Copyright 2014 American Chemical Society. (f) Kinesin-MT interactions can lead to a variety of structures. Reproduced with permission from ref 56. Copyright 1997 Nature publishing group.

Quantity	**Value**
Tubulin bare charge at pH 6.9	– 52 *e*
Tubulin effective charge in MT	– 23 ± 0.2 *e* [79]
Relative permittivity of tubulin	3.5251 ± 0.861 [93]
Polarizability of tubulin	7×10^{-34} C.m^2/V [93]
Effective tubulin dipole moment in MT (MT length 5 μm, along the MT length)	2.8 Debye [91]
Overall MT induced dipole moment (MT length 3.5 μm; along the MT length)	34 0000 D at 200 000 V/m, 2 MHz [88]
MT electrophoretic mobility (bulk value)	$(-2.6 \pm 0.4) \times 10^{-8}$ m^2 /Vs [88]
MT electrophoretic mobility (MT oriented parallel to the E-field)	$(-2.59 \pm 0.02) \times 10^{-8}$ m^2 /Vs [79] $(-2.93 \pm 0.02) \times 10^{-8}$ m^2 /Vs [80]
MT electrophoretic mobility (MT oriented perpendicular to the E-field)	$(-2.15 \pm 0.01) \times 10^{-8}$ m^2 /Vs [79] $(-2.30 \pm 0.04) \times 10^{-8}$ m^2 /Vs [80]
MT Zeta potential	– 32.6 ± 0.3 mV [79] – 43.5 ± 6.5 mV [80]
MT effective linear charge density	– 280 *e*/μm [87] – 256 *e*/μm [94]

MT effective surface charge density	-0.229 ± 0.003 *e*/nm^2 [79] -0.24 ± 0.04 *e*/nm^2 [80]

Table 2.1. Electrical parameters of tubulin and MTs determined from the mechanical response to electrical stimuli. Ionic concentrations were calculated assuming total dissociation of Mg^{2+}, Na^+, K^+ and Cl^- ions. All measurements were taken between pH 6.8 and 7.0.

The addition of cations to the solution can regulate the material properties (including stiffness, morphology and stability) of tubulin polymers through non-specific interactions. For example, the presence of trivalent cations Al^{3+} and Fe^{3+} at high concentrations (> 250 μM), causes MT destabilization and tubulin aggregation.[99-100] The presence of Ba^{2+}, on the other hand, leads to an increase in MT stability and stiffness (*e.g.* increasing the persistence length from 2 mm in control conditions to 5 mm in the presence of 5 mM $BaCl_2$; Figure 2.3 d).[101] The presence of Mg^{2+} and Mn^{2+} also increase MT stability, while additionally leading to the formation of GDP-tubulin 'rings' in solution. [102] Ba^{2+}, Mg^{2+} and Mn^{2+} are modeled to interact non-specifically with the tubulin dimer, lowering the electrostatic repulsion between the C-termini tail and tubulin body. The shielding effect is modeled to bias the C-termini towards a kinked conformation, stabilizing the overall MT structure. [103] It is worth noting that not all divalent cations have this effect; the presence of Zn^{2+} or Co^{2+} leads to the formation of polymeric, two-dimensional tubulin sheets instead of cylindrical MTs.[104-106] Zn^{2+} interacts at the N-terminal of each tubulin monomer, causing protofilaments to align in an antiparallel orientation to one another (Figure 2.3 c).[107] Prolonged exposure to a solution of Zn^{2+} can lead to sheets 'wrapping up' to form >300 nm diameter macrotubes, indicating the importance of electrostatics in the determination of the polymorphic structure of tubulin.[105, 108] Interestingly, Ca^{2+} has the opposite effect, causing MT disassembly through acceleration of GTP hydrolysis.[109-110] Addition of monovalent cations Na^+ and K^+ stimulates MT assembly until a saturating concentration is reached, after which an inhibitory effect is observed.[111] The presence of Na^+ has also been observed to stabilize tubulin sheets for long durations of time.[108] In contrast, high concentrations of the organometallic cation CH_3Hg^+ cause MT disassembly through potential interactions with free sulfhydryl groups on the tubulin surface.[112-113] The presence of large (trivalent, tetravalent and pentavalent) cations derived from lysine oligomers induces the formation of hexagonal bundles of MTs and so-called 'living necklaces'. [114] Collectively, these

results indicate the potential utility of electrostatic parameters to enable the tuning of cargo volume, movement and direction within integrated nanodevices that utilize MT-kinesin systems for transport.

In addition to responding to the presence of different ions, C-termini tails are also modeled to undergo conformational changes when exposed to nanosecond electrical pulses (nsEPs; 20 kV/cm, >400 nanoseconds). Exposure to nsEPs has been experimentally shown to inhibit the ability of tubulin to form MTs (Figure 2.4 a).[67] Upon nsEP exposure, changes in zeta potential and hydrodynamic radii that are consistent with C-termini extension were clearly observed (Figure 2.4 b and c). nsEP exposure to U2OS cells in a low conductivity buffer background led to MT loss, as seen by the loss of filamentous structures upon performing confocal microscopy (Figure 2.4 d; center panel). This also resulted in fluorescently tagged End Binding protein 1 (EB1), which can be imaged as distinct 'comets' that localize to growing MT ends, [115-117] which have been seen to instead diffusely spread across the cytoplasm (Figure 2.4 d; far left panel).[68] Other work has also shown that nsEP exposure with similar parameters led to intracellular MT disruption.[118-119] Interestingly, a reversal of this MT destabilizing effect was seen in high conductivity media, where nsEP exposure led to a smaller number of MTs in cells overall, which underwent longer growth times. The nsEP-MT interaction is hence proposed as a potential target for non-pharmacological therapies (or in combination with pharmacological therapies) in the context of cancer and illustrates the utility of using electric fields to successfully induce biochemical changes within intracellular proteins. Importantly, already developed cancer treatment modalities involving electric fields such as tumor-treating fields (TTFields) are also hypothesized to interact mechano-chemically with the MT network of the cancer cell.[64-66] According to the standard model, TTFields, which are 10-300 kHz, 1-3 V_{rms}/cm a.c. electric fields, inhibit cancer-cell proliferation by interacting with the large dipole moment of tubulin, which causes MT alignment along TTField-generated electric field lines leading to a disruption of the mitotic spindles. It is important to note that the precise molecular mechanism through which TTFields – or any other electric fields for that matter – act on MT dynamic instability parameters has not yet been clearly established.

If *in Vitro* assays determining the relationship between electric field parameters (including frequency, intensity, waveform type) could be performed, then the sensitivity and specificity of electric field based anticancer modalities would be significantly improved providing an important piece of information needed to optimize the delivery of this therapeutic modality for cancer patients. Notably, upon translating the laboratory measurement results for MTs to those within living cells, an important difference involves the presence of cell membranes. It is well known that phospholipid bilayer structure of the membrane can be represented as a capacitor, which could be seen as a high-pass filter, which would allow sufficiently high frequency electric fields to permeate into the cytoplasm as is in evidence, when examining the action of TTFields.[122]

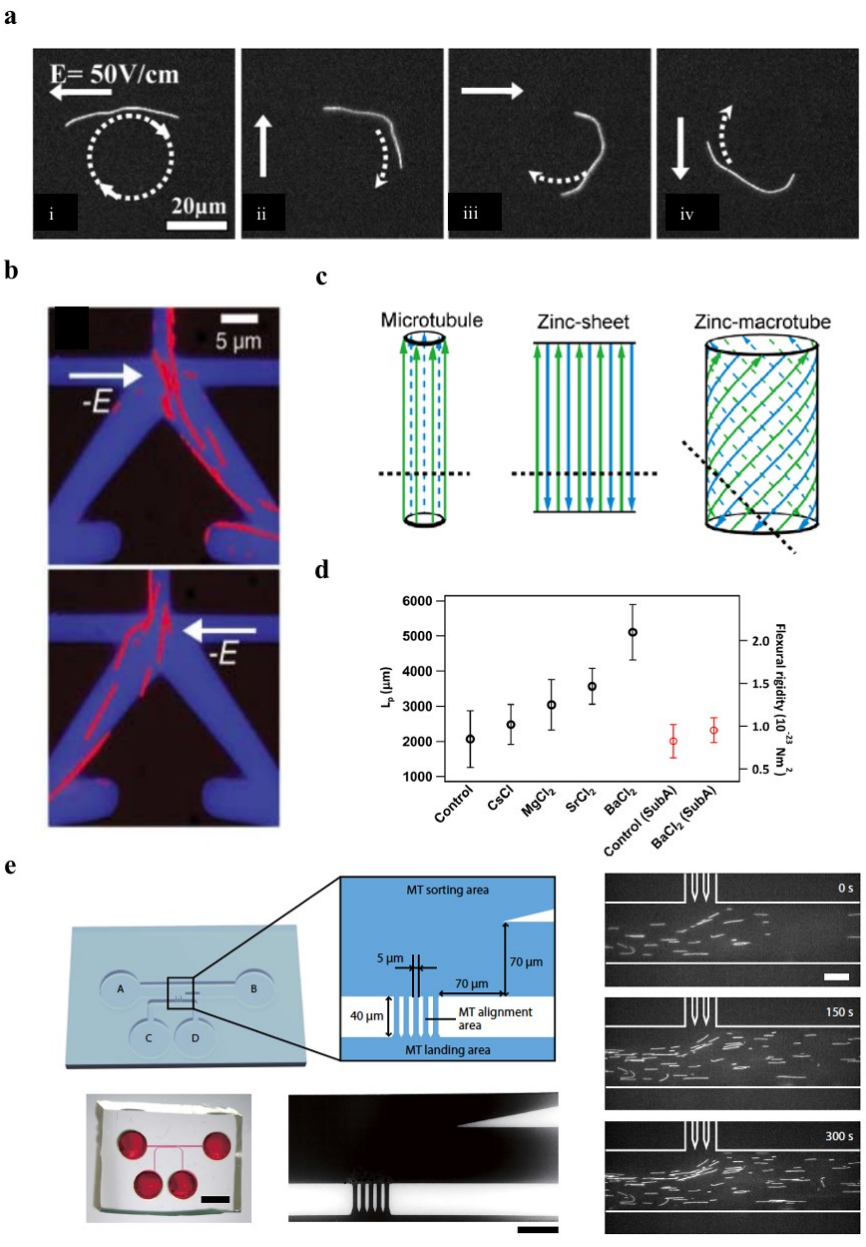

Figure 2.3. (a) Demonstration of circular translocation of a MT on a kinesin coated substrate using an electric field of 50 V/cm in directions specified by the solid arrow. Adapted with permission from ref 120. Copyright 2007 American Chemical Society. (b) MT steering on kinesin-coated microchannels with an electric field of 500 V/cm. Reproduced with permission from ref 80. Copyright 2006 American Association for the Advancement of Science. (c) Schematics of tubulin polymorphs, indicating MTs (left), sheets (centre) and macrotubes (right). Reproduced with permission from ref 121. Copyright 2012 PLOS One. (d) Graph displaying the variation of persistence length on the addition of various divalent salts. Reproduced with permission from ref 101. Copyright 2006 American Chemical Society. (e) A sorting device for kinesin steered MTs of varying stiffness. Varying curvature trajectories are achieved with a 30 V/cm field strength. Reproduced with permission from ref 62. Copyright 2017 American Association for the Advancement of Science.

Furthermore, cell membranes incorporate numerous membrane proteins (including those that make up ion channels). This results in the electrical representation of the membrane as a 'leaky capacitor' further allowing the electric fields to penetrate into the cell interior.[123] Dividing cells, in particular, can be characterized by the presence of the cleavage furrow during cytokinesis, which additionally provides areas of electric field penetration.[124] Therefore, the electric field effects of MTs in living cells become not only frequency dependent, but also dependent on MT location within the cell.

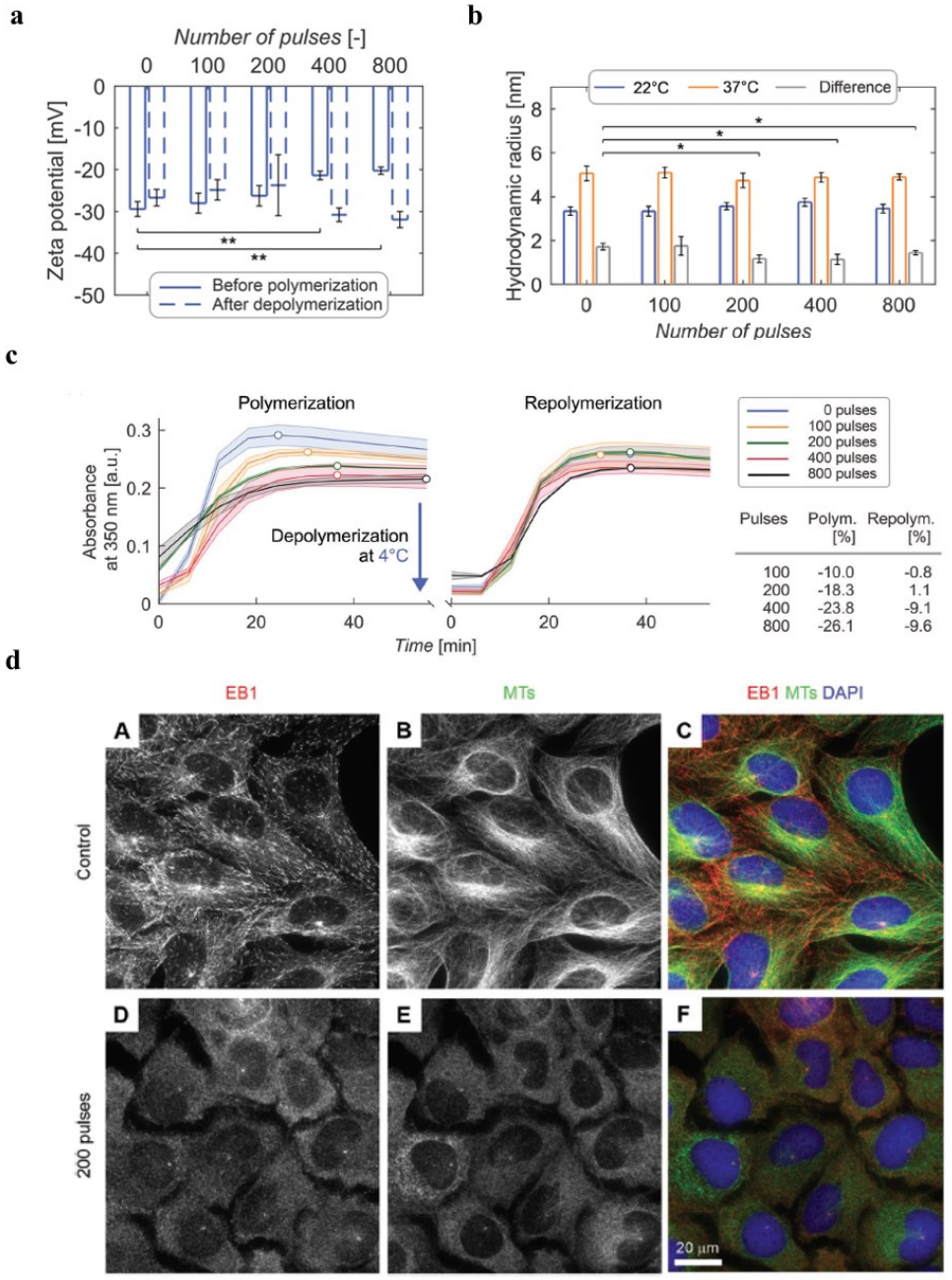

Figure 2.4. (a) Graphs displaying the changes in tubulin zeta potential values upon exposure to increasing number of nanosecond electropulses (nsEPs). Reproduced with permission from ref 67. Copyright 2019 Wiley-VCH. (b) Graphs displaying values of tubulin hydrodynamic radius upon incubation at different temperature values, and number of nsEPs. Reproduced with permission from ref 67. Copyright 2019 Wiley-VCH. (c) Turbidity experiments showing MT polymerization is inhibited in the presence of nsEPs (right). After MT depolymerization by cooling to 4 °C, exposure to nsEPs also resulted in inhibited repolymerization (left). Reproduced with permission from ref 67.

Copyright 2019 Wiley-VCH. (d) The effect of nsEP exposure on U2OS cells imaged using immunofluorescence staining (top). The effect on the MAP, EB1 (end-binding protein 1; red), MTs (green) and nuclei (blue) can be clearly seen. Reproduced with permission from ref 68. Copyright 2020 Wiley-VCH.

MICROTUBULES AS INTRACELLULAR NANOWIRES

Due to their large negative charge, MTs cause extensive cationic condensation on their outer surface. The 4 nm long, brush-like C-termini tails, that protrude from the outer MT surface, increase the surface area available for cationic condensation. While counterions closer to the MT surface are modeled to be 'frozen', those further away from the surface can move along the MT relatively freely, creating an axial conductive sheath along the MT.[14] Some resistance to this ionic current is caused by thermal noise and interactions with the protein surface, with axial and perpendicular resistances for a single 8 nm section of a MT having been estimated to be 10^9 Ω and 7×10^6 Ω, respectively.[125] A capacitance is predicted to be established by the presence of a theorized 'depleted layer' with a thickness corresponding to the Bjerrum length (room temperature Bjerrum length in aqueous buffer = 6.7 Å[125]), which separates the condensed counterions from the bulk solution.[125,17] The existence of this depleted layer still needs to be experimentally confirmed. However, if this model is correct then the MT capacitance will be non-linear due to C-termini dynamics and saturable size.[17] The capacitance of 8 nm section of a MT, excluding the C-termini, is predicted to be 0.68 fF and the net capacitance due to all corresponding C-termini is estimated as 0.64 fF.[17] The helical arrangement of tubulin dimers in a MT is theorized to cause the axial currents to twist forming a solenoidal path with a corresponding inductance of 0.8 fH per ring. These values of resistance, capacitance and inductance, as well as the resistance to ionic flows through the nanopores (see *Ionic currents across the MT wall*), can be used in an equivalent circuit model to predict the behavior of ionic transmission along, around and inside a MT. Consequently, the complex geometry of a MT results in highly unusual ionic electric conduction behavior, which, when experimentally validated, can serve as a basis for the construction of complex non-trivial bioelectronic devices.

Unsurprisingly, MTs have been theorized to behave as transmission lines, with signals propagating across their lengths as nonlinear ionic waves.[17, 95, 125] These waves can be described by their associated potential, which was shown to have an anti-kink wave-front along the MT

length.[125] For reasonable circuit parameter values, monovalent and divalent counterionic waves were shown to propagate as solitons, which retain their localized waveform despite experiencing ohmic losses due to the presence of nonlinear effects. These soliton pulses have propagation speeds estimated to be in the mm/s to cm/s range.[16-17] The sheer magnitude of ionic wave velocity may help explain how sub-cellular electrical signals can propagate amidst large amounts of thermal noise in an aqueous environment. The influence of MTs on local charge carrier dynamics, through the complex interconnected network formed within cells, particularly neurons, highlights their potentially important role in bioelectric signal transmission.

Ionic currents along the MT outer surface

Early hints that MTs altered ionic transport came in 1985, when Vassilev and co-workers showed that the presence of MTs led to electrical coupling between two lipid bilayer membranes (LBMs) that were separated by a 100 μm gap.[74] As the interesting electrical properties of the C-termini and counterionic condensation around MTs were revealed, several experimental efforts to evaluate counterionic conductivity around MTs were performed. However, the determination of the ionic conductance around a single MT is a major experimental challenge, mainly because the equivalent circuit formed by thousands of cylindrical MTs of different lengths (each with its own resistive, capacitive and inductive components) oriented in random directions in a background solution is difficult to reliably reconstruct. Reliable experimental determination of MT conductivity is further hampered by the high conductivity and experimental noise associated with high ionic strength buffers (such as BRB80) that MTs are most stable in. Despite such obstacles, several noteworthy attempts at determining the MT conductivity have been made and are discussed below.

To quantify the d.c. conductivity of an individual MT from an ensemble, the electrostatic interaction between positively charged Poly-L-lysine (PLL) and MTs was exploited.[126] After fabricating metallic contact pads with a 10 μm gap, PLL was layered and MAP-rich MTs settled such that they straddled both contacts (Figure 2.6 a; top). After repeated I-V (current-voltage) measurements (Figure 2.6 a; below), the authors extrapolated the d.c. conductivity of a single MT to be of the order of 90 S/m. While the approach using PLL to coat a surface with MTs reduced the contribution from background buffer solution, the calculation of MT d.c. conductivity was based on the assumption that the PLL-MTs had adsorbed all ionic species

present within the solution, and that MT resistance was connected to that of the solution in parallel. Additionally, it was unclear if the MTs denatured after several minutes of repeated voltage exposure, or if the presence of MAPs in solution altered conductivity.

To study the d.c. conductivity of a single MT, a dual patch clamp technique was used to directly contact the ends of a MT (Figure 2.6 b; top). This approach avoided extrapolating ensemble MT measurements as being connected in series or parallel, thus providing for a more accurate presentation of MT d.c. conductivity. Interestingly, these experiments revealed an increase in the collected current signal as opposed to background solution (BRB80; Figure 2.6 b; below).[15] Based on differences between stimulating and collected currents at the patch pipettes, it was concluded that MTs acted as ionic current amplifiers, and suggested their potential roles as intracellular transistors that could regulate synaptic plasticity through electrical information transmission (ionic currents).

Measurements of MT angular velocity in an a.c electric field were used to determine that MT counterionic conductivity was 150 mS/m in the 1 kHz – 10 MHz range (Figure 2.7 a; below). These experiments used MTs stabilized in taxol, within a highly diluted ('low salt') buffer (1 mM MES; Figure 2.7 a; top).[127] When C-termini were enzymatically cleaved by the addition of subtilisin, the measured conductivity was reduced to 60% of the reference value indicating the importance of C-termini in MT-based charge transport. Adding different salts to the background solution showed that ionic conductance was highest in the presence of monovalent K^+ and Na^+ and reduced successively in the presence of divalent and trivalent ions. In relatively higher ionic strengths (BRB16), dielectrophoresis experiments showed that at 2.5 MHz, MT conductivity was 250 mS/m.[128]

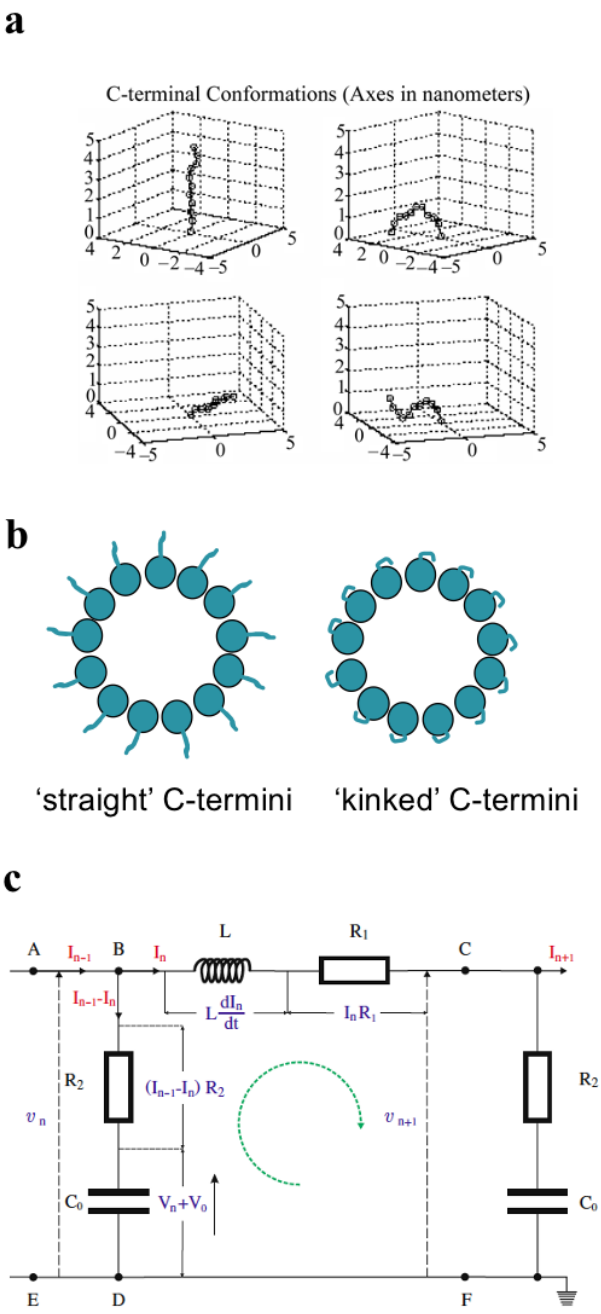

Figure 2.5. (a) Results from a simulation depicting various conformations adopted by a single C-terminus. Reproduced with permission from ref 78. Copyright 2005 Springer Nature. (b) Schematic of C-termini in the 'straight' and 'kinked' conformations, viewed from the MT cross section. (c) An equivalent circuit of ionic flow along the nth 8 nm section in a MT using a nonlinear transmission line model. Reproduced with permission from ref 125. Copyright 2009 Springer Nature.

Electrochemical impedance spectroscopy using non-uniform a.c. electric fields (Figure 2.7 b; top) and low ionic strength buffers (ionic concentrations ~16 mM) indicated that MTs increase

solution conductance, while unpolymerized tubulin dimers decrease solution conductance at identical concentrations (Figure 2.7 b; below).[81] Interestingly, the frequency range (100-300 kHz) in which this behavior was observed matched that of TTFields (tumor-treating electric fields). While such observational correlation may indicate potential involvement of MT-based ionic transport in TTField-based tumor growth inhibition, it should be noted that these experiments were performed *in Vitro* (using low ionic strength buffer solutions as background). As a consequence, these results may have limited applicability to *in Vivo* systems due to the screening effects of phospholipid bilayers forming membranes. However, the screening effects are imperfect for several reasons: (a) the 'leaky' capacitor membrane structures do allow for some electric field penetration through ion channels, membrane proteins and pores, (b) in dividing cells, especially during cytokinesis, the high curvature of the membrane allows a greater degree of electric field penetration than a rounded shape in interphase and (c) there are frequency-dependent effects of electric field attenuation across the membrane with intermediate frequency values in the TTField range exhibiting lower attenuation than either higher or lower frequencies.[129]

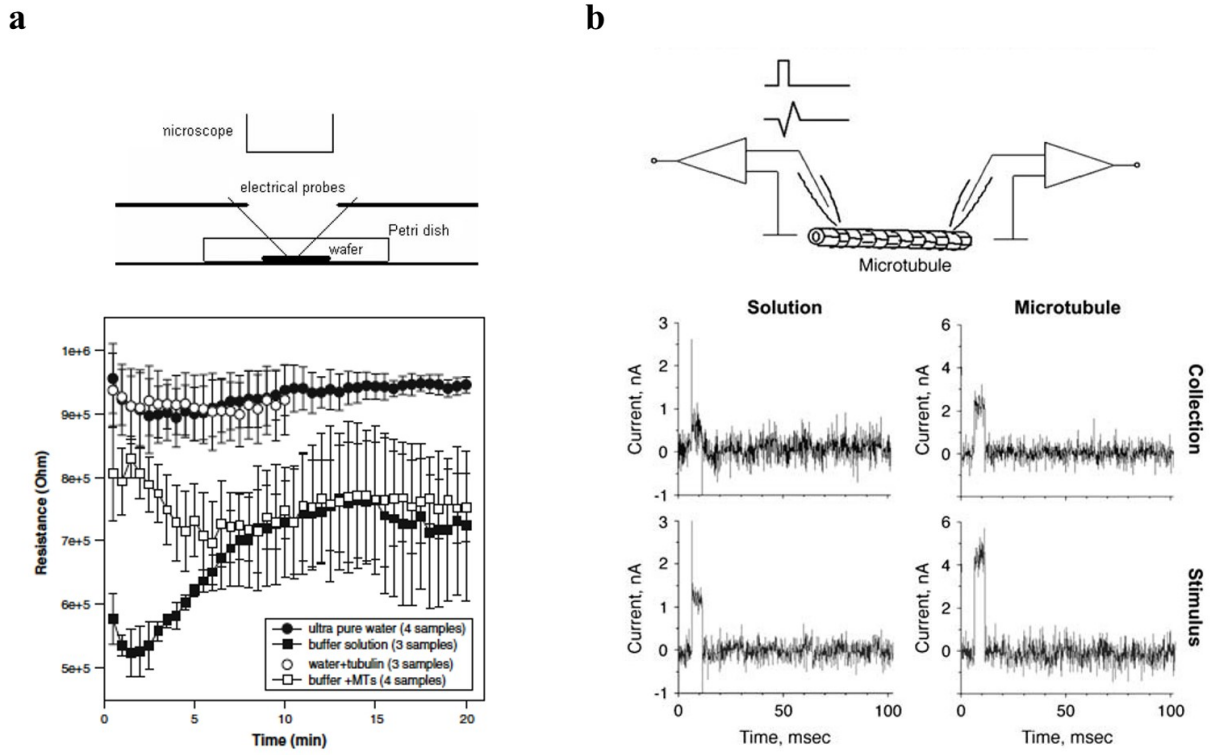

Figure 2.6. (a) Schematic representation of a probe-type geometry used to evaluate the d.c. response of MTs to voltage exposure (top) The variation of resistance of various samples as a function of time, measured at the probe tips (below). Reproduced

with permission from ref 126. Copyright 2007 Springer Nature. (b) Experimental setup displaying patch-clamp based MT contact method (top). Variation of 'stimulus' and 'collection' currents as a function of time, indicating the potential of MTs as amplification devices within the cell. (below). Reproduced with permission from ref 15. Copyright 2006 Biophysical Society.

To reduce experimental noise due to the high conductance of the background buffers, which masks MT conductance, the a.c. experiments discussed above were performed with low ionic strength solutions (between 2-32 mM ionic concentration). Additionally, low tubulin concentrations were used, aiming to reduce MT number in solution and thus reduce noise and simplify the modeling of an equivalent electrical circuit. However, intracellular ionic strengths are appreciably higher (200-500 mM),[130-131] and MT networks can exist in densely packed, highly interconnected configurations within the cell. Thus, to partially mimic intracellular conditions, utilizing BRB80 (ionic strength 160 mM) and physiologically relevant tubulin concentrations, impedance spectroscopy experiments using a parallel-plate contact configuration (Figure 2.8c; top) were performed. It was observed that the presence of MTs caused a dramatic increase in solution capacitance, while the presence of tubulin did not alter it significantly (Figure 2.8 c; below).[13] Notably, when the resistance of MT-containing solution was compared to that of high ionic strength background, a 'flip' in conductance was seen in the 20-60 Hz range, indicating that MTs increased solution conductance within this frequency range compared to free tubulin. While MTs clearly introduce significant changes in conductivity and capacitance of the solution in which they are contained, it is less clear how to model the entire interconnected MT meshwork. Equivalent circuit models accounting for the electrical behavior of MTs must incorporate subtle, nonlinear aspects[88] in addition to random alignments and connections formed by MTs. Such computational modeling is important for designing and characterizing MT networks with well-controlled I-V characteristics in the a.c. domain.

Ionic currents across the MT wall

In addition to being transported along the MT outer surface, ions have been modeled to permeate across the MT wall, through gaps, or 'nanopores' created between adjacent tubulin dimers (Figure 2.8 a). There are four pore types. Type 1 and type 2 pores, which are the most common, are the intra- and interdimer gaps, with radii of 4 Å and 3 Å respectively, in their most constricted area. Type 3 and type 4 pores are found exclusively at the MT 'seam', forming

as a consequence of the gap between two protofilaments. Present literature indicates that MTs act as 'leaky' pipes, with ions permeating into the lumen, and being released at MT ends.

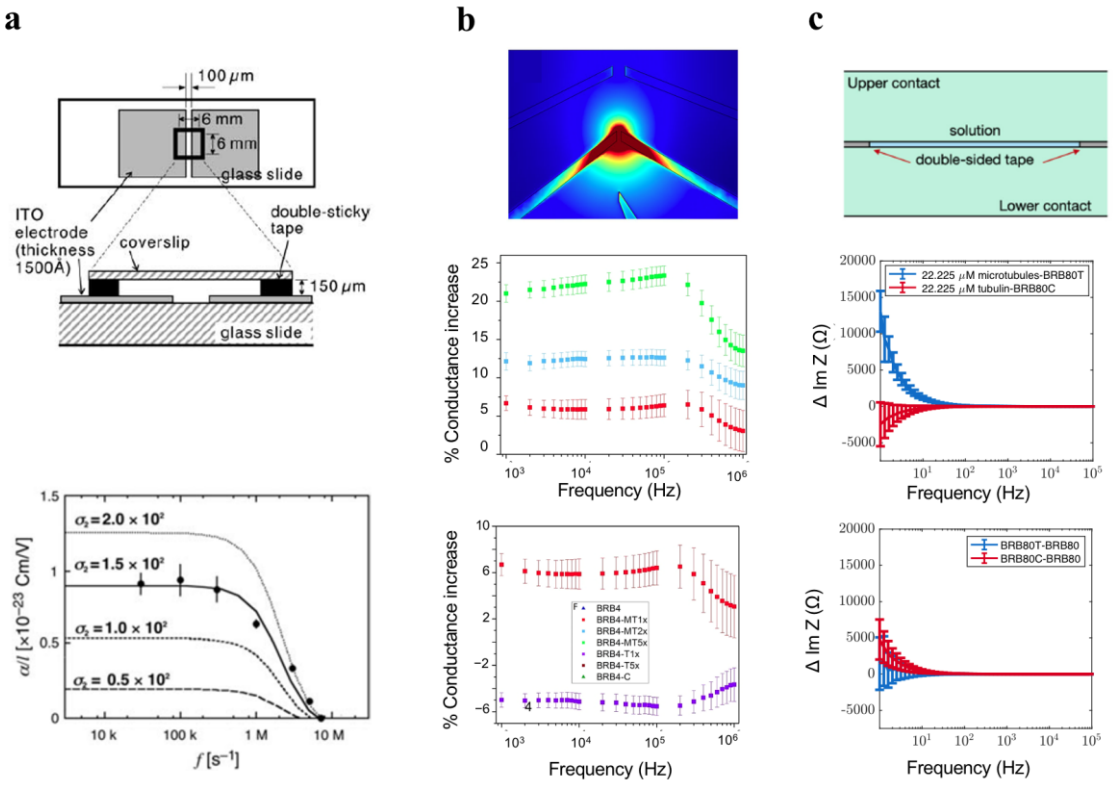

Figure 2.7. (a) Experimental setup used to determine MT conductivity through electro-rotation experiments (top). The variation of polarization coefficient (α) per unit length, as a function of input electric field frequency. The best fit for line for conductance was displayed to be 1.5 × 102 mS/m (below). Reproduced with permission from ref 127. Copyright 2006 Biophysical Society. (b) Spatial variation of electric field intensity of a probe-type contact geometry used to determine the effect of MTs and tubulin on solution conductance (top). The variation of MT and tubulin conductance as a function of frequency (below). Adapted with permission from ref 81. Copyright 2017 Springer Nature. (c) Schematic representation of a parallel-plate contact geometry used to determine the effect of MTs (at cell-like concentrations of tubulin and ions) on solution capacitance (top). Differences between imaginary components of tubulin and MTs, with their respective background solutions (below). Adapted with permission from ref 13. Copyright 2020 Multidisciplinary Digital Publishing Institute.

Cations have been modeled to permeate across the pores using energy supplied by thermally driven C-termini conformational changes. Brownian dynamics simulations of ionic conductance found that pores acted as ionic valves, with the conductance being higher when ions were moving from outside to inside the MT (Figure 2.8 b).[77] When tubulin charge was removed, cationic conductance was calculated to be lowered by a factor of 15. Ionic permeation has also been modeled to arise due to the difference in electrostatic charge density between the internal and external MT surfaces.[132] These MD (molecular dynamics)-based simulations also found that type 1 pores were more conductive than type 2 pores (Figure 2.8 c, d). Although K^+ and Na^+ ions permeated across the MT wall, Ca^{2+} and Mg^{2+} ions were unable to do so, due to their higher electrostatic attraction to the electrostatically negative external surface and their larger hydration shells (Figure 2.8 e). Interestingly, it was seen that the concentration of K^+ inside the lumen increased in response to a pulse of Ca^{2+} ions travelling along the outer MT surface (Figure 2.8 f). Thus, the transfer of cations across the MT wall clearly plays a key role in the polymer's overall electrical properties. Importantly, this work did not include C-termini tails (not resolved crystallographically due to their flexibility), because they do not contribute to the overall MT structure or nanopore dimensions. However, due to the C-termini containing a large fraction of the overall MT charge, and previous simulations showing its importance in charge transport across the MT wall, the exclusion of the C-termini is a serious drawback, and could be incorporated in a future work.

Experimental validation of ionic transport across the MT wall finally came in 2016, when patch-clamping experiments on tubulin sheets showed cationic permeation across these sheets representing a MT wall (Figure 10 b).[133] The ionic current was found to be oscillatory with a fundamental frequency of ~ 29 Hz that did not change, irrespective of the holding potential used (Figure 10 c and d). The average change in conductance over an oscillation at physiological conditions (140 mM K^+) was measured to be 640%. The presence of taxol (which binds to tubulin at an intermediate binding site within the nanopores and in the main binding site to the lumen surface of a MT) decreased the time-averaged conductivity and strongly inhibited ionic oscillations. A similar oscillatory response was observed in MT bundles, which demonstrated a slightly different fundamental frequency (typically 39 Hz, which could result from differences in nanopore dimensions), a more complicated amplitude response and a smaller mean oscillatory swing corresponding to a 258% conductance change (Figure 10 d).[21] For both MT sheets and bundles, the mean current-to-voltage response was linear over short time periods but displayed rectification over longer times. These measurements led to the

hypothesis that a nanopore behaves as an electrical oscillator and the total electrical response of a MT is a result of synchronization between the oscillations. Recent measurements have shown that single MTs also display an oscillatory response to constant holding potentials, although the frequency response is much more complex (5 different fundamental frequencies, all between 1 and 100 Hz, were observed) and the changes in conductance are greater than those found for previously measured tubulin structure.[134] Impedance spectroscopy experiments performed on MT-containing solutions validated these findings, displaying an increase in solution conductance in the 20-60 Hz range, potentially due to ionic oscillations across the MT wall at these frequencies (Figure 10 a).[135] Although experimental evidence for nanopore electrical oscillations is strong, a theoretical explanation as to the mechanism behind this has not been provided and should be a focus of future work.

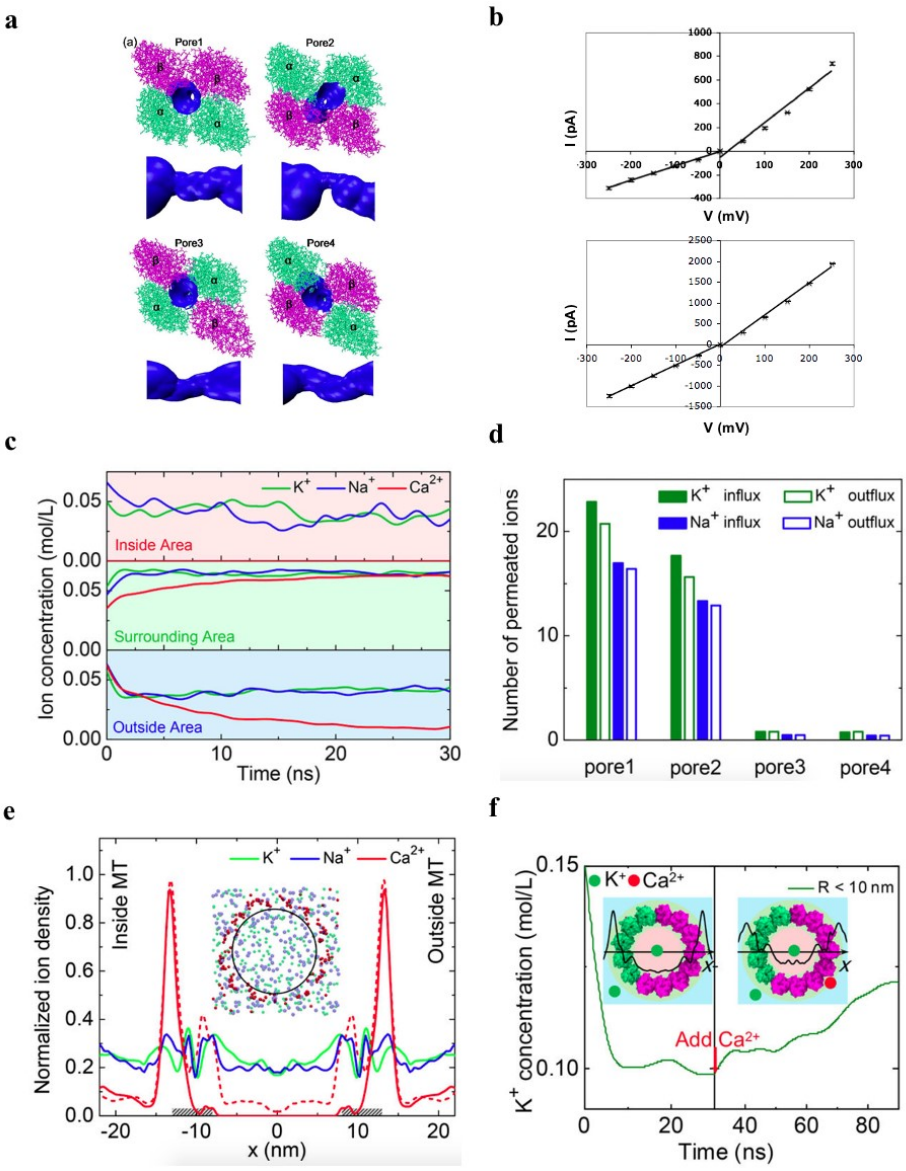

Figure 2.8. (a) Snapshots of nanopores created between tubulin dimers within the MT lattice. Reproduced with permission from ref 132. Copyright 2018 American Chemical Society. (b) Representation of simulated current as a function of voltage across type 1 (top) and type 2 (below) pores in the wall. Reproduced with permission from ref 77. Copyright 2010 American Physical Society. (c) Variation of ionic concentration of ions as a function of time, inside the MT lumen (red), outside the MT outer surface (green), and in bulks solution (blue). Reproduced with permission from ref 132. Copyright 2018 American Chemical Society. (d) Graph displaying the higher number of ions permeating across pore 1 and 2, as opposed to pore 3 and 4. Reproduced with permission from ref 132. Copyright 2018 American Chemical Society. (e) Distribution of K^+ ions around the MT wall. Reproduced with permission from ref 132. Copyright

2018 American Chemical Society. (f) A display of the influx ofK^+ ions as a function of time. Reproduced with permission from ref Reproduced with permission from ref 132. Copyright 2018 American Chemical Society.

It is worth noting that the two frequency regimes of increased MT conductance correspond to two separate ionic modes: The first frequency regime is between 100-300 kHz, where the increased conductance is hypothesized to occur as a consequence of ionic movement along the MT length, along its outer surface. The second frequency regime is between 20-60 Hz, where the increased conductance is thought to be a consequence of ionic movement across the nanopores in the MT wall, possibly induced by C-termini oscillations. An experimental exploration of the third hypothesized ionic mode, that along the MT lumen, has not yet been performed and would offer an interesting insight due to the shielding effects of the MT walls. The relative proportion of ions transported along each mode (along the MT outer surface through C-termini, along the MT lumen, and across nanopores) is also unclear and should also be a focus of future work (Figure 2.10). The utilization of TBAs to block/enhance a particular mode should be useful in this endeavor. For example, utilization of the protease subtilisin, which cleaves C-termini,[136] will nullify the C-termini's significant contribution to ionic transport along the MT outer surface. To determine the proportion of ion flow through the MT lumen, 2D tubulin sheets, which do not have a lumen, and hollow, >200 nm wide 'macrotubes' can be separately subjected to patch clamping and impedance spectroscopy, allowing for greater transport through the inner MT circumference. It is unclear how ionic transport will scale with dimensions of these polymorphic structures, given the presence of 'leaks' through nanopores and the different geometries. Nevertheless, experiments performed on sheets and macrotubes should shed light on the contribution of the MT lumen to ionic transport. Future experimental research must utilize MT-TBA interactions to decipher the relative importance of each mode. Notably, much of our present knowledge of MT electrical behavior is based on experiments performed in the presence of taxol (which inhibits ionic transport through nanopores[20-21, 133]). By comparing the impedance parameters of taxol-stabilized MTs to those that are stabilized by a TBA that does not block nanopores (such as the MAP TPX2[137]), it should be possible to glean information on the contribution of nanopores to MT-based ionic transport. Understanding how TBAs, actin filaments and cell organelles alter the ionic impedance around MTs will also enable us to understand their role in intracellular MT-based electrical signaling. This would enable a construction of an effective bioelectric circuit of a living cell.

Early work in this direction already indicates that the electrical behavior of MT nanopores changes in the presence of actin filaments,[19] previously only known to interact with MTs biochemically through MAPs such as MAP2 and MAP tau.[138-139] In patch-clamp measurements, the presence of actin filaments led to a significant increase in the mean current across MT sheets while keeping their oscillatory frequency unchanged (Figure 2.9 e). A similar response was observed for MT bundles where the charge transfer increased by about 100% after the addition of actin filaments. Electrostatic 'crosstalk' between actin filaments and MTs may have biological implications, such as the generation of propagating ionic soliton waves around and along actin filaments in the neighborhood of MT walls that generate such ionic oscillations, which could be of significance in excitable cells such as neurons and muscle cells where actin filaments are involved in neurotransmitter release and in force generation, respectively.[95, 140] Understanding how each impedance component varies with MT length is critical for the fabrication of future MT-based electrical devices. Due to the presence of three separate modes of ionic transport in a single MT, addressing such issues is nontrivial. The significance of 'leakage current' along the MT length is also unclear and should be included in future models. Understanding the variation of ionic conductivity with MT diameter should give insights into the importance of leakage current, being critical both from a device perspective as well as an evolutionary standpoint. More sophisticated computational models and future experiments should, therefore, consider all three modes of ionic transport, changing MT dimensions, and include interactions with actin filaments, tubulin-binding drugs and MAPs.

Due to their exotic electrical properties, MTs have been modeled as 'memristors' (two-terminal devices that are described by a resistance which is dependent on the previous conductive state of the device, *i.e.* resistance with memory).[141] Changes in the C-termini conformation have been theorized to affect changes in MT resistance to counter-ionic currents, since the C-termini conformation is influenced by the counter-ionic concentration.[135, 142] This results in the emergence of memristance, which has been calculated to be between 1 Ω and 20 kΩ for a 10 μm MT. Although direct experimental proof of these results is still required, it was found that when subjected to the same magnitude of d.c. voltage, a solution containing MTs responded with different resistance values depending on the direction of the voltage, which is consistent with this assumption.[143] It was also seen that when patch-clamp based square-voltage pulses were applied to 'silent' tubulin sheets (those that did not display oscillatory responses under voltage-clamp conditions), the response could be modeled by a circuit with a saturating

capacitor and a memristor. While more work (experimental and theoretical) is required to verify such extraordinary and far-reaching claims, memristive properties of MTs suggest many intriguing possibilities. It has been shown that memristors can implement logical operations. [144] and they have great promise for use in neuromorphic computing. [145] Tuszynski *et al.* tie these findings back to basic biology and suggest that MT memristive properties may be behind the 'memory' demonstrated by amoeba. [135] Thus, memristive properties of MTs would have extensive implications for bio-computing applications and basic biological research. Moreover, due to the prominent role played by MTs in the neuronal cytoskeleton, where they form parallel bundles interconnected by MAPs, their potential involvement in memristive signal processing may be of major importance to our understanding of how the human brain works. The sheer complexity of the electrical properties of MTs and their sensitivity to the ambient conditions may offer a rich spectrum of possibilities for signal processing in both living systems and their hybrid technological adaptations.

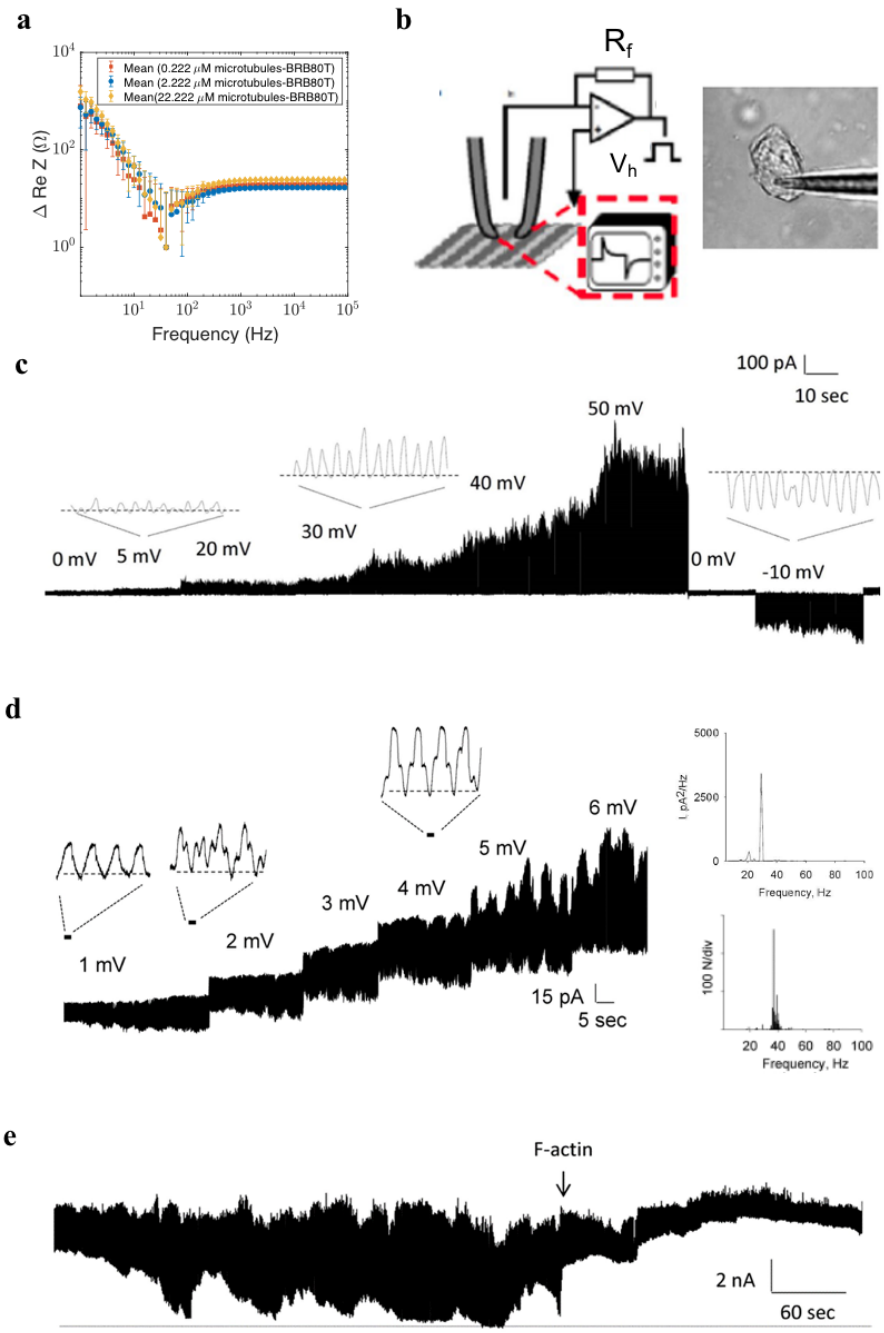

Figure 2.9. (a) Impedance spectroscopy measurements displaying an increase in solution conductance in the 20-60 Hz range upon the addition of MTs. Adapted with permission from ref 127. Copyright 2020 Multidisciplinary Digital Publishing Institute. (b) Patch-clamp based experimental setup to determine the current response of MTs and sheets. Reproduced with permission from ref 20. Copyright 2019 Springer Nature. (c) The oscillatory current response of a MT sheet voltage-clamped at different potentials. Reproduced with permission from ref 133. Copyright 2016 Springer Nature. (d) The oscillatory response of a voltage-clamped MT bundle as a function of time. Reproduced with permission from ref 21. Copyright 2018 Springer Nature. Insets

display Fourier transforms of a typical voltage-clamped MT sheet response (upper inset) and of a typical voltage-clamped MT bundles response (lower inset). The fundamental oscillation frequencies of ~30 Hz for MT sheets and ~40 Hz for MT bundles are clearly shown. Reproduced with permission from ref 133. Copyright 2018 Springer Nature. (e) The change in the MT sheet voltage-clamped response upon addition of f-actin to the solution. Reproduced with permission from ref 19. Copyright 2020 Wiley-VCH.

PERSPECTIVES

In addition to communicating through biochemical pathways, intracellular macromolecules communicate through bioelectrical cues. Both theoretical/computational modeling and experimental work illustrate the significance of MTs in such communication. MTs can respond to bioelectrical signals through mechanical migration,[45, 79-80, 88] electro-rotation,[91, 127] changes in C-termini conformation,[17, 125] mechanical stiffness[101] and surface charge,[87] ionic transport along the outer surface[15] and across the nanopores.[20-21, 133] These electrical, biochemical and mechanical responses are, of course, interrelated, with the precise boundaries of each response regime being largely unclear. While significant advances in our understanding of MT response to electrical stimuli have been achieved in the past half-decade, further work must be performed to determine the exact nature (electric field intensity, frequency, waveform) of the electrical stimuli that elicit each response. Future work should focus not only on how electric fields alter the interactions of MTs with TBAs such as kinesins, but also how MT-TBA interactions alter MT electrical properties. Careful research on the interplay between external electrical field application, TBA binding and resultant MT properties is needed to fully realize the potential of MTs as tunable electrical conduits and ionic transporters.

Characterization techniques will need to be advanced to obtain quantitative information about MT electrical properties. The concentration of various cations in the immediate vicinity of MTs is useful to know in this connection. Currently, there are no reports on the empirical measurement of local ionic concentrations for tubulin dimers and MTs. As previously mentioned, our understanding of the different modes of conductance in a MT is largely incomplete and, in particular, the nanopores in MTs have received little attention (Figure 2.10). The binding of fluoroionophores to select amino acids in MTs might offer a way forward to estimate the local concentrations of specific cations through fluorescence, and changes in the local concentration near nanopores to obtain insight into the ionic conductance of the

nanopores. For instance, potassium fluoroionophores based on dye-conjugated crown ethers and cryptands are able to selectively detect K^+ ions (even in a Na^+ rich electrolyte)[146] and 4-pyridylethenylbenzene derivatives can detect local proton concentrations through shifts in their emission spectra.[147] Patch clamp techniques are routinely used to study the electrical properties of protein nanopores.[148] Advanced scanning probe microscopy (SPM) techniques tailored to nanopores such as scanning ion conductance microscopy constitute a powerful suite of high spatial resolution characterization techniques to probe the conductance signatures of type 1 and type 2 nanopores in MTs.[149] One challenge associated with nanopore SPM is the interpretation of the conductance signatures obtained.[150] The ability to make direct electrical contact to the end of MTs through lithographically defined electrodes would enable gating the nanopores in MTs modulate the ionic conductance akin to a transistor.[151] Even the ion-sensitive field-effect transistor (ISFET) configuration commonly used in biosensing offers opportunities to advance the characterization of MTs. If the gate dielectric of an ISFET was constituted of a single layer carpet of MTs or zinc sheets, the saturation voltage and charging gate current during gate voltage sweeps could yield information regarding the total charge and conductance of nanopores in MT ensembles respectively. Although electric fields have been reported to align MTs, we are not aware of a mat of fully aligned MTs. Such a carpet of aligned MTs straddling two metal electrodes would enable magnetoresistive probing of the nanopore conductance in the alignment direction (orthogonal to the axes of the MTs) through the Hall effect by placing a third electrode at the side of the aligned carpet.

From a fundamental science standpoint, a better understanding of the role played by the lumen and C-termini for MT-based charge transport is crucial to both the fabrication of MT-based nanodevices and the determination of the electric properties of living cells. While deep inroads into our understanding of MT bioelectricity have been achieved by investigating their mechanical response to electrical stimuli, future utilization within nanodevices and medical modalities will require an improved understanding of their electrical response.

We now know that the electrical behavior (conductivity, surface charge) of free unpolymerized tubulin in solution is dramatically different from that in its polymerized forms.[81, 135] However, understanding how the electrical properties of free tubulin change as it polymerizes will help reveal how MT length and sheet dimensions control their electrical behavior. Future work showing precisely how actin filaments and TBAs alter MT electrical properties should shed further light on the promise of the cytoskeleton as a tunable, dynamic and sensitive

electromagnetic signal transduction device.[152] Indeed, the effect of MT electromechanical properties at the cellular system-level must be explored. Two-dimensional models have already displayed an enhancement of the piezo- and flexoelectric properties of the cell upon cytoskeletal degradation.[153] Expanding on such work will require a greater understanding of how to couple MT electro-mechanical properties to energy sources including acoustic waves. Recent work has also shown the importance of tunneling nanotubes (TNTs), which are membranous bridges formed between neighboring cells, for the transport of intracellular organelles and cytoplasmic molecules. [154-155] Interestingly, TNTs, which can contain MTs, [156-157] also transmit electrical signals through calcium waves between cells. [158-159] Given that MTs are modelled to play important roles in the storage and transport of intracellular ions, the relationship between ionic transport by MTs and that by TNTs must be explored. It would also be critical, from a medical perspective, to investigate if the characteristics of ionic transport are altered in diseased tissue, particularly brain tumors which have been shown to contain thicker longer intercellular bridges termed tumor microtubes (TMs).[160] Further, the effect of electric fields, particularly TTFields, on TNT-related MT transport would be interesting to study.

Outside the cell, if devices using tubulin and its polymers are to be fabricated, the electrical and mechanical properties of these biological polymers in solvents such as DMSO and DMF, which are commonly used for the fabrication of OLEDs and OPVs (organic photovoltaics), must be precisely determined.[161] Experiments performed in a variety of solution conditions (over a variety of solvents, pH values and ionic strengths) may reveal the origin of differences in reported values of conductivity and effective charge. As discussed in previous sections, theoretical models have postulated that MTs behave as transmission lines capable of propagating nonlinear ionic waves[16-17, 125] and that MTs have memristive properties.[135] Initial experiments have supported these hypotheses and shown that MTs can amplify propagating ionic signals.[20, 78] These results suggest that MTs could be a building block of bio-electronic circuits and bio-computational systems. To verify and develop this possibility, further experimental quantification of MT electrical properties is required. In addition to creating hybrid bio-nanoelectronic devices, implantable sub-cellular structures based on MTs can be engineered for applications such as neuro-regeneration, memory augmentation or targeted drug delivery.[162-164] If the challenges outlined above can be overcome, then the potential of MTs to reduce the complexity of microelectromechanical systems, while simultaneously enhancing their versatility and functionality, is monumental and can create avenues for a wide spectrum of applications.

We close this work with a list of 10 questions (Table 2.2) that must be answered in the field of MT bioelectricity in order to rapidly advance in the quest outlined above. Successfully addressing these questions will improve our understanding of MTs within the cell, while also enabling their utilization within medical and possibly bioelectronic devices.

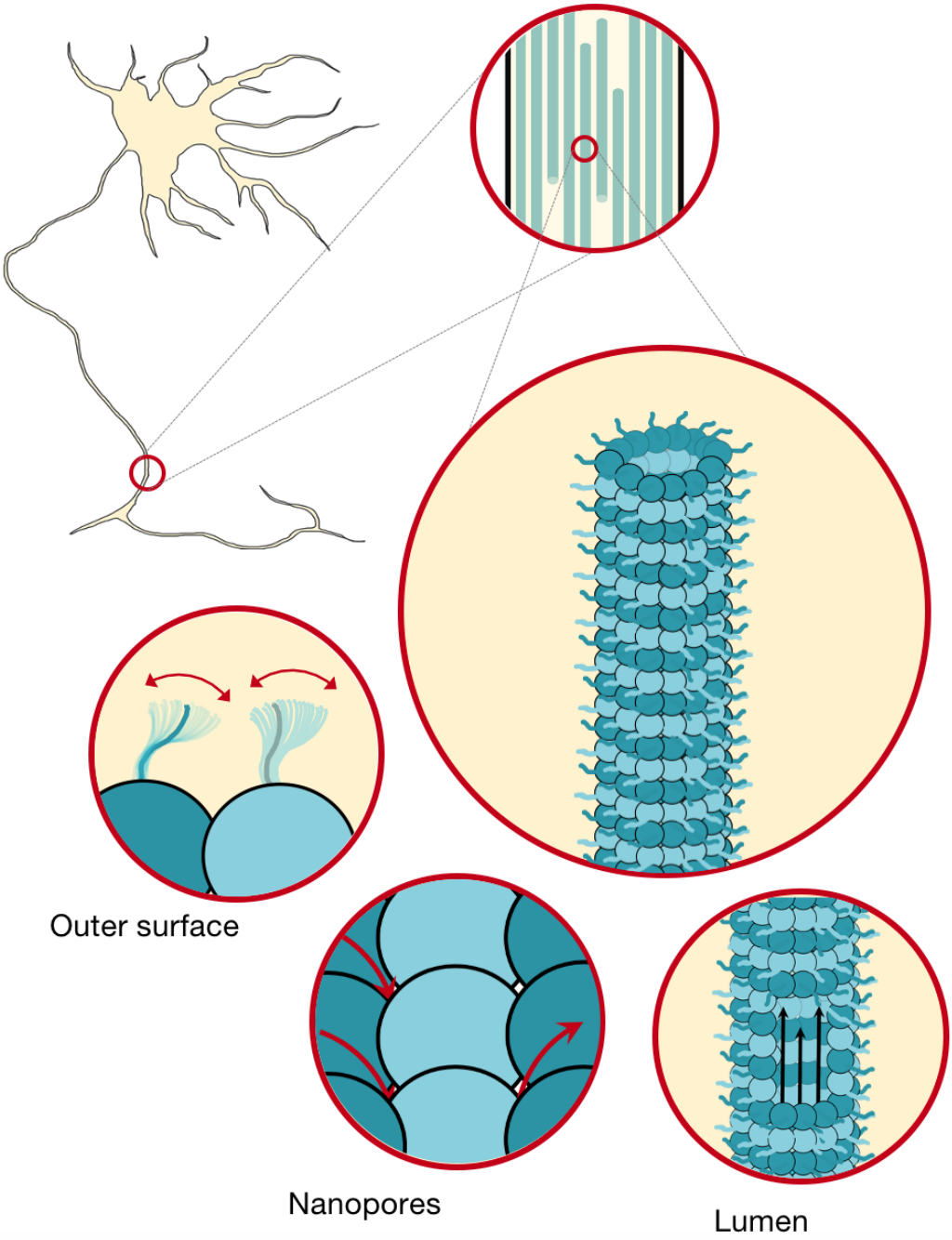

Figure 2.10. Demonstration of the various modes of ionic transport through MTs. Ionic transport can take place on the MT outer surface, across nanopores and inside the

lumen. Ionic signaling across MTs is modelled to play an important role in intraneuronal information processing.

Field of impact	Duration	Question
Intracellular biophysics	Short term	**How do electric fields interact with dynamic instability?** How to electric fields alter MT nucleation, elongation rate, shortening rate, catastrophe frequency and rescue frequency?
Intracellular biophysics	Short term	**Do MTs preferentially transport ions?** Which ions are transported preferentially?
Intracellular biophysics	Medium term	**How do MAP and drug binding, and the presence of actin filaments, alter MT conductivity?**
Intracellular biophysics	Long term	**Does MT/tubulin polymerization state alter the local electrical properties of the cell?** Does MT shortening alter the local spatiotemporal electrical properties? Can shortening of one MT trigger intracellular events driven by this electrical change?
Intracellular biophysics	Long term	**What is the ratio of ionic transport among these three modes?** 1. Lumen transport 2. Outer surface transport 3. Nanopore transport How to distinguish between these conductance modes experimentally?
Intracellular biophysics + nanodevice applications	Short term	**How do MT-MAP interactions change when exposed to electric fields?** Do electric fields cause biochemical changes in the cytoskeleton?
Nanodevice	Medium	**How do MTs interact with acoustic waves?**

applications	term	Ca MT electrical properties be used for electromechanical coupling?
Nanodevice applications	Medium term	**How does conductance depend on MT length and diameter?** Unclear due to the presence of nanopores and ionic 'leakage' through outer surface.
Intracellular biophysics + medical applications	Medium tern	**What is the effect of insulating membranes on MT coupling to a.c electric fields?** How does the presence of pores in these membranes influence MT coupling? How do these results correlate to the effects of a.c electric fields within living cells?

Table 2.2. A list of 10 challenges for MT bioelectricity.

3. Measuring the resistance and capacitance of the microtubule network in a cell-like environment[2]

ABSTRACT

In this chapter, we used impedance spectroscopy to show that while microtubules at physiological concentrations increase solution capacitance, free tubulin has no appreciable effect. Further, we observed a decrease in electrical resistance of solution, with charge transport peaking between 20-60 Hz in the presence of microtubules, consistent with recent findings that microtubules exhibit electric oscillations at such low frequencies. We were able to quantify the capacitance and resistance of the MT network at physiological tubulin concentrations to be 1.27×10^{-5} F and 9.74×10^{4} Ω. Our results show that in addition to macromolecular transport, microtubules also act as charge storage devices through counterionic condensation across a broad frequency spectrum. We conclude with a hypothesis of an electrically tunable cytoskeleton where the dielectric properties of tubulin are polymerization-state dependent.

INTRODUCTION

Since the tubulin dimer possesses a high negative electric charge and a large intrinsic high dipole moment [79, 165], MTs have been implicated in electrically-mediated biological roles [166-169]. They have been modelled as nanowires capable of enhancing ionic transport [125, 170], and simulated to receive and attenuate electrical oscillations [21, 133, 167, 171]. In solution, MTs have been shown to align with applied electric fields [63, 79, 87, 127-128, 172]. Recently, MTs have also been modelled as the primary cellular targets for low-intensity (1-2 V), intermediate-frequency (100-300 kHz) electric fields that inhibit cancer cell proliferation, in particular glioma [64, 66, 173].

---

[2] This chapter was published as a research article Kalra, Aarat P., Patel Sahil D., Bhuiyan Asadullah F., Jordane Preto, Scheuer Kyle G., Mohammed Usman, Lewis John D., Rezania Vahid, Shankar Karthik, and Tuszynski Jack A. "Investigation of the Electrical Properties of Microtubule Ensembles under Cell-Like Conditions." *Nanomaterials* 10, no. 2 (2020): 265.

Indeed, MTs have been reported to decrease buffer solution resistance [127-128], leading to a conductance peak at TTField-like frequencies [81]. While these studies show that MTs are highly sensitive to external electric fields, answers to the questions 'How do MTs effect a solution's capacitance?' and 'What is the capacitance of a single MT?' are still elusive and crucial to the determination of the dielectric properties of living cells. The tubulin concentration in mammalian cells varies in the micromolar range (~10-25 μM) [174-175]. *In vitro*, polymerizing tubulin at such high concentrations can lead to the formation of entangled networks, confounding quantification of the individual MT response to electric fields. Electro-rotation, dielectrophoresis and impedance spectroscopy are thus performed using low concentrations of tubulin, in the nanomolar regime, to enable robust observation of individual MTs.

MT formation and stability are known to be optimal in buffers with ionic strength between 80 and 100 mM [109, 111]. A background of BRB80 (which consists of 80 mM PIPES, 2 mM $MgCl_2$ and 0.5 mM EGTA, containing ~46mM $PIPES^{2-}$, ~36mM $PIPES^{-}$, ~68mM Cl^{-}, ~160mM K^{+}, and ~2mM Mg^{2+} [79]), is thus used to study the dynamics and mechanical properties of MTs. To study their electrical properties however, the usage of such high ionic-strength solutions has historically been problematic because any dielectric attenuation caused by MTs is overwhelmed by the noise and high conductivity from the background. In the low-frequency regime (1 Hz-100 kHz), two approaches have thus far been used to estimate the dielectric properties of MTs and tubulin. One is to electrically observe low concentrations of MTs (tubulin concentration in the nanomolar regime) in the presence of low ionic strengths [81, 88, 127-128, 176]. Such studies overlook the intrinsic ionic concentration of mammalian cytosol, which varies between 200 to 500 mM depending on the cell type [130-131]. Another approach to electrically interrogate MTs is to dry them: the conductivity of the buffer is nullified by evaporation, leaving polymeric tubulin behind [177-178]. In a physiological situation however, MTs are solvated by the highly conductive and noisy cytosol.

Here, we report on our efforts overcome the barrier posed by a high ionic strength by performing electrochemical impedance spectroscopy (EIS) on cellular concentrations of tubulin. We have been able to successfully observe differences in impedance using a background of BRB80 itself. Surprisingly, we find that MTs increase the solution capacitance of BRB80 whereas free tubulin does not, implicating a difference in electrical properties based only on the morphology of this protein solute. We also report a 'reversal' in the resistive behaviour of MTs compared to BRB80, with a reduction in solution resistance peaking in the

20-60 Hz region, a finding consistent with recent reports showing that polymerized tubulin quasi-resonantly responds to electric oscillations at ~39 Hz [21, 133]. Using an equivalent circuit model for MTs, we experimentally determine the capacitance and resistance of the MT network to be 1.27×10^{-5} F and 9.74×10^{4} Ω respectively, at physiological concentrations of tubulin. Our values indicate that the polymerization of tubulin into MTs alters spatial and temporal charge distribution, altering the electrical properties through charge storage in the cell.

MATERIALS AND METHODS

Tubulin reconstitution

Rhodamine-labelled tubulin solution was prepared using previously published protocols [81]. Lyophilized unlabelled tubulin powder (Cytoskeleton Inc; T240) was reconstituted in BRB80 supplemented with 1 mM GTP, and mixed with Rhodamine labelled tubulin (Cytoskeleton Inc; TL590m) in a final labelling ratio of 1:15. Aliquots were snap-frozen and stored at -80 °C.

MT polymerization and stabilization

MT polymerization was performed by incubating 45.45 μM tubulin aliquots in a 37 °C water bath for 30 minutes. BRB80 solution was heated alongside tubulin during the first 15 minutes of polymerization. Subsequently, BRB80 was incubated at room temperature, and paclitaxel solution (Cytoskeleton Inc, TXD01; 2 mM stock) was thawed at room temperature alongside it. After 30 minutes of tubulin polymerization brought to completion, 100 μL of BRB80 was added to 5 μL of 2 mM paclitaxel. For preparing 0.222 μM MTs, 99.5 μL of this solution was added to 0.5 μL tubulin solution. For 2.222 μM MTs, 95 μL of this solution was added to 5 μL tubulin solution. For 22.225 μM MTs, 5 μL of this solution was added to 5 μL of tubulin solution. For preparing BRB80T, 45 μL of this solution was added to 45 μL of BRB80.

For tubulin stabilization, 2 μL of colchicine stock solution (Sigma-Aldrich, C9754; 5 mM in DMSO) was added to 100 μL BRB80. For preparing 0.222 μM tubulin, 99.5 μL of this solution was added to 0.5 μL unpolymerized tubulin solution. For 2.222 μM tubulin, 95 μL of this solution was added to 5 μL unpolymerized tubulin solution. For 22.225 μM tubulin, 5 μL of this solution was added to 5 μL of unpolymerized tubulin solution. For preparing BRB80C, 45 μL of this solution was added to 45 μL of BRB80.

Fluorescence imaging of MTs

Imaging was performed on a Zeiss Examiner.Z1 microscope using a Hamamatsu EMCCD C9100 camera, a Zeiss plan-Apochromat 1.4 NA 63x lens. After pipetting MT solution (2-5

μL) onto a glass slide (VWR 48382-173) a coverslip (VWR 48393-070) was placed on the solution, allowing it to spread. The microscope used an EXFO X-Cite 120 fluorescence source and excitation and emission filters of 535 nm and 610 nm, respectively. Exposure times between 50 ms and 300 ms were used for imaging to validate the presence of MTs.

Electrode design and device construction

Each 'plate' in the parallel-plate contact device was formed by FTO (Fluorine-doped Tin Oxide)-coated glass slides (Sigma Aldrich, 735140). The slides were cleaved to dimensions of 1.5 mm x 10 mm x 50 mm for the upper contact and 1.5 mm × 27 mm × 50 mm for the lower contact. The cleaving dimensions were set using 3D printed devices that were placed as holders (The Shack, University of Alberta; Fig. B1 in Supplemental Information). The slides were ultrasonicated and subjected to Reactive Ion Etching (RIE) using a 5-minute exposure to oxygen plasma (Oxford Instruments, NGP80) to remove surface particulate matter. 70 μm thick double-sided tape was used as a spacer, which formed a chamber of dimensions 3 mm × 1.25 cm × 70 μm. The top electrode was placed using a separate 3D-printed holder device. Once the device was constructed using the above protocol, solution was perfused into the chamber using a pipette and a filter paper for suction. We used flat copper electrode clips in a three-electrode configuration to connect to our capacitor device. The counter electrode was connected to the lower electrode, and the working and reference electrodes were connected to the top electrode of our device.

Impedance measurements

Experiments were conducted using Electrochemical Impedance Spectroscopy (EIS) on a Zahner Zennium impedance analyzer. The parallel-plate contact device was placed into the 3D-printed holder for stabilisation. The contacts from the machine were connected to the parallel-plate device using flat-faced copper alligator clips. A three-electrode configuration was used: the counter electrode was attached to the lower contact of the parallel-plate device, whereas the working electrode was attached to the upper contact with the reference electrode orthogonally clipped onto the clip of the working electrode. Within the Thales Z3.04 environment, the Potentiostat Mode was ON; the stabilisation delay was set to 1 second, the rest potential drift tolerance was set to 250 μV , V_{rms} was set to 5 mV. Solutions were perfused into the experimental chamber using a micropipette tip at one opening, and a filter paper at the other opening for suction, similar to protocols used for TIRF (Total Internal Reflection Fluorescence)

microscopy [179]. The frequency range of the EIS measurement was set from 4 MHz to 1 Hz and data were subsequently collected.

Data analysis

MT and tubulin samples were analyzed using data from five to seven days of experiments. Each day consisted of three to seven solutions for each concentration being tested, with one frequency sweep per solution. Readings of each sweep were saved as a .csv file, and next sample was loaded by solution exchange method. Water was run as the first solution for each day of experiments. BRB80T was run prior to MT solutions, and BRB80C were run prior to the free tubulin containing solutions. MT- and free tubulin-containing solutions were run on separate days, in increasing order of concentration. MATLAB (The Mathworks; Natick, MA) scripts were used for data analysis. Fitting to the real and imaginary components of impedance was performed using the function lsqnonlin. Initial guess values for the MT network resistance and capacitance were 10^5 F and 10^{-5} Ω , respectively, based on visual inspection of raw data. The initial guess values for the nominal series resistor, R_H, were set at 1.78, 0.6 and 0.4 Ω for with tubulin concentrations of 0.222, 2,222 and 22.222 μM, respectively. The 95% confidence intervals were determined using the function nlparci. Error propagation was performed assuming no relationship between various days of data collection.

RESULTS

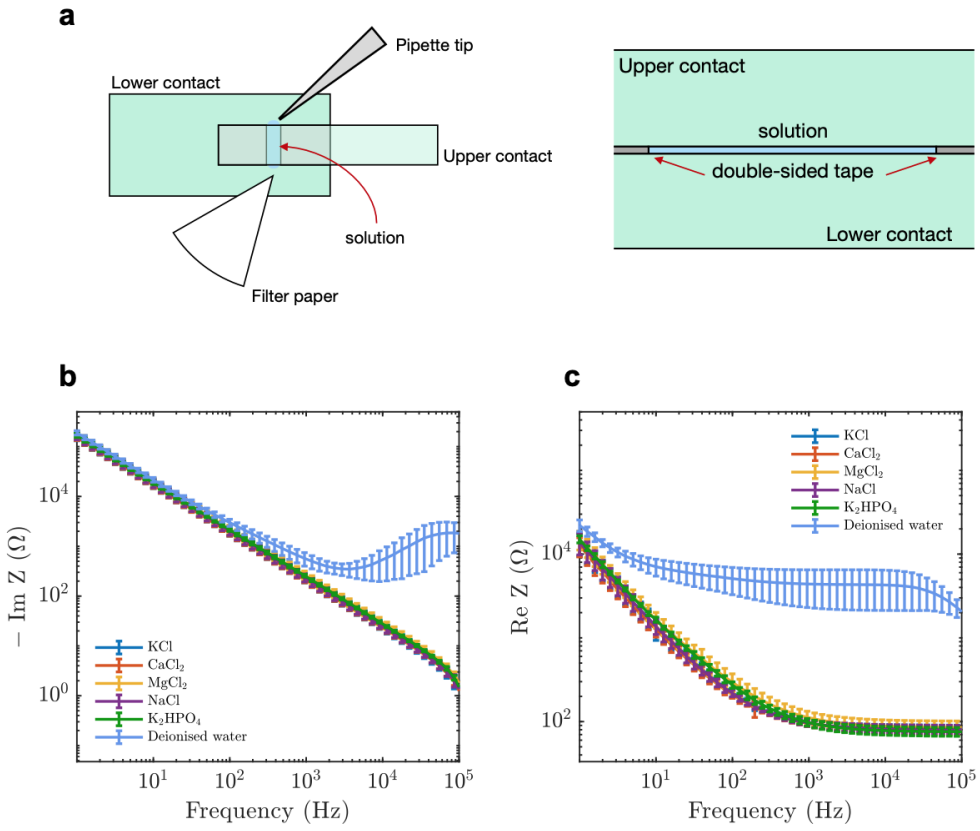

Figure 3.1. A parallel-plate contact device to measure the impedance properties of MTs compared to tubulin. The operation of the parallel plate device showing (a) top view (left) and side view (right). The upper and lower contacts, double-sided tape and solution are labelled in green, gray and blue, respectively. (b) Imaginary component of impedance for electrolytic solutions at 100 mM and de-ionized water. (c) Real component of impedance for electrolytic solutions at 100 mM and de-ionized water. Data display average values collected between 15 and 21 times. Error bars represent standard deviation. For measurement setup and perfusion protocols, see Materials and Methods.

A parallel-plate contact device can accurately measure dielectric properties of ionic solutions found within the cytosol

To determine the differences in the dielectric properties of solution caused by the presence of MTs, we aimed to create an electrode geometry that would be experimentally robust and easily modelled. We fabricated an FTO-coated parallel-plate contact device (Fig. 3.1a, Materials and Methods, which allowed EIS using a solution-exchange method.

We started by performing EIS on electrolytes found in the cytosol and observed a decrease in the imaginary component of impedance as a function of decreasing input frequency (Fig. 3.1b). The total impedance of our system was given by:

$$Z = r_c + r_s/(1 + (r_s\,\omega C)^2) + j(\omega L_c - (r_s^2\,\omega C)/(1+(r_s\,\omega C)^2)) \quad (3.1)$$

Here, Z is the impedance, ω is the angular frequency (given by $2\pi f$ where f is the input voltage frequency), C is the system capacitance, L_c is the cable inductance, r_s and r_c are the solution and cable resistances respectively. We also observed a decrease in the real component of impedance as a function of decreasing input frequency (Fig. 3.1c). Such a trend is expected from Warburg impedance [180-181] and is in accordance with the equation:

$$Z_{complex} = (A_\omega)/\sqrt{\omega} + (A_\omega)/(j\sqrt{\omega}) \quad (3.2)$$

Here, $Z_{complex}$ is the complex impedance and A_ω is the Warburg coefficient. Our circuit simplifies to the equation below if we ignore the effect of cable inductance ωL_c , at frequencies below 10^5 Hz:

$$Z = r_c - j/\omega C \quad (3.3)$$

Our results using various electrolytes emulated previous data [182-184] and validated the experimental setup for further analysis.

3.2. MTs increase solution capacitance compared with background, while unpolymerized tubulin does not have a significant effect

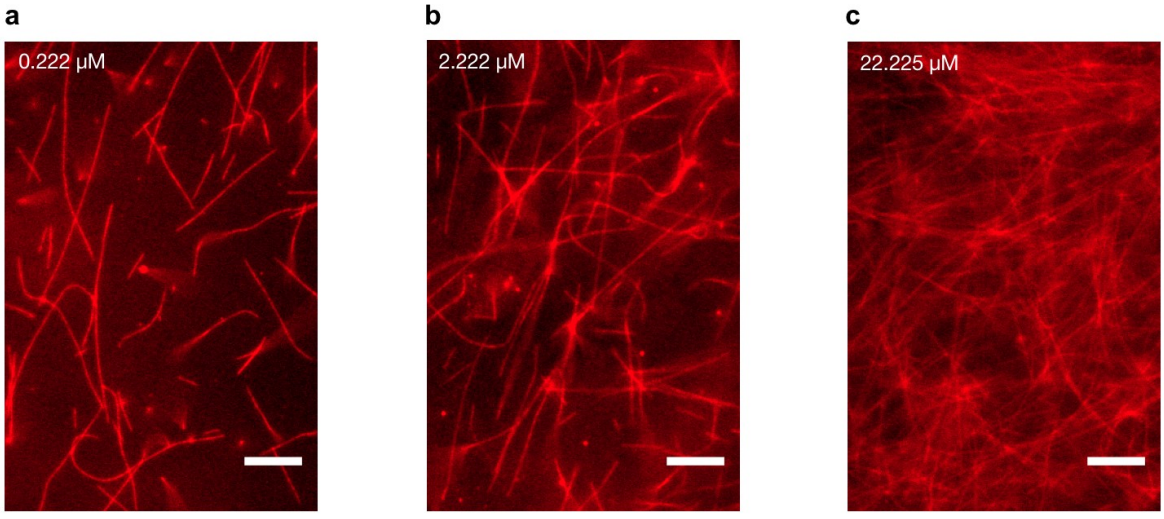

Figure 3.2. Microtubule imaging at different tubulin concentrations. Polymerization was performed using 45 μM tubulin, and MTs were stabilized with 50 μM paclitaxel, and subsequently diluted to a final concentration of (a) 0.222 μM tubulin (b) 2.222 μM tubulin (c) 22.225 μM tubulin, respectively. Scale bars represent 10 μm. For imaging setup and polymerization protocols, see Appendix D (Materials and Methods).

We reconstituted and polymerized fluorescent tubulin from a stock of 45.45 μM tubulin solution (Appendix D). MTs were stabilised using 50 μM paclitaxel [30, 185] and imaged using an epi-fluorescence microscope. On diluting MT concentration across three orders of magnitude (0.222, 2.222 and 22.225 μM tubulin), we observed that while individual MTs at low concentrations were separated by large distances, those at cellular concentrations formed enmeshed networks reported previously (Fig. 3.2 a, b, c) [186]. Such interconnected MT networks are utilized by molecular motors for long-range macromolecular transport [187-188]. Here, their presence demonstrated successful MT polymerization for electrical characterization.

We performed EIS on BRB80, BRB80T (BRB80 supplemented with 50 μM paclitaxel; background for all MT-containing solutions), and MT-containing solutions in increasing order of concentration. We subtracted impedance values obtained for BRB80T alone from those in MT containing solutions, to determine the MT contribution to impedance. Our results showed that with an increasing MT concentration, the value of imaginary impedance became more negative, resulting in positive impedance differences (Fig. 3.3a, b, c, d). This effect was highest at 1 Hz and decreased with a decreasing input frequency. Experiments with unpolymerized tubulin at the same concentrations were performed using the identical procedure, but using BRB80C (BRB80 was supplemented with 50 μM colchicine) as a background, to prevent MT nucleation [34, 189]. Results with tubulin did not show an appreciable deviation at any concentration. Based on the above we can conclude that polymerization of tubulin into MTs alters their ensemble electrical properties, increasing the solution's capacitance on forming MTs and their networks. An increase in the solution's capacitance due to MTs has previously been modelled, [77, 170, 190] indicating an increase in charge storage as free tubulin polymerizes.

Microtubules increase solution resistance compared to background with this effect's reversal observed at low frequencies

Next, we investigated the differences between MTs and tubulin in the real component of impedance (solution resistance). Previous studies using nanomolar tubulin concentrations and

low ionic strengths (1-12 mM) have indicated that MTs enhance charge-transport in solutions [81, 127, 191]. To evaluate if this observation held true at physiologically relevant tubulin concentrations and at higher ionic strengths, we also analyzed the real component of impedance. Addition of both MTs and tubulin generally led to an increase in solution resistance, with MTs having a higher resistance at low frequencies (1-20 Hz) compared to unpolymerized tubulin. Unexpectedly, a 'reversal' of this behaviour was observed at higher frequencies as MTs began to lower solution resistance compared to tubulin. The reversal took place gradually between 10 and 300 Hz, with a peak between 20 and 60 Hz (Fig. 3.4 a, b, c). Interestingly, within this range, we also found that the addition of MTs lowered solution resistance compared to background buffer BRB80T.

Such a reversal in resistance between microtubules and tubulin has not been reported before. Because the extent of this reversal decreased with decreasing concentration, this result also displays the utility of our 'cell-like' approach. Our results are consistent with predictions of an increase in solution conductance at ~39 Hz [21, 133], and predicted an increase in solution conductance in the range that we observe, indicating that the conductance behaviour at such frequencies was due to MT- generated electrical oscillations.

It is worth noting that this region falls within the gamma frequency regime, implicating such quasi-resonant phenomena as a possible explanation for the source of low frequency intraneuronal electrical oscillations. No such reversal was observed for the corresponding frequency range in the imaginary impedance values.

The microtubule network can be described as an RC circuit in parallel.

Our next aim was to quantify the resistance and capacitance of the microtubule network. The slope of approximately negative unity on the impedance difference curve suggested that the microtubule network resulted in the addition of a capacitive element to the solution. We examined several combinations (data not shown) but a parallel RC circuit to represent the entire MT network provided the best fit to observed curves (Fig. 3.5):

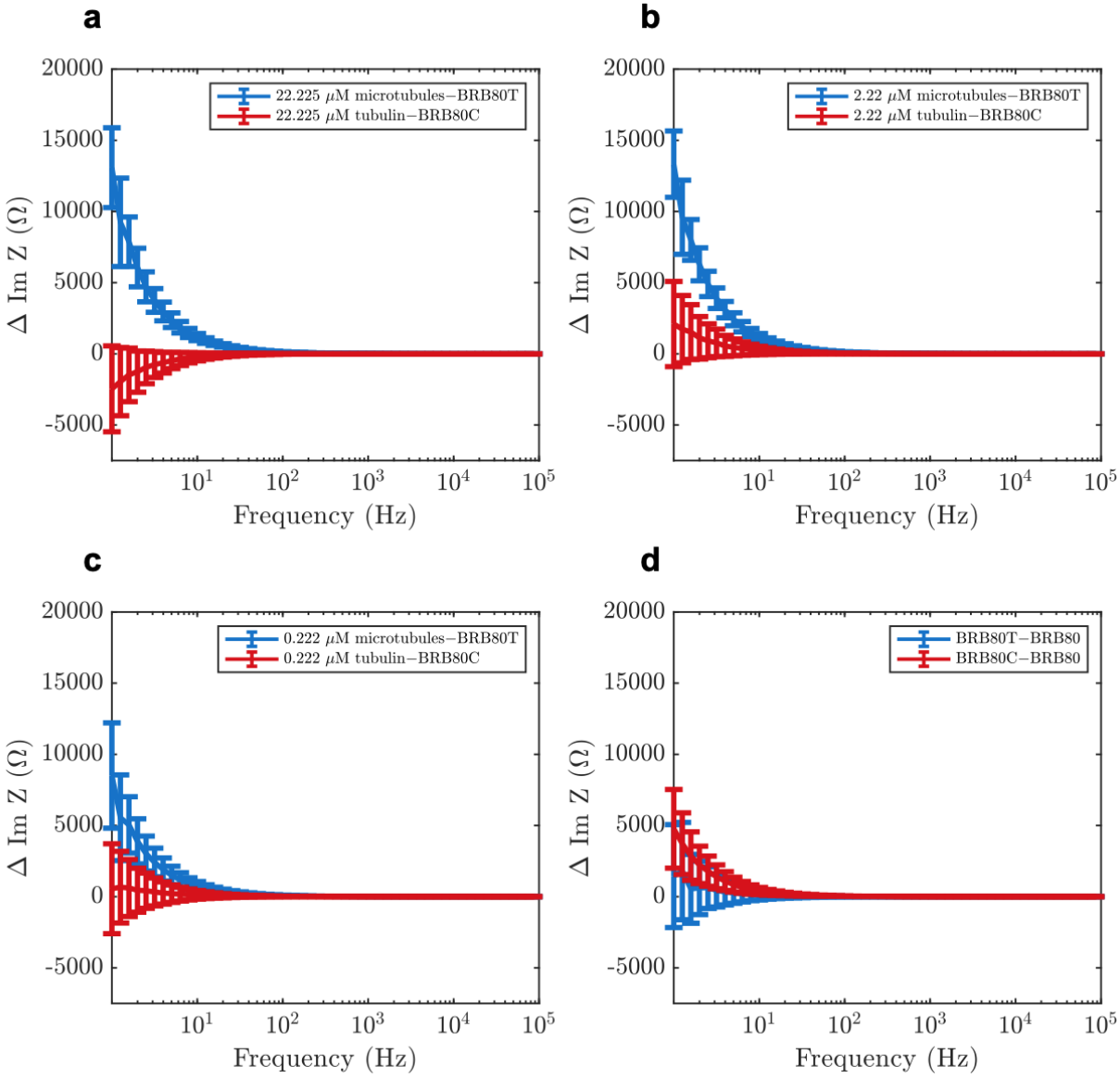

Figure 3.3 Mean differences in the imaginary component of impedance as a function of decreasing input AC frequency at total tubulin concentrations of (a) 22.225 μM (n = 22 experiments for tubulin, n = 21 for MTs), (b) 2.222 μM (n = 35 experiments for tubulin, n = 49 for MTs) (c) 0.222 μM (n = 35 experiments for tubulin, n = 49 for MTs), (d) comparison of the effects of paclitaxel (BRB80T) and colchicine (BRB80C, n = 49 experiments for BRB80T, n = 35 for BRB80C, n = 84 experiments for BRB80). Error-bars represent standard deviation.

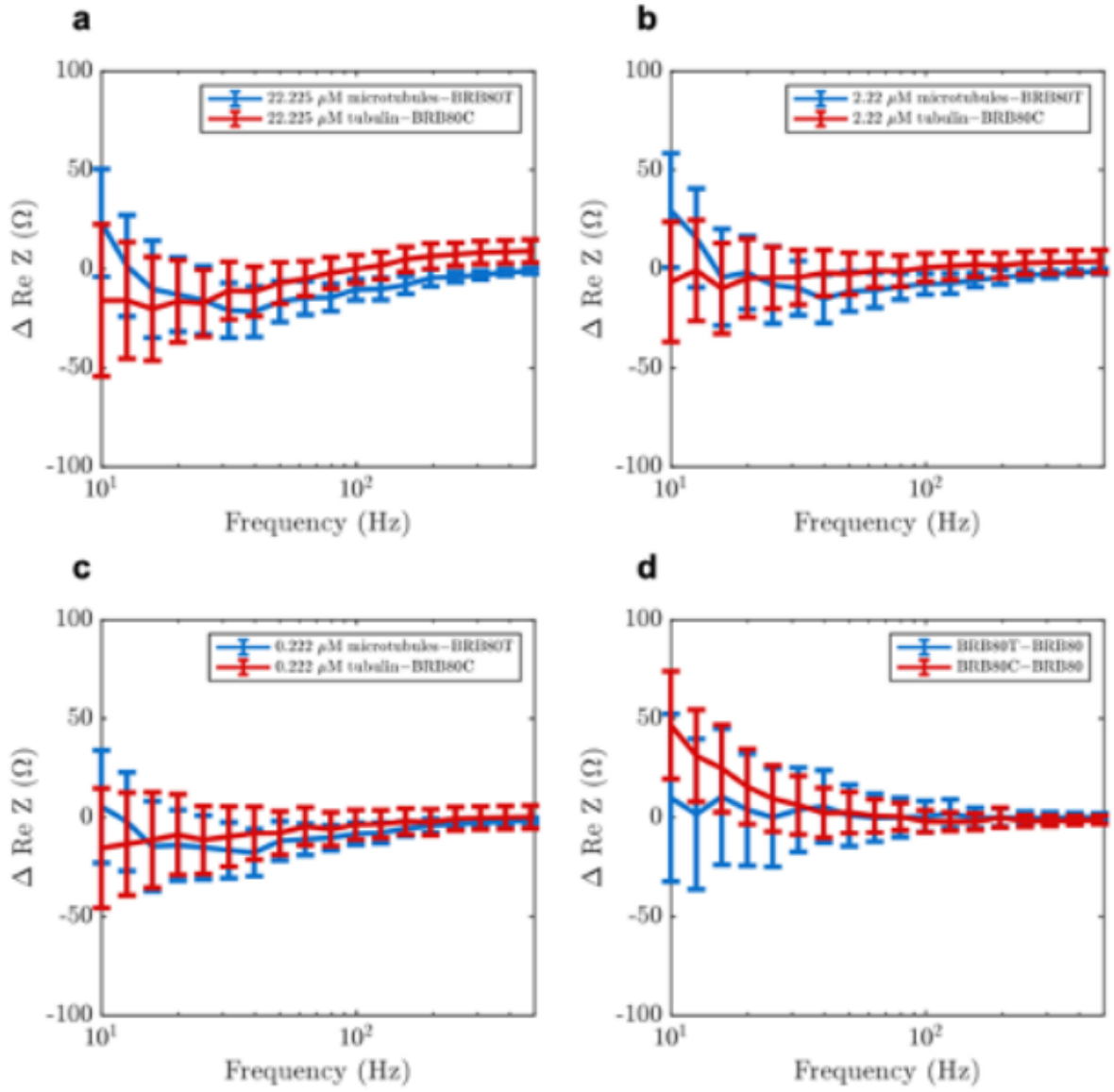

Figure 3.4. Mean differences in the real component of impedance as a function of decreasing input a.c. frequency at total tubulin concentrations of (a) 22.225 μM, (b) 2.222 μM, (c) 0.222 μM, (d) comparison of the effect of paclitaxel and colchicine on impedance. Error-bars represent standard deviation.

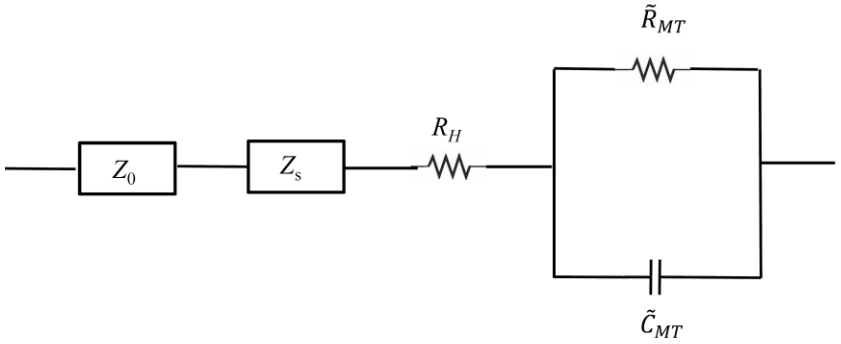

Figure 3.5. The equivalent electrical circuit model representing the microtubule network as a parallel RC circuit, with network resistance R_{MT} and capacitance C_{MT}. The external element has impedance Z_0, while solution has impedance Z_s. R_H is the small constant resistance that is ascribed to small fraction of unpolymerized tubulin that is present in MT containing solutions.

We modelled the impedance caused by external circuit elements and BRB80T as Z_o and Z_s respectively, as shown in Figure 3.5. The net impedance of the background BRB80T was thus given by:

$$Z_{buffer} = Z_0 + Z_s \qquad (3.4a)$$

Denoting the impedance, resistance and capacitance of the entire MT network by Z_{MT} , R_{MT} and C_{MT} respectively, the impedance for the circuit with MTs is given by:

$$Z_{MT+buffer} = Z_0 + Z_s + R_H + Z_{MT} \qquad (4b)$$

where,

$$1/Z_{MT} = 1/R_{MT} + j\omega C_{MT}$$

Additionally, the impedance differences between solutions with and without MTs are given by:

$$\Delta Z = Z_{MT+buffer} - Z_{buffer} = R_H + Z_{MT} \qquad (3.5)$$

where

$$Z_{MT}=R_{MT}/(1+(\omega C_{MT}R_{MT})^2) - j(\omega C_{MT}R_{MT}^2)/(1+(\omega C_{MT}R_{MT})^2) \qquad (3.6)$$

We subsequently fit experimental impedance difference curves shown in Fig. 3.3 to real and absolute value of imaginary parts of ΔZ using R_H , R_{MT} and C_{MT} as our fit parameters. Here, R_H is a resistance ascribed to the nominal fraction of unpolymerized tubulin present in MT containing solutions. The fitted curves are displayed in Figure 3.6 and the optimal fit parameters are listed in Table 3.1.

[Tubulin] (μM)	C_{MT} (F)	δC_{MT} (F)	R_{MT} (Ω)	δR_{MT} (Ω)	R_H (Ω)	δR_H (Ω)
22.222	1.27×10^{-5}	1.48×10^{-7}	9.74×10^{4}	1.18×10^{4}	2.12	40.61
2.222	1.25×10^{-5}	1.67×10^{-7}	1.00×10^{5}	1.40×10^{4}	0.61	34.79
0.222	2.01×10^{-5}	3.38×10^{-7}	9.97×10^{4}	2.82×10^{4}	0.41	31.95

Table 3.1. Fit parameters attained by fitting the real and imaginary components of impedance to equation 3.6. Fit parameters represent effective capacitance C_{MT}, and resistance R_{MT} introduced into the solution through the addition of the MT network at different concentrations. R_H is the small constant resistance that is ascribed to small fraction of unpolymerized tubulin that is present in MT containing solutions. δR_{MT} , δC_{MT} and δR_H correspond to 95% confidence intervals for the fit parameters. Corresponding graphs are displayed in Fig. 3.6.

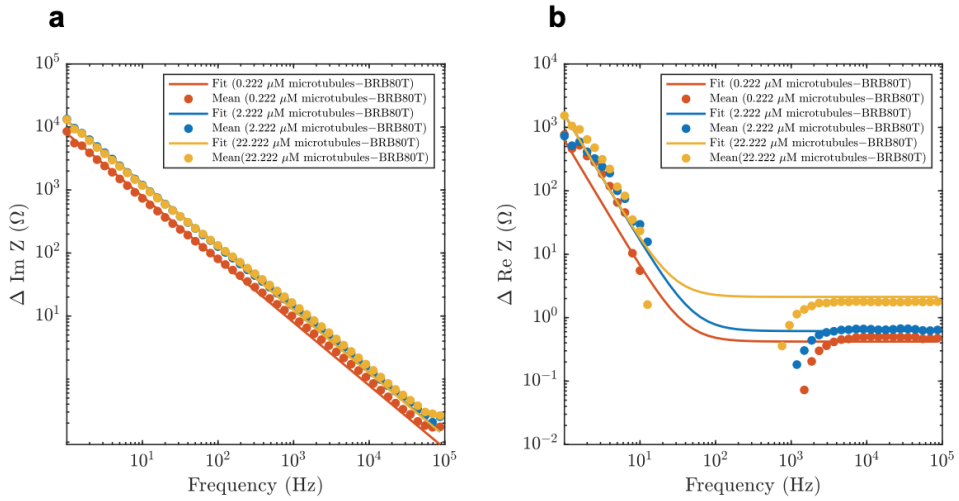

Figure 3.6. Mean differences of (a) imaginary and (b) real impedance curves for 0.222 μM, 2.222 μM and 22.222 μM, are fitted with the model described in Eq. 3.5 and Fig. 3.5. Fit parameters and confidence intervals are displayed in Table 3.1. Values in the range 10-1000 Hz was not fit due to negative differences in resistance from background BRB80T solutions. For detailed fitting methodology, see Appendix B.

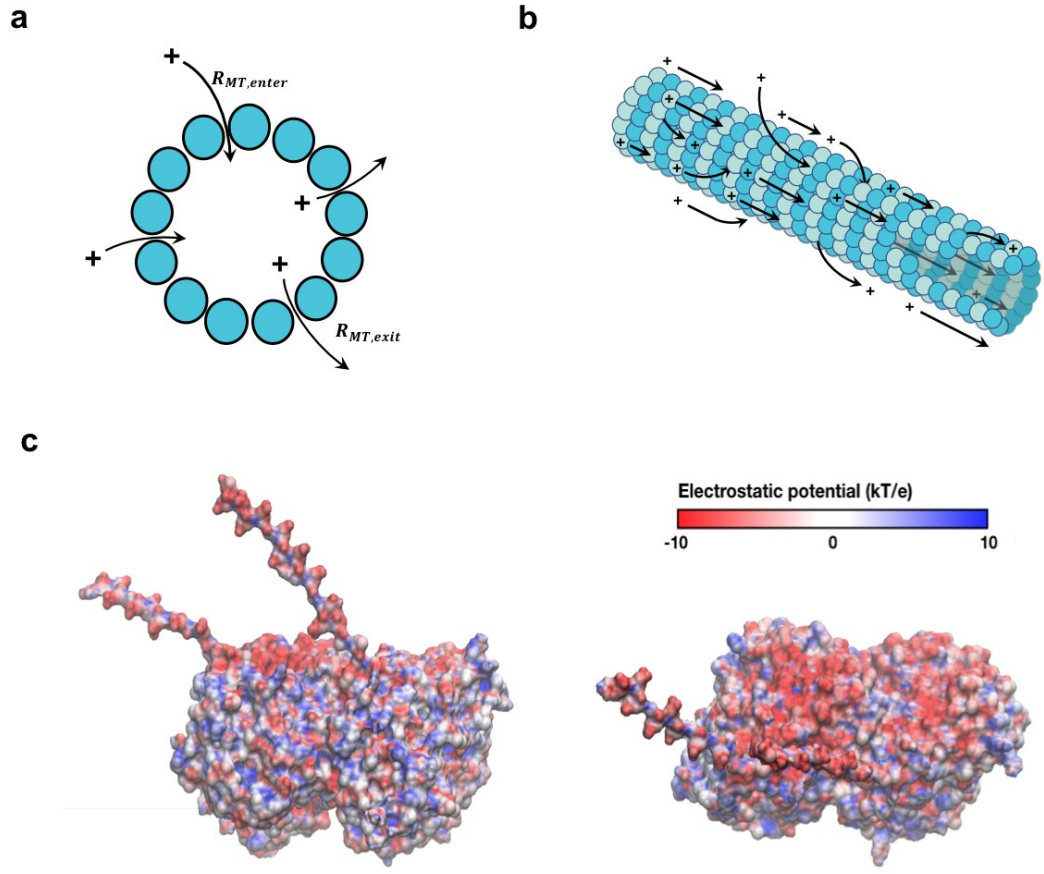

Figure 3.7. Schematic of charge transport along and across a MT. (a) A representation of charge flow across the MT cross section through nanopores present between adjacent protofilaments. (b) A representation of charge flow through both inner and outer modes along a MT. Arrows depict charge flow via both mechanisms, enabling MT charge storage across a broad spectrum of frequencies, and charge transport at low AC frequencies in the cell. (c) Side view (left) and top view (right) of the tubulin dimer, displaying distribution of electrostatic potential at different locations. The negatively charged C-termini face towards the solution and contains ~50 % of the total negative charge on a tubulin dimer.

DISCUSSION

Our measurements using a parallel plate contact device reveal interesting electrical properties of MTs at physiological concentrations. Unlike studies exposing MT-containing solutions to non-uniform electric fields [81, 87, 127-128], our device allowed robust quantification of electrical impedance in the presence of spatially uniform electric fields. Our results show that the addition of the MT network mimics a parallel RC element placed in series with the high-ionic strength solution, with a nonlinear dependence on MT number. Unpolymerized tubulin did not alter capacitance significantly, indicating changes in electrical properties of tubulin as it polymerizes.

The physical underpinnings of an increased capacitance

An increase in capacitance arises from dense counterion condensation on the MT surface. This has been extensively predicted and simulated to arise from a variety of sources [14, 125, 132, 170, 190]. Firstly, the negative charge of the tubulin dimer attracts counterions in solution, leading to the presence of a double layer and depletion region outside the microtubule surface [14, 125, 170, 191]. The charge distribution in the MT protein wall is also highly non-uniform, with the outer surface containing approximately four times the charge compared to the inner surface [132](Fig. 3.7 c). This asymmetry between the inner and outer electrostatic potentials serves to enhance capacitance and is responsible for the abnormally large dipole moment of the tubulin dimer [165]. The asymmetry also manifests through C-terminal 'tails' composed of 10-12 amino-acids, that can extend 4-5 nm outwards from each tubulin monomer. These slender C-termini tails are highly negative, containing about 50 % of the charge of the tubulin dimer [95]. As they stretch outwards into the solution in a pH and ionic strength dependent manner, they increase the effective area of the tubulin dimer and significantly contribute to the overall MT capacitance [125, 170].

Coherent oscillations of these C-terminal tails are modelled to generate solitonic pulses of mobile charge along the outer surface of a MT, creating ionic currents along its' length [17, 170, 190]. Ions from the bulk solution are also modelled to be pumped into the hollow MT lumen through nanopores in its' wall, resulting in charge accumulation inside the cylindrical MT over time [77]. A recent study using molecular dynamics simulations showed that the permeability of the MT lumen was significantly higher for Na^+ and K^+ as opposed to Ca^{2+}, allowing for free movement of selective ions into the MT lumen across its porous surface [132]. To the best of our knowledge, our findings are the first to experimentally quantify this resistance encountered by

charge flow across the MT cross section. These results implicate not only ionic movement along the microtubule axis, but also across and inside it, enhancing the modelled roles of MTs as complex subcellular nanowires.

Manning's theory of polyelectrolyte solutions predicts the conditions for ionic condensation on charged polymer surfaces provided a sufficiently high linear charge density is present on these surfaces creating an ionic concentration depletion area surrounding them [192]. The sum total of the charges on polymer surfaces and the associated counterions decreases to values dependent on the valence of the counterions and the Bjerrum length, which is the distance from the polymer surface at which the Coulomb energy of the screened surface charges equals the thermal energy. The double layer of surface charges and counterions separated by the Bjerrum length can be viewed as having capacitor-like properties. Although the Manning theory was originally developed for such polyelectrolytes as DNA, it was also applied to actin filaments [193] and MTs [15]. For actin filaments, its application explained the observed lossless transmission of electric pulses along the filament lengths. In the case of MTs, it provided a plausible explanation of unusual amplification of injected electrical signals that propagated along these nanowires. The calculated Bjerrum length for MTs was found to be approximately 6.7×10^{-10} m [17, 125]. Both actin filaments and MTs have been represented in these models by cable equations with effective real and imaginary impedance due to the viscosity of the solution resisting ionic flows and the capacitive properties of the ionic double layers around the filaments, respectively [15, 193]. The capacitance for a single ring of a MT including C-termini was calculated to be approximately 1.3×10^{-15} F [125]. When extended to 20 μm, (representative of the length of a single MT for our measurements), the predicted value would be $C = 3 \times 10^{-12}$ F, although an experimental confirmation of this prediction is not directly available through our measurements or in any previous work. We note the relatively weak dependence of network capacitance on MT concentration, and assign it to the random spatial locations and directional orientations of MTs in our solution. Indeed, the conductivity of randomly distributed RC networks has been shown to scale weakly with the number of elements in the network [194]. Additionally, qualitative similarities can be found in the models of random resistor and capacitor networks [195]. In particular, there is a frequency-dependence cross-over for both conductance and impedance in these networks due to percolation-type conduction where resistors are dominating the conduction process at low frequencies while capacitors are high frequencies. We intend to develop a quantitative model for our experimental observations in a subsequent publication.

Implications for the cell

Our work, which utilizes cell-like tubulin and ionic concentrations for the first time, indicates a cellular role for microtubules as wires that store charge. Neuronal environments where MTs are spontaneously nucleated from free tubulin, such as growth cones, would experience large capacitance changes over short bursts of time. This ability would significantly impact action potentials, that are known to depend strongly on the local charge distributions [196]. Additionally, ionic movement across the MT wall would enhance their roles as attenuators of local cation distributions. In nonneuronal environments, transient ionic currents around a MT during mitosis could impact MT dynamics and potentially influence chromosome segregation. Specifically, Ca^{2+} ion storage/flow about a MT would trigger its' depolymerization, whereas waves of Mg^{2+} or lowering in the local pH (increasing H^{+}) would lead to MT stabilization [197-198]. The attraction of Zn^{2+} or Mn^{2+} ions in the vicinity would lead to formation of two-dimensional tubulin polymers [102, 106]. Properties of the cytoplasm such as polarizability and relative permittivity would get severely attenuated due to the presence of MTs in the vicinity. Due to the polymerization state of tubulin altering solution capacitance, our findings implicate a temporal evolution of capacitance and ionic flows as the ratio of MTs to free unpolymerized tubulin changes [199-201]. MT lattice defects, that take place when a tubulin dimer is missing in a MT wall [202-203], would cause a large ionic flux to develop at the defect site. Such localised shifts in charge distributions would be most significant at the MT end, where large localized charge fluxes would form due to sudden changes in both ionic resistance and capacitance. Free/polymerized tubulin would thus regulate local and global electrical properties, creating spatially dynamic gradients of charge storage and flux. We envision a cytoskeleton that, in addition to transporting macromolecules, stores and transports ionic signals and electrical information across the cytoplasm (Fig. 3.7 a, b).

Our findings can be coupled with a vast array of bio-nanodevices that utilize MTs and MAPs (microtubule-associated proteins) for construction of bio-nanotransporters and bio-actuators [49, 204-207]. Under specific conditions, MAP-MT systems are capable of repositioning macromolecules [83 208], directionally transporting microtubules [63, 209] and even drive their movement within zero-mode waveguides [210] and inorganic nanotubes [53]. Storage of electrical charge and its' transport along MTs can be coupled to such cutting-edge mechanical MAP-based devices to develop a wide range of nano-actuators and nano-sensors.

When compared to cells, the rates of MT nucleation and polymerization are significantly lower in BRB80. This difference can be attributed to the absence of MAPs and macromolecular crowding [211-212]. Mammalian cells contain high concentrations of K^{+} ions (140-300 mM) [130-

[131], which, in addition to MAPs and molecular crowding agents, would be included in a future study to attain physiological equivalence. We are in the process of performing DC (direct-current) measurements, determine the contribution of MTs to impedance relaxation time and evaluate the voltage dependence of capacitance on MT-containing solutions. Interestingly, this aspect has been discussed previously: the inductance of a single protofilament is calculated to be <1 fH [125]. Further investigation is required to experimentally confirm these predictions.

CONCLUSIONS

We used EIS to compare the complex impedance of MT- and tubulin-containing solutions. A physiologically relevant, high ionic strength buffer (BRB80) created a high noise, low impedance background, which was countered through the use of physiological concentrations of tubulin. While the presence of MTs increased solution capacitance, unpolymerized tubulin did not have any appreciable effect. In a study that is the first of its kind to the best of our knowledge, we determined the capacitance and resistance of the MT network at physiological tubulin concentrations to be 1.27×10^{-5} F and 9.74×10^{4} Ω. We envision a dual electrical role for MTs in the cell: that of charge storage devices across a broad frequency spectrum (acting as storage locations for ions), and of charge transporters (bionanowires) in the frequency region between 20 and 60 Hz. Our findings also indicate that the electrical properties of tubulin dimers change as they polymerize, revealing the potential impact of MT nucleation and polymerization on the cellular charge distribution. Our work shows, that by storing charge and attenuating local ion distributions, microtubules play a crucial role in governing the bioelectric properties of the cell.

4. Investigating the response of tubulin to DMSO-containing electrolytes[3]

ABSTRACT

Microtubules are frequently modelled as one-dimensional bionanowires that act as ion transporters in the cell. In this chapter, we used dynamic light scattering (DLS) to measure the hydrodynamic diameter of tubulin in the presence of a polar aprotic co-solvent. We found that the hydrodynamic diameter increased with increasing DMSO volume fraction, almost doubling at 20% DMSO. To evaluate if this was due to an enlarged solvation shell, we performed reference interaction site model (RISM) simulations and found that the extent of solvation was unchanged. Using fluorescence microscopy, we then showed that tubulin was polymerization competent even in the presence of colchicine, and thus inferred the presence of oligomers in the presence of DMSO, which points to its mechanism of action as a microtubule polymerization enhancer. Tubulin oligomers are known to form when microtubules depolymerize and are controversially implicated in microtubule polymerization as well. We show that DLS may be used to monitor early-state microtubule polymerisation and is a viable alternative to fluorescence and electron microscopy-based methods. Our findings showing that DMSO causes tubulin oligomerization are thus of critical importance, both for creating bio-inspired nanotechnology and determining its biophysical roles in the cell.

INTRODUCTION

α, β -tubulin is a globular protein heterodimer that polymerizes to form hollow cylindrical tubes termed microtubules (Fig. 4.1), which play a variety of roles in the cell, such as generating mechanical forces to separate daughter cells, segregating chromatids during mitosis, forming a

[3] This chapter was published as a research article Kalra, Aarat P., Kar Piyush, Preto Jordane, Rezania Vahid, Dogariu Aristide, Lewis John D., Tuszynski Jack A., Shankar Karthik. "Behavior of α, β tubulin in DMSO-containing electrolytes." *Nanoscale Advances* 1, no. 9 (2019): 3364-3371.

network for transport of macromolecules, and maintaining cell shape and rigidity in association with actin filaments and intermediate filaments to form the cytoskeleton.[1] Inside the cell, microtubules change their lengths through rapid polymerization/depolymerization cycles of free cytosolic tubulin dimers, a process termed dynamic instability.[213-214] Microtubule length-shortening events, termed 'catastrophes', involve *en masse* release of tubulin oligomers into the cytosol.[215] Due to the crucial roles they play, tubulin and microtubules are key targets for anti-tumor drugs.[216-218] In this context, understanding the factors and mechanisms triggering microtubule formation and catastrophe events are critical. Among several key factors, the cytoplasm may strongly affect tubulin/microtubule diffusion processes and mediate or screen specific interactions within or between tubulin dimers, thus altering microtubule dynamics. To understand the role of the cell environment on microtubule dynamics, aspects such as catastrophes and rescues have been studied and shown to be altered in different solvents. For example, glycerol and polyethylene glycol (PEG) are reported to create an 'excluded volume' via macromolecular crowding, and drastically lower association rate constants to reduce the critical concentration for nucleation of microtubules in vitro.[211, 219] The presence of dimethyl sulfoxide (DMSO) has also been shown to reduce the critical concentration required for microtubule polymerisation by 8 to 10 times.[220-222] While the effects of these solvents on microtubule dynamics have been quantified and detailed, the effect on tubulin dimers themselves and their ability to aggregate or polymerize, while hypothesized to alter the solvent structure around tubulin, is not well understood.

Due to the negative charge and high dipole moment of the tubulin dimer, counterions have been modelled to condense around microtubules, and to couple with the phonon modes of the microtubule lattice.[125, 170] The nature of the solvation shell around tubulin, which is crucial in determining protein structure and function,[223-226] has been modelled to form a 'slip layer' around tubulin, and act as a passage for ionic charge transport.[227-228] Characterizing the solvation shell in aqueous media and different solvents is thus of critical importance.

An increasing interest in the use of tubulin for applications in electronics,[81, 229] nanotechnology[230] and biosensors [231] elevates the importance of characterising this protein and its assemblies regarding its response to different environments. In this paper, we characterize the response of tubulin dimers to DMSO using Dynamic Light Scattering (DLS) as a first step towards understanding its response to different solvents. Using Reference Site Interaction Model (RISM) simulations, we exclude the possibility of the solvation shell being significantly altered in the presence of DMSO and point towards oligomerization and aggregation as reasons for an increased hydrodynamic diameter. In addition to involvement in microtubule

catastrophes, oligomers are also reported to play roles in microtubule elongation and are important to characterize biophysically.[232-233] Our research is aimed at studying the biophysical properties of tubulin dimers and oligomers in both aqueous and hostile environments, with a view towards both understanding the biophysics of the cell and eventually developing biologically-inspired nanotechnology.

METHODS

Tubulin stock preparation

General tubulin buffer (80 mM PIPES pH 6.9, 2 mM $MgCl_2$, 0.5 mM EGTA; Cytoskeleton Inc; BST01-010) was purchased in powdered form and reconstituted as prescribed by the vendor. This solution was filtered and stored at 4°C for subsequent use. Lyophilized tubulin stock (5 mg; Cytoskeleton Inc; T-240) was reconstituted using 20 µL of microtubule cushion buffer (General Tubulin buffer supplemented with 60% Glycerol) added to 180 µL of G-PEM buffer (general tubulin buffer supplemented with 1% GTP). Tubulin solution was snap frozen in liquid nitrogen and stored in 5 µL aliquots at -80 °C.

Measurement of hydrodynamic diameter

DLS was performed using a final concentration of 1.2 µM tubulin and 1.4 µM colchicine in the presence of BRB8. Briefly, 2 µL of colchicine (dissolved in DMSO) was added to 498 µL of BRB80. 11 µL of this solution was added to 0, 7.5, 15, 22.5 and 30 uL of filtered DMSO to form 0, 5, 10, 15 and 20 % DMSO (v/v) solutions respectively. 4 µL of tubulin stock was added to this solution and the volume was made up to 150 µL using de-ionized water. The temperature of the system was set to 25°C using the measurement file. The final solution pH for all cases of DMSO volume fraction was calculated and determined to be approximately 6.9. Once samples were prepared, a Nano-ZS (Malvern Instruments) machine was used for the determination of hydrodynamic diameter. The equipment used for our DLS measurements was a Malvern Nano-ZS located at the National Institute for Nanotechnology (NINT) facility, in Edmonton, Alberta, Canada. The incident laser wavelength was 633 nm, and the instrument automatically set the angle of the detector by accounting for the particle size. Data acquisition was performed by three runs for each sample, and each run entailed multiple/repetitive measurements of particle size, ensuring statistical significance.

Tubulin labelling

Lyophilized tubulin (20 µg; Cytoskeleton Inc, TL-590m) was reconstituted in a 1:5 labelling ratio with unlabelled tubulin, in 10% glycerol and 1 mM GTP, as recommended. Briefly, 4 µL of G-PEM buffer was added to tubulin powder, followed by 1 µL of microtubule cushion buffer. Tubulin solution was snap frozen using liquid nitrogen and stored in 5 µL aliquots at -80°C.

Epifluorescence imaging

Epifluorescence microscopy was performed using a Zeiss Axio Examiner microscope, and a Zeiss 63x Plan-Apochromat objective. 2 µL of solution was pipetted onto Silane-prep glass slides (Sigma-Aldrich; S4651) for imaging. Excitation and emission filters of 535 nm and 610 nm, respectively, were used. An exposure of 300 ms and a sensitivity of 100 were kept constant for all images.

Modelling methodology

The 3D RISM method was used to estimate the 3D equilibrium density distribution of solvent around the tubulin dimer [234]. 3D RISM is based on the Ornstein-Zernike (OZ) equation, which expresses the density distribution in terms of direct and indirect spatial correlation functions. This module is available within the AMBER MD package. Terming $g_\gamma(r)$ the density distribution of atoms of type γ at position r, we introduce the total correlation function $h_\gamma(r)$ as $h_\gamma(r) = g_\gamma(r) - 1$, where $g_\gamma(r) = 1$ and $h_\gamma(r) = 0$ for bulk solvent, i.e., when $r \to \infty$. The total correlation function can in turn be expressed from the direct correlation function leading to the following equation:

$$h_\gamma(r) = \sum_\alpha \int c_\alpha(r - r')\chi_{\alpha\gamma}(r')dr'. \quad (4.1)$$

In eq. (4.1), $\chi_{\alpha\gamma}(r)$ stands for the site-site solvent-susceptibilty for atom types α and , which was pre-calculated using 1D-RISM by integrating the dielectrically consistent RISM (DRISM) equation coupled with the Kovalenko-Hirata (KH) closure equation. A temperature of 300 K was used for our calculations. 3D-RISM was then applied to compute the 3D density distribution $g_\gamma(r)$ of solvent atoms around our prepared tubulin oligomers.

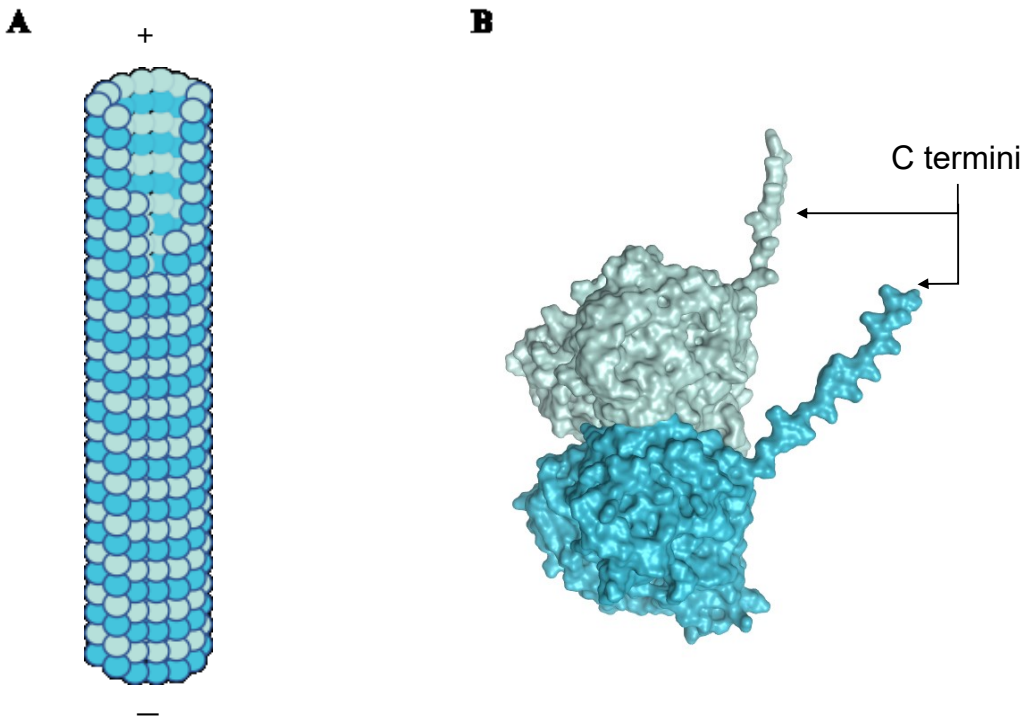

Figure 4.1. α,β tubulin dimers form long filamentous nanowires termed microtubules. (A) A schematic showing a side view of microtubules, which are hollow cylindrical nanostructures. α,β tubulin dimers stack linearly to form microtubules. (B) A three-dimensional structure of α and β subunits of tubulin, displaying C-terminal 'tails', that carry approximately 50% of the net negative charge on the dimer.[127]

RESULTS AND DISCUSSION

Dynamic Light Scattering

The hydrodynamic diameter of tubulin was measured in BRB8 (Bradley's reconstitution buffer with 8 mM PIPES) as opposed to the standard buffer BRB80 used for microtubule polymerization, since the low ionic strength solution reduces the effect of ionic condensation on the surface of tubulin. The Stokes-Einstein equation, on which size determination using DLS is based, uses temperature, viscosity and refractive index to determine the hydrodynamic diameter of solute particles. Values used for tubulin are shown in Table 4.1. Our results showed that, consistent with the expected size of tubulin shown previously using X-ray diffraction, DLS and fluorescence correlation spectroscopy (FCS) measurements,[235-237] the hydrodynamic

diameter of tubulin by number distribution in a BRB8 solution was 7.038 ± 0.0703 nm, (Fig. 4.2 A, B and C).

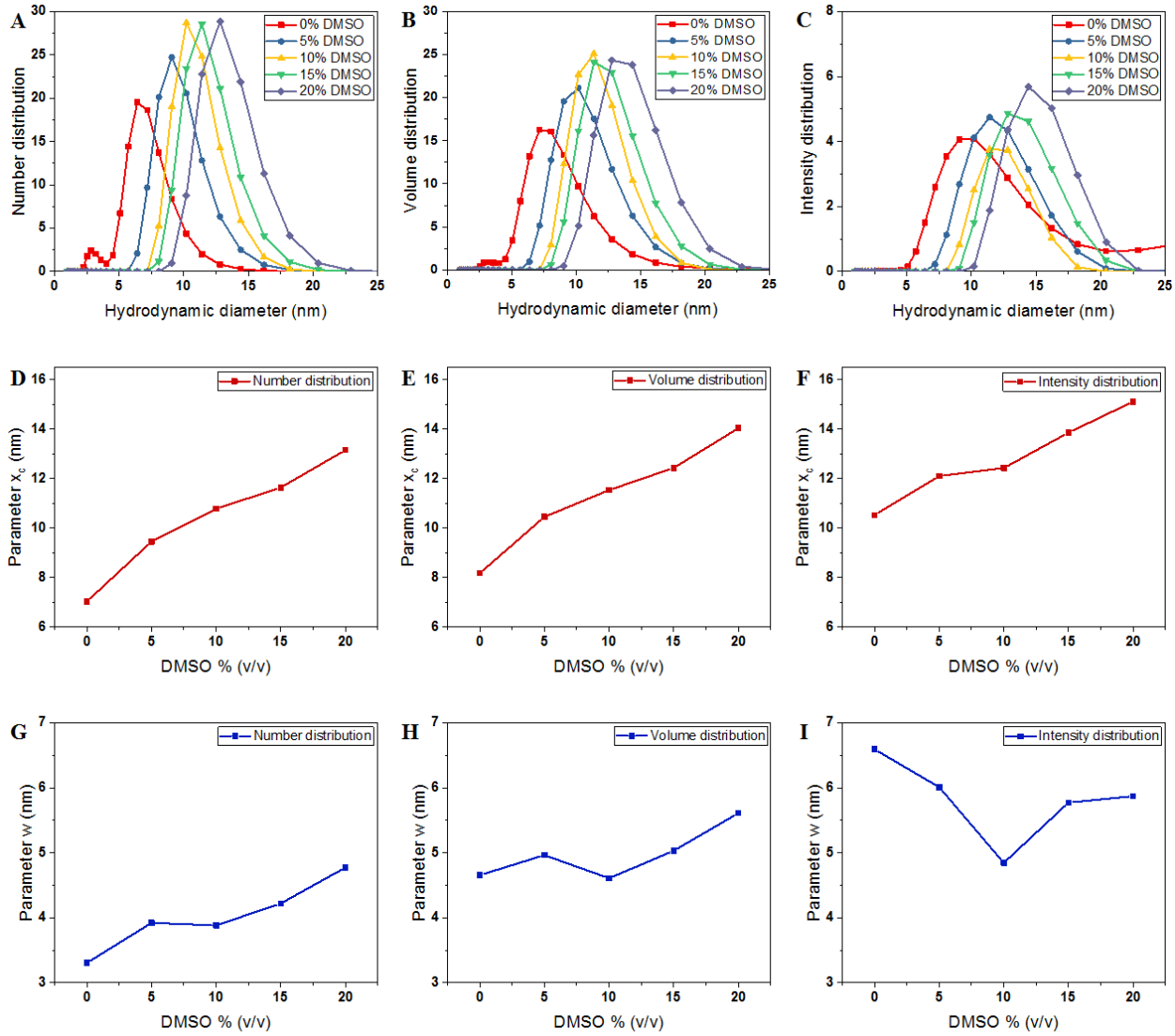

Figure 4.2. Hydrodynamic size of tubulin dimers measured using DLS. (A-C) Displays the hydrodynamic dimeter of the tubulin dimers determined by number, volume and intensity distributions. (D-F) Displays the peak of the Gaussian fit in the number, volume and intensity distributions, respectively, represented by the parameter x_c. (G-I) Displays the FWHM of the Gaussian fit in the intensity plots, represented by parameter *w*.

The DLS instrument determined the size of the particles using three interpretations: intensity plots showed which size had the highest scattering intensity, the volume plots showed which size occupied the highest volume and the number density plots, which showed what sized

particles were in greatest abundance. After obtaining data from the DLS experiment, we plotted these values and fitted them to a Gaussian as shown in the equation below:

DMSO % (v/v)	Parameter x_c (nm)		Parameter w (nm)		Reduced Chi-Sqr	Adj. R-Square
	Value	Standard Error	Value	Standard Error		
Number distribution						
0	7.038	0.070	3.306	0.176	1.425	0.957
5	9.459	0.068	3.922	0.170	1.432	0.971
10	10.784	0.064	3.883	0.157	1.518	0.975
15	11.641	0.069	4.220	0.169	1.449	0.976
20	13.155	0.077	4.773	0.190	1.467	0.976
Volume distribution						
0	8.178	0.094	4.656	0.246	1.165	0.957
5	10.457	0.091	4.965	0.229	1.349	0.967
10	11.536	0.072	4.608	0.178	1.175	0.977
15	12.436	0.083	5.031	0.206	1.250	0.974
20	14.036	0.086	5.611	0.213	1.139	0.977
Intensity distribution						
0	10.527	0.194	6.593	0.524	0.170	0.912
5	12.105	0.091	6.010	0.230	0.049	0.9775
10	12.433	0.064	4.847	0.159	0.020	0.983
15	13.856	0.089	5.772	0.222	0.048	0.977
20	15.113	0.077	5.872	0.190	0.043	0.983

Table 4.1. A schematic displaying the variation of Gaussian fit-parameters x_c and w within equation (1) with increasing DMSO concentration in solution. Number, volume and intensity fits are shown. Other fit parameters are shown in Supplemental Information.

$$y = y_0 + \frac{Ae^{\left(\frac{-4ln(2)(x-x_c)^2}{w^2}\right)}}{w\sqrt{\frac{\pi}{(4ln2)}}} \tag{4.1}$$

Here, the coefficients y_0, w,and A represent the baseline height, FWHM (full width at half maximum) and area under the Gaussian curve respectively, while x_c represents the position of the peak on the x-axis. As shown in (Fig. 4.2 D, E and F), our results showed that value of the hydrodynamic diameter and the fit parameter x_c increased with increasing DMSO volume. Interestingly, we also saw an increase in the width of Gaussian fits, represented by the parameter w (Table 4.1, Fig. 4.2 G, H and I). This pointed us towards three possibilities (1) an increased solvation shell of tubulin (2) tubulin oligomerization leading to a larger particle size (3) the formation of aggregates of tubulin in the presence of DMSO.

First, to investigate if this increase was a result of changing solvation dynamics as opposed to the formation of oligomers and aggregates, as hypothesized in earlier reports [220], we used computational modelling estimates to evaluate the thickness of the solvation shell.

Computational modeling estimates of the hydrodynamic diameter

Solvent molecules surrounding proteins in their vicinity may interact strongly with protein structures and may therefore contribute to the value of the hydrodynamic radius R_H. For instance, the increase of R_H observed in Fig. 4.4C for increasing DMSO concentration may be partly explained by an increase of the solvation shell thickness, which would lead to an increase in the hydrodynamic radius of tubulin. In order to determine how the solvation shell contributes to the value of R_H, molecular structural analysis of tubulin dimers and small oligomers was performed.

Structures of tubulin oligomers were obtained by first downloading the Protein Data Bank (PDB) cryo-EM structure 3J6F, which consists of a 3X3 lattice of tubulin dimers as part of a GDP-bound microtubule, and by trimming the structure in order to get the desired types of oligomers. Extracted structures include free tubulin dimer (1X1), two laterally bound dimers (2X1), two longitudinally bound dimers (1X2), as well as 3X1, 2X2 and 1X3 structures. C-termini together with GTP and GDP cofactors were not considered, as they were assumed to minimally contribute to the hydrodynamic radii of the molecules. Energy minimization was run on each oligomer structure in implicit solvent using the AMBER molecular dynamics (MD).[238] The hydrodynamic radius R_H of each oligomer in the absence of solvent was computed by first estimating their radius of gyration R_g, which satisfies:

$$R_g{}^2 = \frac{1}{M}\sum_{i=1}^{N} m_i(r_i - r_{mean})^2 \quad (4.2)$$

where r_i are the coordinates of each atom of the oligomer ($1 \leq i \leq N$), m_i are their mass, $M = \sum_i m_i$ is the total mass and r_{mean} are the coordinates of the center of mass of the protein. Next, the hydrodynamic radius of each oligomer was deduced from the well-known relation.[239]

$$R_g = (3/5)^{1/2} R_H = 0.77 R_H, \quad (4.3)$$

which has been shown to hold for a large panel of proteins. Values of hydrodynamic diameter for each oligomer with no solvent considered are given in the second column of Table 4.2.

In order to investigate how the hydrodynamic diameter changes when solvent is considered, the equilibrium distribution of solvent molecules around each oligomer structure was predicted using the 3D-RISM utility available within the AMBER package. Using 3D-RISM has an advantage over explicit solvation that it doesn't require periodic boundary conditions, resulting in improved handling of long-range effects. It is worth noting, however, that RISM ignores kinetically-limited phenomena. Simulations were carried out at 0% v/v, 5% v/v, 10% v/v of DMSO/water concentration, consistent with the DLS experiments described previously. Note that only water and DMSO molecules were considered for our simulations, i.e., no ions or additional species were added to the solvent. This is because the concentration of ions and other chemical species used in our experimental setup, which includes PIPES, used as a buffer agent, and $MgCl_2$, which is below 1 mM, were assumed to have a negligible influence in the formation of the solvation shell. 3D-RISM requires information about the static dielectric constant ε of the solution as an input. To estimate ε for DMSO/water mixtures, the following equation was applied:[240]

$$\varepsilon = \left[\left(\varepsilon_{DMSO}^{1/3} - \varepsilon_{H2O}^{1/3}\right) v_{DMSO} + \varepsilon_{H2O}^{1/3}\right]^3, \quad (4.4)$$

where $\varepsilon_{H2O} = 78.9$and $\varepsilon_{DMSO} = 47.29$ are the static dielectric constants of pure water and pure DMSO solutions, respectively [240] and v_{DMSO} is the volume fraction of DMSO. Note that $v_{DMSO} = 0$ leads to $\varepsilon = \varepsilon_{H2O}$and $v_{DMSO} = 1$ to $\varepsilon = \varepsilon_{DMSO}$, respectively. Other parameters and theory related to 3D-RISM are provided in the material and section method. After using 3D-

RISM to provide the distribution function around protein oligomers, the placevent.py program can be applied to generate solvent molecules around the solute and determine their coordinates (Fig. 4.3A and 4.3B).

Oligomer	Vacuum	Water	DMSO (5%)	DMSO (10%)
1x1	4.52	4.8	4.8	4.8
1x2	7.74	8.00	8.00	8.00
1x3	11.2	11.36	11.38	11.38
2x1	6.02	6.28	6.28	6.28
3x1	8.06	8.24	8.24	8.24
2x2	8.78	8.98	8.98	8.98

Table 4.2. Hydrodynamic diameter (in nm) for different tubulin oligomer configurations (1x1 = tubulin dimer, 2x1= two laterally bound dimers, 1x2 = two longitudinally bound dimers, as so on. Each column displays oligomer hydrodynamic diameter values in various solvents.

To estimate the hydrodynamic diameter, the radius of gyration was first estimated. The following formula was applied:

$$R_g{}^2 = \frac{I_{prot} + I_{solv}}{M}, \tag{4.4}$$

where I_{solv} is the moment of inertia of the solvation shell estimated as: $I_{solv} = \sum_\alpha \int \rho_\alpha(r)(r - r_{mean})^2 \, d^3r$. α indicates the type of solvent atoms considered (e.g., for pure water, α correspond to hydrogens or oxygen). $\rho_\alpha(r)$ gives the excess solvent mass due to the solute that is discounted by the solvent displaced by the solute, i.e.: $\rho_\alpha(r) = m_\alpha c_\alpha h_\alpha(r)$, where m_α is the mass of atoms of type α, c_α is the bulk concentration $c_\alpha = N_\alpha/V$ and $h_\alpha(r)$ is the total correlation function at r, given as an output of 3D-RISM computations (see material and methods section). Similar to Eq (1), I_{prot} is the moment of inertia of the protein given by $\sum_{i=1}^{N} m_i(r_i - r_{mean})^2$. M and $r_{mean}$are the total mass and the center of mass of the system, respectively, including the solvation shell. Eq. (4.2) was then used to estimate the hydrodynamic diameter. Values of the hydrodynamic diameter including the solvation shell are provided in the last three columns of Table 4.2 corresponding to 0% v/v, 5% v/v, 10% v/v of DMSO/water concentration.

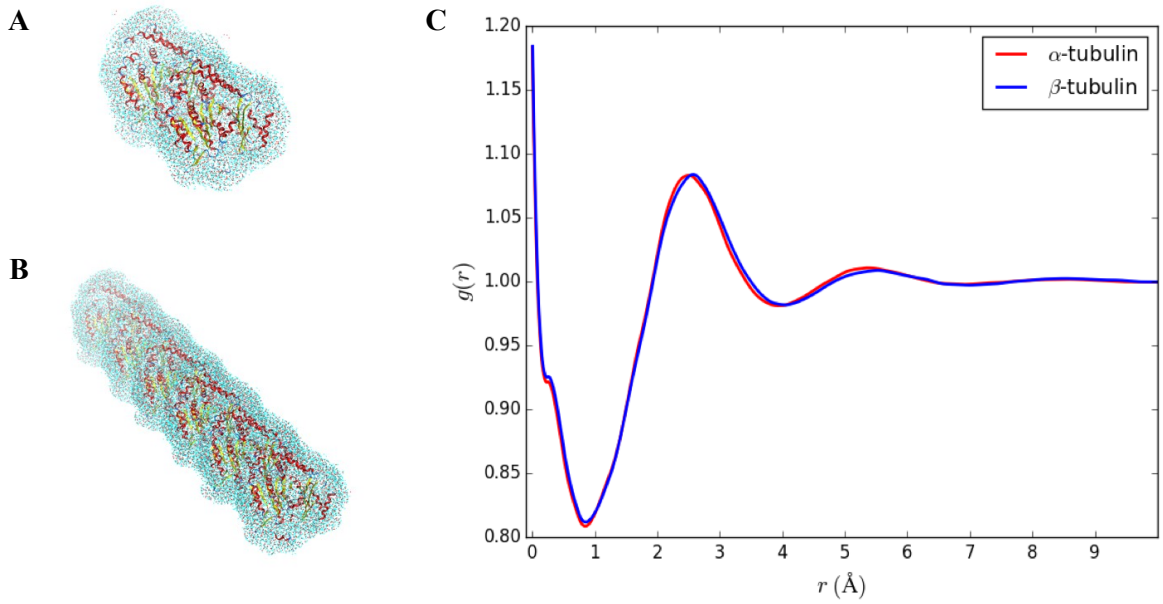

Figure 4.3. (A) Shape of the solvation shell surrounding a tubulin dimer. Positions of the water molecules were predicted using the placevent.py script. Only water molecules characterized by $g(r) > 1$, i.e., for which the density is larger than the bulk density, were kept. (B) Shape of the solvation shell surrounding three longitudinally bound dimers (bottom, 1X3 case). (C) Average radial density distribution $g(r)$ of oxygen atoms in pure water for α and β tubulin monomers. $g(r) = 1$ corresponds to the bulk density.

An estimate of the hydrodynamic diameter for a single dimer, as given by the first row of Table 4.2, was found to match with DLS results at 0% DMSO, suggesting no oligomerization or aggregation. However, we noticed from our 3D-RISM simulations that only a small change was observed in the hydrodynamic radius of tubulin oligomers because of the solvent. As shown in Table 4.2, only an increase of about1Å is found when considering the solvation shell. Besides, no significant differences in R_H were reported between the pure water case (3rd column of Table 4.1) and DMSO/water mixtures (4th and 5th columns of Table 4.2) suggesting that the presence of the solvation shell does not explain the increase of R_H observed in DLS experiments when the DMSO concentration is increased. This result appears reasonable assuming a protein will still have the same free energy regardless of solvent thus always influencing the same mass around it.

In order to corroborate values found in Table 4.1, an average radial distribution of solvent molecules close to the surface of tubulin was computed. Since α and β tubulin monomers are comparable to spherical objects, the density distribution $g(r)$, as provided by our 3D-RISM

simulations, was estimated for different values of polar $\theta\epsilon[0,\pi]$ and azimuthal angles $\varphi\epsilon[0,2\pi]$ starting from the center mass of each monomer. Then, the average distribution $g(r)$ was computed over all the θ and φ values. Fig. 4.3C shows such an average radial distribution for oxygen atoms in pure water, setting the protein surface to $r = 0$Å and the bulk density to $g(r) = 1$. The hydration shell thickness was taken as the distance between the protein surface and the first minimum of the radial distribution function. This distance corresponds to 0.9Å, which is close to the 1Å increaseobserved in the value of the hydrodynamic radius due to the solvent (see Table 4.2).

Epifluorescence microscopy

We used fluorescence microscopy to evaluate if the presence of DMSO was leading to tubulin oligomers being formed. We reasoned that if tubulin was indeed polymerizing as opposed to forming amorphous aggregates, we would see microtubules under a fluorescence microscope. Fig. 4.4 shows our results with epi-fluorescence microscopy of labelled-tubulin solutions. For imaging, we used the same concentrations and parameters as our DLS measurement, using 0%, 10% and 20% DMSO. While no polymers existed in the presence 0% and 10% DMSO, microtubules were observed in the presence of 20% DMSO. We thus inferred that tubulin was still polymerization competent, and that the increase in hydrodynamic diameter of tubulin as a function of DMSO volume fraction was due to the presence of oligomers and not amorphous aggregates. Interestingly, microtubule formation in these conditions was not expected for a variety of reasons. Firstly, tubulin concentration was an order of magnitude lower than the critical concentration required for microtubule formation at 37°C (1.2 μM as compared to ~22 μM)[241]. We note that experiments were performed at 25°C, further reducing the propensity for polymerization. Also, colchicine, a well-known inhibitor of microtubule formation[34, 189, 242] was added to all solutions (see Appendix D). All experiments were conducted at lower than normal ionic concentrations (in BRB8 as opposed to BRB80), further inhibiting polymerization, while simultaneously lowering counterionic condensation[111].

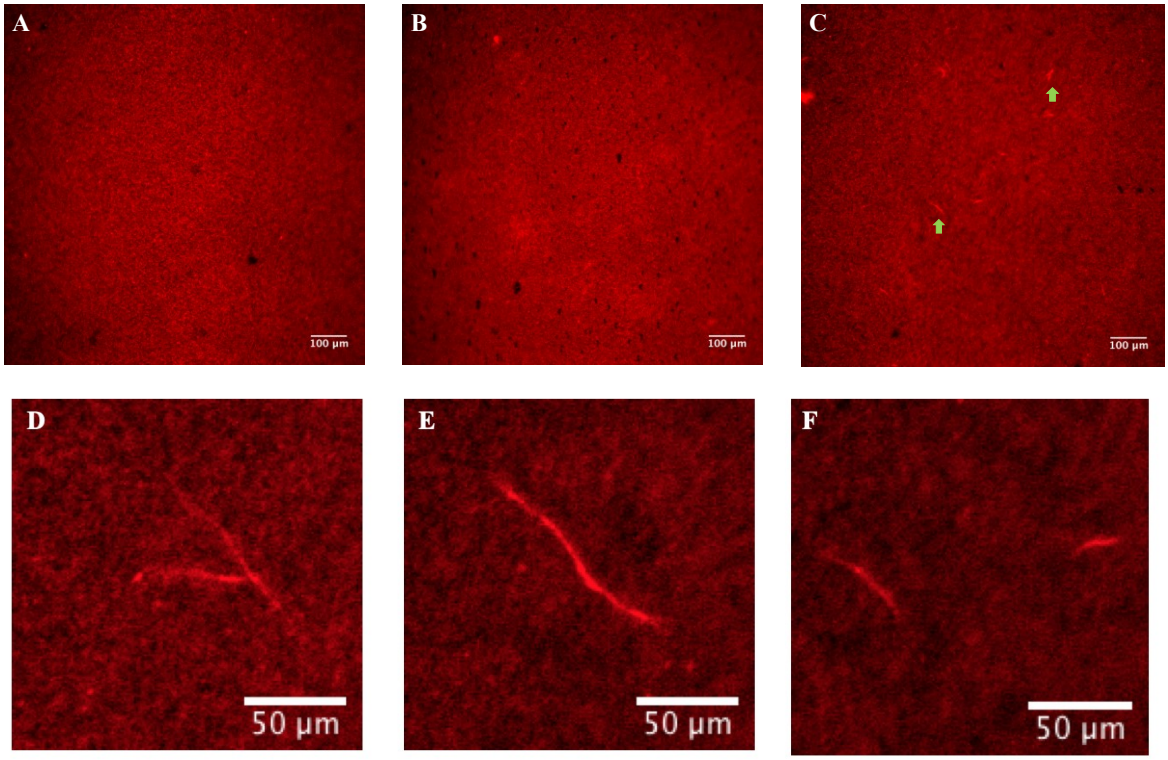

Figure 4.4. Epi-fluorescence microscopy to show that tubulin remains polymerization competent in the presence of increasing DMSO concentrations. (A-C) Images of 1.2 µM tubulin in 0%, 10% and 20% DMSO and 1.4 µM colchicine in BRB8 solution. The green arrows in C point towards microtubules. (D-F) Magnified images showing microtubule formation at 1.2 µM tubulin in the presence of 20% DMSO and 1.4 µM colchicine in BRB8 solution. For detailed experimental conditions and epi-fluorescence microscopy setup, see Appendix D.

In biochemical assays, DMSO is a commonly used solvent. DMSO is also used as a drug carrier in treatments for dermatological diseases[243], schizophrenia[244], amyloidosis and gastrointestinal disorders[245-246] . The presence of DMSO leads to tumor retardation in mouse breast cancer cells [247], loss of tumorigenic potential in human carcinoma cells[248], alters the biochemical and morphological properties of cancer cells[249] and decreases the permeability of breast cancer cells[250]. DMSO has also been suggested to act as a stimulator of a tumor suppressor protein HLJ1 in lung cancer cells[251]. We thus chose DMSO to study the response of tubulin to DMSO with a view to understand its biophysical effects on the cytoskeleton. Our findings showed that this polar, aprotic solvent did not appreciably alter the solvation shell around tubulin. Further, despite the presence of colchicine, tubulin oligomerization took place. Our approach using DLS to study tubulin polymerization is both novel and consistent with previous reports of DMSO enhancing tubulin polymerization[219-220].

CONCLUSIONS

The hydrodynamic diameter of tubulin was measured using DLS in the presence of increasing volume fractions of DMSO. In aqueous solvent, the hydrodynamic diameter was 7.04 ± 0.07 nm by number distribution, increasing as the volume fraction of DMSO was increased. Interestingly, our simulations using RISM showed that this was not a consequence of increased hydration in the presence of DMSO. Our work points towards the formation of tubulin oligomers in the presence of DMSO.

Unlike traditional techniques used to study microtubule dynamics such as fluorescence microscopy, electron microscopy and turbidimetry, DLS quantifies particle size at relatively fast temporal resolutions and requires nominal post-measurement analysis, (such as image reconstruction required for electron microscopy or sub-pixel tracking in fluorescence-based imaging methods). DLS is not hampered by photobleaching and is not affected by the diffraction-limited resolution obtained with a microscope, or other factors that confound imaging such as a high background noise. In the past, limitations with fluorescence-based imaging methods have been typically circumvented by the use of electron microscopy, which requires the sample to be stained prior to imaging, making it susceptible to aggregation and the presence of artifacts. Unlike electron microscopy, which is highly specialized and time consuming, DLS does not require any staining or labelling and is non-destructive, lending itself for use in quantification of various microtubule nucleation parameters.

For the quantification of microtubule dynamics and nucleation, an ideal combination would be the spatial resolution offered by EM, working in tandem with the temporal resolution offered by fluorescence-based methods such as TIRF (Total Internal Reflection Fluorescence) and CLIC (Convex Lens-Induced Confinement) microscopy. Additionally, DLS can also help understand solvation of tubulin, and thus explore the validity of the ‘slip-layer’ being present on microtubules and evaluate its response to different environments. DLS is thus a novel technique that straddles both the advantages of fluorescence microscopy and electron microscopy. We envisage its further use in quantification of kinetics of microtubules and other cytoskeletal polymers in the future.

5. Exploring the tunability of tubulin charge[4]

ABSTRACT

Exploiting the electrostatic behaviour of tubulin and microtubules within device-based applications is limited due to the lack of understanding of tubulin behavior as a function of solvent composition, especially DMSO, a key solvent used in such devices. This chapter displays the tunability of tubulin surface charge using DMSO for the first time. Increasing the DMSO volume fractions leads to the lowering of tubulin's negative surface charge, eventually causing it to become positive in solutions > 80 % DMSO. As determined by electrophoretic mobility measurements, this change in surface charge is directionally reversible i.e permitting control between –1.5 $cm^2 (V\ s)^{-1}$ and + 0.2 $cm^2 (V\ s)^{-1}$. When usually negative microtubules are exposed to these conditions, they form positively surface charged tubulin sheets and aggregates, as revealed by an electrophoretic transport assay. Fluorescence-based experiments also indicate that tubulin sheets and aggregates co-localize with G-C_3N_4 sheets while microtubule do not, further verifying the presence of a positive surface charge. This study illustrates that tubulin and its polymers, in addition to being mechanically robust, are also electrically tunable.

INTRODUCTION

Microtubule mechanical properties (Young's modulus ~1 GPa; persistence length 1-10 mm [35, 37, 252-253]) and ability to generate forces of up to 5 pN due to polymerization [254] are key features that enable intracellular roles, and have also led to utilization within engineered nano- and micro-electromechanical systems (NEMS/MEMS). In tandem with molecular motors, microtubules have been employed within high efficiency rectifiers, [44, 255] biosensors, [256-258]

[4] This chapter was published as a research article Kalra Aarat P., Patel Sahil D., Eakins Boden B., Riddell Saralyn, Kumar Pawan, Winter Philip, Preto Jordane, Carlson Kris W., Lewis John D., Rezania Vahid, Tuszynski Jack A., Shankar Karthik. "Revealing and attenuating the electrostatic properties of tubulin and its polymers" *Small* 2003560 (2020).

direction-specific sorters and transporters, [48, 53, 207, 259] force-meters, [54] as nanopatterning agents, [260-262] and even for parallel nanocomputing. [263] Interestingly, in addition to such mechanical roles, microtubule-based systems can also exploit the highly negative charge (47 e^-) that tubulin dimers exhibit at physiological pH values. [165, 264] This high negative charge leads to extensive counterionic condensation on the microtubule outer surface. [15, 17, 125] Experiments have validated computational predictions that the presence of microtubules increases solution capacitance under physiologically relevant ionic conditions. [13, 15] When exposed to a.c. electric fields (in the kHz regime), these condensed counterions are modelled to contribute to imaginary impedance of the system, leading to experimentally observable frequency-specific changes in solution conductance. [21, 81, 135] The high negative charge of tubulin also leads to a large protein dipole moment because ~ 40% of the total negative charge is accumulated on the filamentous C-termini 'tails' (Figure 5.1a), which contributes to the dipole moment of the dimer when a counter ionic double layer is formed around these charges. Depending on the tubulin isotype, the value of the dimer's dipole moment ranges between 1500 D and 3500 D. [265] Upon exposure to electrical nanosecond pulses, C-termini tails are modelled to undergo conformational changes that can attenuate microtubule assembly. [67] The electrical properties of tubulin enable unprecedented control over microtubule trajectories, allowing for directed spatial migration, [79-80, 87, 120] and full-circle electro-rotation [127-128] when subjected to d.c electric fields. Crucially, non-uniform electric fields can also sort microtubules in a mechanical stiffness-dependent manner. [62-63] While tunability of the mechanical properties of microtubules is well demonstrated, tunability of electrical properties can enable the launch of several possible applications within electrically driven tubulin-based devices.

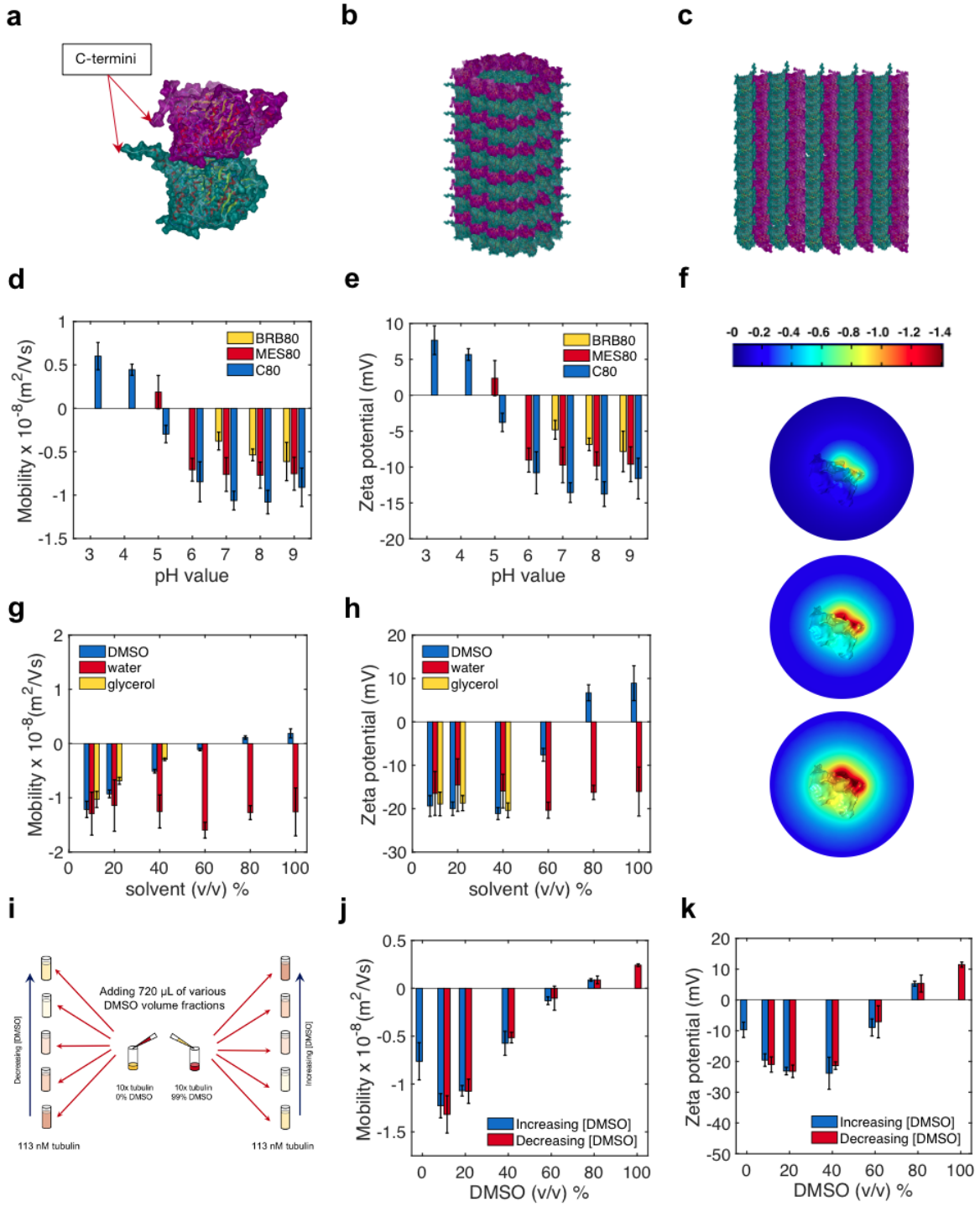

Figure 5.1. (a) The three-dimensional structure of the tubulin heterodimer, displaying the C-terminal tails. α and β subunits are shown in cyan and magenta respectively. (b) A schematic of the microtubule structure, composed of α, β tubulin dimers. (c) A schematic of α, β tubulin sheet structure. (d) The variation of mobility as a function of solution pH value. (e) The variation of zeta potential as a function of solution pH value. Mobility and zeta potential were measured using commercial equipment (Malvern Zetasizer; see Supporting Information). (f) A simulation of the electric potential around the tubulin dimer under varying ionic environments ranging from pH 5, to pH 7, and pH 9. Simulation was performed as described using parameters

extracted from Table E1 and section E1. (g) The variation of mobility as a function of solvent volume fraction. Volume fractions were measured in percent values, with the remainder consisting of MES80. (h) Graph displaying the variation of zeta potential as a function of solvent volume fraction. (i) The experimental procedure used to create increasing and decreasing DMSO volume fractions for probing directional reversibility. (j) Graph displaying the variation of mobility as a function of DMSO volume fraction and dilution direction. (k) Graph displaying the variation of zeta potential as a function of DMSO volume fraction and dilution direction. All measurements were performed at 25 °C.

RESULTS

Herein, we report tunability of tubulin surface charge through the addition of DMSO as a co-solvent into aqueous buffer. We measure tubulin electrophoretic mobility (henceforth referred to simply as mobility) and zeta potential (ZP), to show that dissolving tubulin in increasingly large DMSO volume fractions can eventually result in a change in sign of the net electric charge on tubulin. We find that surface charge on tubulin becomes positive at >80 % DMSO (v/v) solutions. Upon investigation of tubulin polymers in these solutions, we find that microtubules (which would otherwise be negatively surface charged in aqueous buffers at neutral pH values) open-up to form two-dimensional sheets and aggregates, also acquiring a net positive charge in the process. DMSO, which enhances tubulin polymerization [222] and oligomerization, [161] can also be used to mimic non-polar macromolecules such as lipids within the interior of the cell membrane. While the high mechanical strength of microtubules and their interesting electrical properties have allowed their utilization in several nanoscale devices, unlike several other bio-nanoparticles (such as Eumelanin, DNA and cellulose), [1, 3, 266] their utilization within OLEDs (organic light emitting diodes) and OPVs (organic photovoltaics) has not been possible due to the prevalence of DMSO as a solvent within these technologies, [267] Here, we present the first experimental study exploring the electrical properties of tubulin within DMSO and DMSO-majority solutions. In so doing, we demonstrate the utility of tubulin and its polymers within electrically based devices. Our work shows that tubulin polymers, in addition to being mechanically robust, are also electro-morphologically tunable by the addition of DMSO.

To establish the mobility and ZP of tubulin in aqueous solutions, we used the two microtubule stabilization buffers BRB80 and MES80, in addition to a citrate-KOH buffer (C80, which uses citric acid as a buffering agent). As expected, we measured negative values for mobility and ZP of tubulin at neutral pH (Figure 1d, e). Of the three buffers we tested, we found the mobility

and ZP of tubulin to be highest in BRB80 (mobility = $-0.37 \pm 0.10 \times 10^{-6}$ cm/Vs, ZP = -4.81 ± 1.31 mV), and lowest in C80 (mobility = $-1.06 \pm 0.10 \times 10^{-6}$ cm/Vs, ZP = -13.55 ± 1.37 mV) at neutral pH. Tubulin exhibited a neutral surface charge as the pH was lowered below 7, eventually becoming positively charged at pH <5 (Figure 5.1 d, e; Figure E1). To investigate the electrical environment around the tubulin dimer as a function of pH value, we first predicted the structure of tubulin as a function of its protonation state, subsequently using COMSOL Multiphysics 5.5 (COMSOL Inc, Burlington, MA) to simulate the static electric potential of tubulin (Figure 1f; Appendix E (Materials and Methods)). Upon close inspection of the ZP and mobility of tubulin, we found that the isoelectric point (pI) of tubulin was slightly above 5 in MES80 and was approximately 4.5 in C80 buffer (Figure E1). The insolubility of PIPES (buffering agent in BRB80) at low pH values prevented its use for tubulin pI determination in BRB80. Differences in mobility and ZP are explained by tubulin conformational changes due to different buffering agents, causing it to have different net surface charges in different environments. For example, tubulin dimers are possibly non-covalently cross-linked by sulfonate groups, thus PIPES (containing two sulfonate groups) is hypothesized to polymerize tubulin to a greater extent compared to MES80 (MES contains one sulfonate group). [268]

To determine how DMSO would alter tubulin's net surface charge, we dissolved tubulin in various DMSO volume fractions. The mobility and ZP became less negative as the volume fraction of DMSO was increased, finally attaining a positive value (mobility at 99.7 % DMSO v/v = 0.18 ± 0.08 cm^2 (V s)$^{-1}$, ZP = 8.91 ± 4.01 mV) at >80% DMSO (Figure 5.1g, h). The effective charge of tubulin in this environment was calculated to be $+1.14 \pm 0.51$ *e*, as opposed to -4.14 ± 0.51 *e* in 0 % DMSO solution (calculation details displayed in Appendix E; Materials and Methods). This result indicates that tubulin's net surface charge could be attenuated by simply adding different volume fractions of DMSO to solution. The ability of DMSO to tune surface charge is explained by its aprotic nature and low relative permittivity, which acts to increase the pKa value of individual residues. This result has been predicted for various chemical species [269-270] and has been experimentally validated for proteins such as BSA (bovine serum albumin) and lysozyme. [271] To validate these results for tubulin, we also measured the ZP and mobility of tubulin under increasing water (i.e diluting the solution) and glycerol volume fractions as controls. Glycerol is commonly used in polymerization 'cushion' buffers due to its stabilizing influence on microtubules. [219] Lowering ionic strength (altered here by increasing water volume fraction) alters microtubule growth rates, [189, 198] increases

microtubule mobility [87] and alters their mechanical properties. Glycerol is also used as a crowding agent to study the effect of macromolecules that occupy up to 40 % of the intracellular volume fraction. [272] The presence of crowding agents *in vitro* alters the structure and dynamics of proteins, [273-276] for example, significantly increasing microtubule growth and nucleation rates. [219] In the presence of 40 % glycerol, the mobility and ZP of tubulin were found to be $-0.29 \pm 0.02 \times 10^{-6}$ cm^2 (V s)$^{-1}$ and 20.39 ± 1.69 mV, respectively. Both glycerol and DMSO have similar relative electrical permittivity values ($\varepsilon_{dmso} = 46.7$, $\varepsilon_{glycerol} = 42.5$), which may indicate similar influence on the mobility and ZP of tubulin. However, as the glycerol volume fraction was increased, the tubulin ZP remained unchanged with increasing glycerol volume fractions (Figure 1h). Estimation of electrical properties in >50 % glycerol solutions was unreliable, possibly due to the high viscosity of the solutions, limiting the ability to compare the electrical effect of glycerol and DMSO addition to tubulin solutions. As solution viscosity increased due glycerol addition, tubulin mobility lowered as expected (Figure 1g). Interestingly, the ionic strength (altered by increasing water volume fraction) was found not to influence tubulin ZP or mobility significantly (as demonstrated by a two-tailed t-test p-value of 0.851 on comparing 0 % and 99% water volume fraction).

To investigate if the tunability of tubulin surface by DMSO was directionally reversible, a 'mother liquor' solution composed of 1.13 µM tubulin dissolved in 99.9 % DMSO was prepared (Figure 5.1i). The addition of varying water volume fractions to 1 µL of this solution induced a reversal to negative mobility and ZP values (Figure 5.1 j, 5.1 k). When the opposite experiment was conducted, i.e. by the dilution of an aqueous mother liquor (containing negatively surface charged tubulin) using higher DMSO volume fractions, tubulin acquired a net positive surface charge. This experiment indicated that positively surface charged tubulin could be induced to have a negative surface charge, and vice versa. The tunability of tubulin remains unchanged irrespective of its solvent history, indicating the utility of tubulin as a DMSO sensor.

We next investigated the biochemical fate of microtubules (which have a negative surface charge), when exposed to >80 % DMSO solutions. To address this question, polymerization of 1:15 rhodamine-labelled tubulin into microtubules was performed in BRB80 (Appendix E; Materials and Methods). Microtubules were subsequently stabilized using either BRB80T (BRB80 supplemented with 200 µM paclitaxel) or using >80 % DMSOT (DMSO supplemented with 200 µM paclitaxel). When solutions stabilized in BRB80T were imaged

using epi-fluorescence microscopy, long filamentous microtubules were observed, as expected (Figure 5.2 a). However, when solutions stabilized in >80 % DMSOT were imaged, a mixture of two-dimensional tubulin sheets and tubulin aggregates were observed (Figure 5.2 b). To investigate their surface charge, two-dimensional sheets of fluorine-doped graphitic carbon nitride (g-C_3N_4; a negatively surface charged fluorophore; zeta potential = −26.8 mV) [277] were introduced into tubulin polymer solutions. Interestingly, the g-C_3N_4 sheets co-localized to tubulin sheets in >80 % DMSOT solutions, validating the presence of a positive surface charge on the tubulin (Figure 5.2 e). However, microtubules in 50 % DMSOT (Figure 5.2d) and in BRB80T (Figure 5.2 c), being negatively surface charged, were not found to co-localize with g-C_3N_4 sheets. Due to similar dimensions and the relative ease of chemically conjugating tubulin, devices where carbon nanotubes (CNTs) and MTs work synergistically have also been fabricated. [52, 55] Correspondingly, this work envisages the utility of conjugating g-C_3N_4 to tubulin by co-localization, allowing the regulation of the electrical properties of g-C_3N_4 through doping with various chemical agents (including heteroatom precursors such as NH_4F, thiourea, 4-(diphenylphosphino) benzoic acid (4-DPPBA) and phosphoric acid) and it would be possible to regulate the electrical properties of tubulin through C-terminal cleavage or pH changes, and their furthermore their relative proximity to each other would be controlled through the addition of DMSOT. These findings appear to illustrate that when microtubules are exposed to >80% DMSOT, positively surface charged two-dimensional polymers are formed (Figure 5.2f).

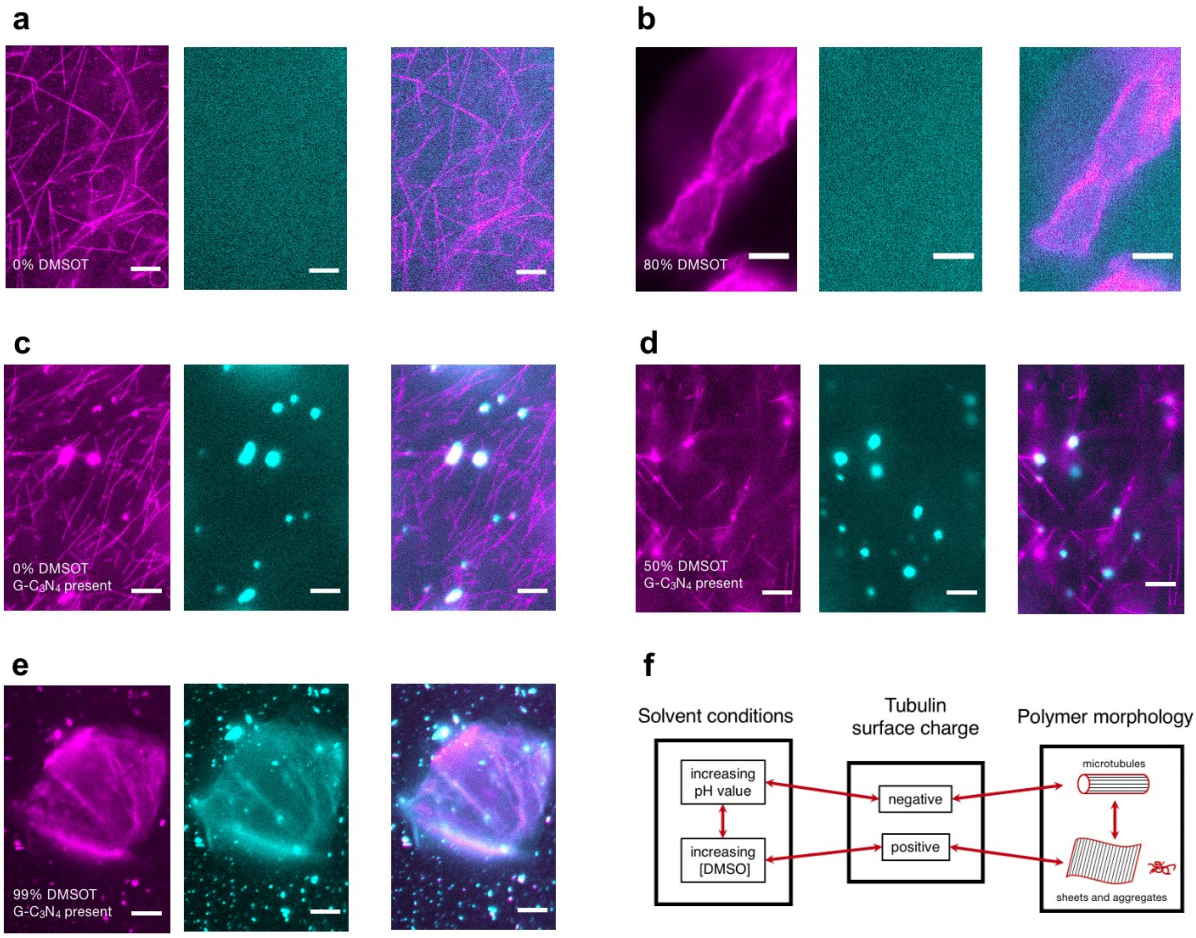

Figure 5.2. (a) Microtubules (450 nM tubulin) stabilized with BRB80T (0 % DMSOT), imaged with an epi-fluorescence microscope using two channels: Magenta (excitation and emission wavelengths of 535 nm and 610 nm) and Teal (excitation and emission wavelengths of 350 nm and 460 nm). (b) Microtubules (450 nM tubulin) stabilized with 80 % DMSOT. (c) Microtubules (450 nM tubulin) stabilized with BRB80T (0% DMSOT), with two dimensional sheets of G-C_3N_4 present. (d) Microtubules (450 nM tubulin) stabilized with 50 % DMSOT, with two dimensional sheets of G-C_3N_4 present. (e) Microtubules (450 nM tubulin) stabilized with 99 % DMSOT, with two dimensional sheets of G-C_3N_4 present. (f) Schematic displaying the interplay between solvent conditions, tubulin surface charge and tubulin polymer morphology. All scale bars represent 10 μm.

To further evaluate the sign of the tubulin polymer surface charge in >80 % DMSOT solutions, an electrophoretic migration assay was performed. Two groups of tubulin polymers, one in BRB80T and the other in >80% DMSOT, were separately exposed to d.c. electric fields between 6 and 60 V cm^{-1} intensity using platinum contacts (Figure 5.3 a, 5.3 b). Polymer migration *en masse* towards a specific contact was monitored using time-lapse epifluorescence

microscopy. As expected, microtubules in BRB80T were found to migrate toward the positively charged contact (Figure 5.3 e, 5.3 f). However, tubulin polymers in >80 % DMSOT were found to behave in the opposite manner, migrating toward the negatively charged contact, validating their net positive surface charge. The finding was validated further when the electric field direction was reversed, and tubulin polymers were transported in the opposite direction (Figure 5.3 c, 5.3 d).

CONCLUSIONS

Taken together, these results illustrate the interplay between the electrostatic properties of tubulin (negative or positive surface charge) and its polymeric state (microtubules or sheets). We started out by quantifying the mobility and ZP of tubulin in physiological conditions and determining its isoelectric point in aqueous buffers used for microtubule polymerization. We subsequently used a variety of assays, including electrophoretic directional transport, to confirm a 'flip' in the sign of tubulin net surface charge in >80 % DMSO solutions. The effective charge of tubulin was tuned from $-4.14\ e$ in 0 % DMSO to $+1.14\ e$ in 99.7 % DMSO solutions. To our knowledge, this work is the first demonstration of the electrical tunability of tubulin using DMSO. By experimentally demonstrating tunability of tubulin electrostatics in DMSO, we bring this protein one step closer to utilization within the flexible optoelectronics industry, where DMSO is used as a solvent. Our experiments also reveal that alteration of the tubulin surface charge by DMSO is directionally reversible and consistent with experimental and computational work showing that DMSO acts to increase pKa values of chemical species.[269-270] We further show that when microtubules composed of negatively charged tubulin are introduced in such an environment, large sheets and amorphous aggregates are formed.

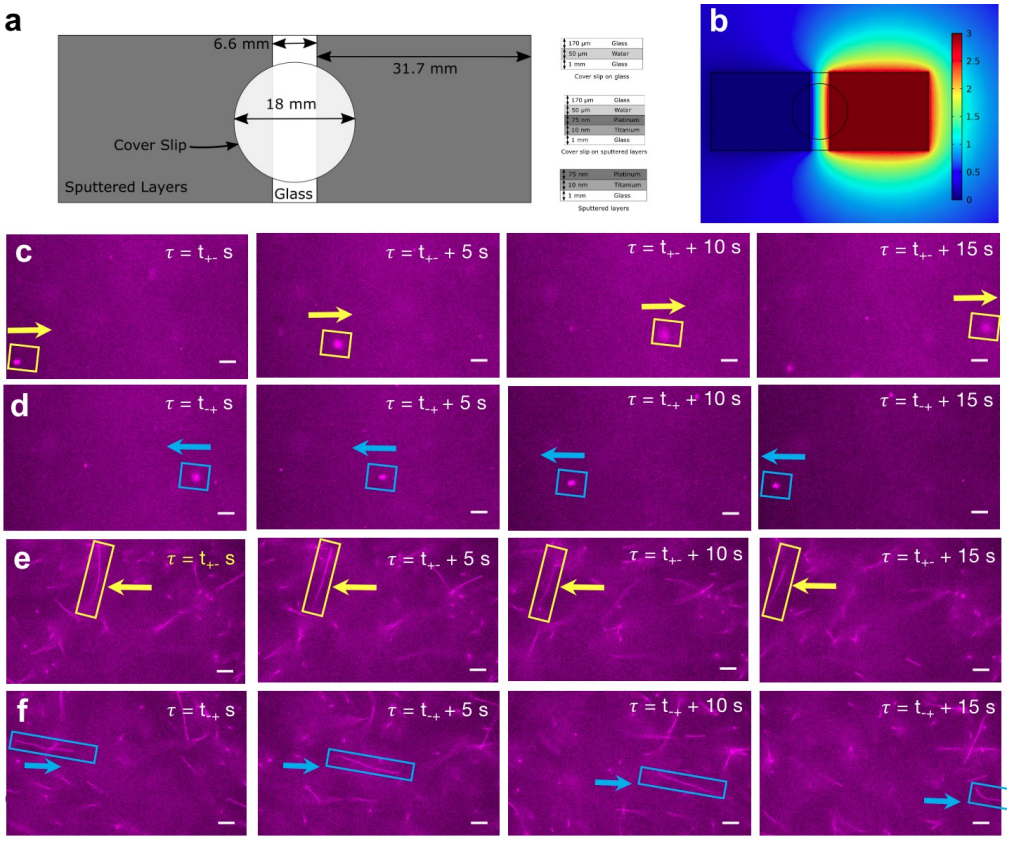

Figure 5.3. (a) A schematic representation of the apparatus used for the electrophoretic transport assay. (b) The electric potential values in the plane 40 nm above the glass slide. The right side of the image displays a Pt contact pad held at 3 V (resulting in an electric field intensity of 6 $V.cm^{-1}$ between the contacts), while the left side displays a grounded Pt pad. (c) An exemplary trajectory of a tubulin sheets (highlighted using a yellow box) in 98 % DMSOT, when exposed to a 24 $V.cm^{-1}$ d.c. electric field in the left to right direction. (d) An exemplary trajectory of a tubulin sheets (highlighted using a blue box) in 98 % DMSOT, when exposed to a 24 $V.cm^{-1}$ d.c. electric field in the right to left direction. (e) An exemplary trajectory of a microtubule when exposed to a 6 $V.cm^{-1}$ d.c. electric field is in the left to right direction. The arrow indicates the direction of microtubule transport. (f) An exemplary trajectory of a microtubule (highlighted using a blue box) when exposed to a 6 $V.cm^{-1}$ d.c electric field in the right to left direction. The yellow boxes represent cases where the electric field is in the left to right direction, while the blue boxes represent opposite cases All scale bars represent 10 μm.

In the presence of DMSO, in addition to becoming positively charged, tubulin also undergoes conformational changes due to solvent effects, that cause it to stabilize sheets instead of

microtubules. [220, 222, 278] Sheets have a lower inter-protofilament curvature than microtubules, allowing for unpolymerized tubulin and neighboring sheets to form lateral contacts, forming larger sheets. [222, 233] This effect is also thought to take place when the solution pH is lowered. [279] The 'sheet stabilizing' action of DMSO-majority solutions may be a combination of (a) the lower ionic strength of DMSO-majority solutions and (b) the small positive charge on tubulin in these conditions, which leads to lower shielding between tubulin dimers (which would otherwise be large due to high electrostatic charge) allowing adjacent sheets to potentially laterally attach. DMSO has also previously been shown to enhance tubulin polymerization due to macromolecular crowding effects. [222] While this aspect has not been explored in the present paper, this could be an interesting topic for future work.

Thus, we display the ability of tubulin surface charge to regulate tubulin polymer state by responding to changes in its chemical environment. In the future, evaluating interactions between microtubules and molecular motors in this solvent would be of great benefit in harnessing the electro-mechanical promise of these biologically ubiquitous nanowires. Attenuating the electrostatic properties of tubulin and microtubules will alter the interactions of motors with these substrates. The integration of the microtubule-motor complex in DMSO-water mixtures would provide a fruitful method for tuning tubulin electrical properties, while simultaneously modulating its polymeric state. Our work is the first critical step in this direction.

6. Conclusions and future outlook

Using impedance spectroscopy, my work has shown that while microtubules increase solution capacitance, unpolymerized tubulin at the same concentrations do not. This result arises from the highly negative charge and cylindrical morphology of a microtubule and indicates their potential role as intracellular charge storage devices. Given that microtubules have interesting electrical properties, we wanted to explore the possibility of tubulin and microtubule based electrical devices. Exploiting the electrostatic behaviour of tubulin and microtubules within device-based applications is limited due to the lack of understanding of tubulin behavior as a function of solvent composition, especially DMSO, a key solvent used in such devices. To characterize the response of tubulin to the presence of DMSO, we used Dynamic Light Scattering and epifluorescence microscopy to show that the hydrodynamic diameter of tubulin increases in the presence of increasingly large volume fractions of DMSO to form oligomers. As the concentration of DMSO is increased to > 20 % DMSO, the net negative surface charge of tubulin reduces, eventually acquiring a positive value at > 80 % DMSO.

In the future, experiments should be devoted to determining which ions condense around a microtubule to the largest extent, and which of these are transported along its length. The role of the C-termini in charge storage and transport must also be gleaned from further experimentation. The feasibility of C-termini coupling to one another in response to electromechanical stimuli such as external electric fields must be investigated.

Additionally, the precise role of the lumen in charge transport must be evaluated. Thus far, while the role of the lumen in charge transport has been modelled, experimental validation of charge transport through it remains to be conducted. The ratio of ionic transport that takes place outside a microtubule along its length, and inside the lumen must also be determined. For this, the extend of ‘crossover’ between these two modes of charge transport, and ‘leakage’ into the

surrounding solution should also be quantified. Quantification of such parameters will not only lead to the effective utilization of microtubules within nanodevices, but will also improve our understanding of the cell.

It is also important to examine how tubulin polymerization alters the electrical properties of surrounding solution, and if the change in local ionic concentration due to microtubule polymerization is relevant within the cell. While it is now clear that the interactions of microtubules with MAPs and tubulin-interacting drugs are altered by changing solution parameters such as viscosity and ionic strength, a thorough exploration of how they are influenced by external (a.c. and d.c.) electric fields needs to be performed. Due to its intracellular importance, the attenuation of the kinesin-MT interaction upon electric field exposure must be specifically explored. This will ensure that the interplay of MAPs and drug binding with biochemical, electrical and mechanical parameters is well documented. Similarly, the influence of the presence of actin filaments on MTs and their electrical properties will also be useful in understanding the bioelectrical underpinnings of the cytoskeleton. This will help create a clearer picture of charge storage and transport within the cell.

A crucial question revolves around how different electric fields intensities and waveforms influence tubulin polymerization into MTs and overall MT stability. Careful examination, using techniques such as turbidimetry and fluorescence microscopy, must hence be performed to understand how the biochemical and biomechanical properties of microtubules respond to electrical stimulus. Such work will, in addition to being useful from a fundamental science standpoint, also be beneficial for medical applications. Studies on MAPs, electric fields and microtubules will shed light on whether TTFields target the electrical properties of tubulin and MTs. Novel medical treatments based on results from such studies can also be envisaged. Optimization of already-existing treatment modalities can also be performed from such studies.

For the utilization of MTs within electrical devices, further characterization within solvents used for such devices must be performed. While this thesis addresses characterization within DMSO, further work on the response of tubulin and MTs to DMF must also be carried out. Characterization of microtubules in the solid-state, to shed light on their ability to act as electronic conductors, will also require future assessment. Once a complete characterization in non-aqueous solvents, and the solid state is complete, studies on the utilization of MTs and tubulin in electrical devices such as OPVs and OLEDs can be performed.

Appendix A: Figure permissions

Documents regarding permissions to reuse figures are available upon request.

Appendix B: Supplementary materials for Chapter 3

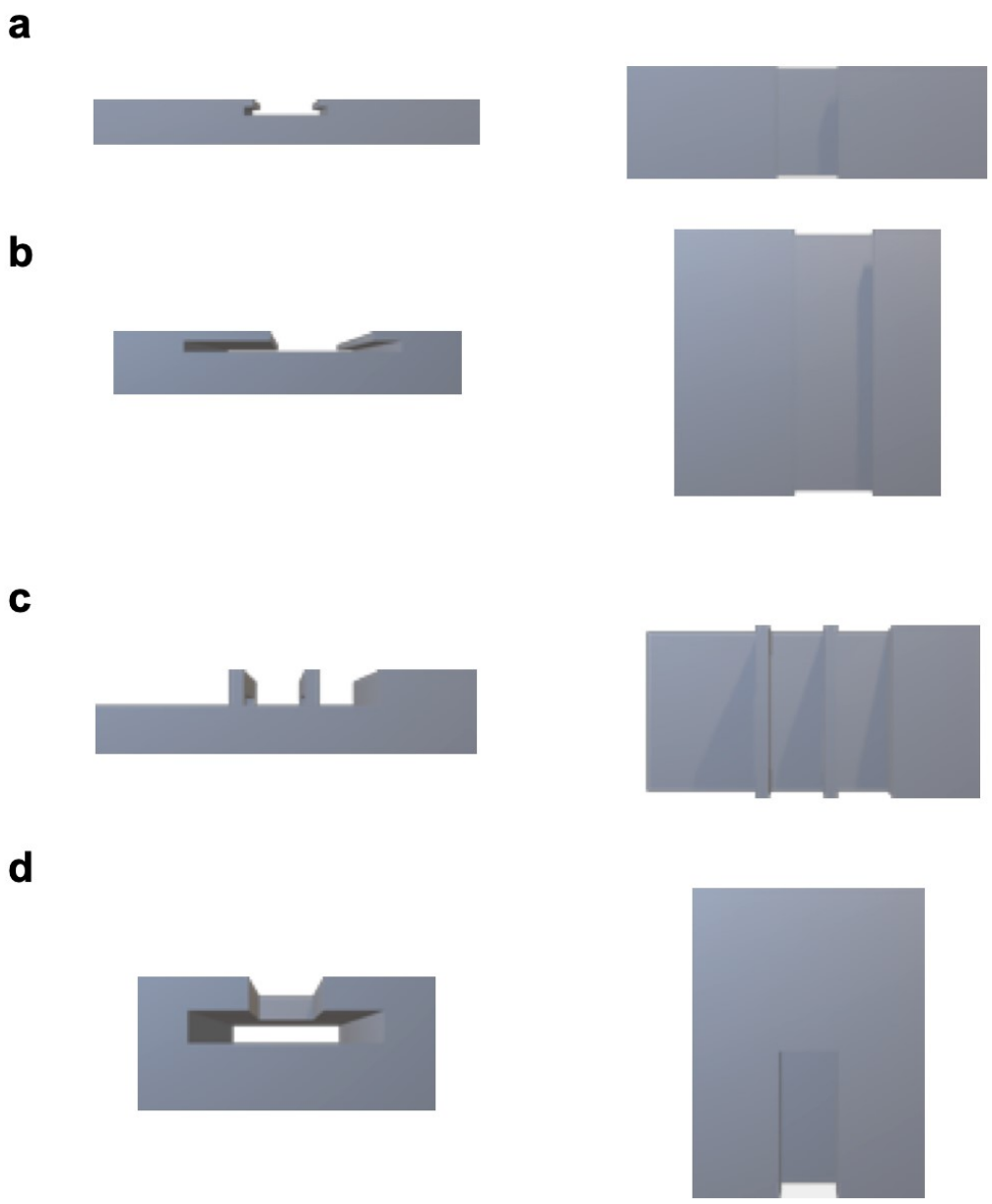

Figure B1. 3D printed holders used to fabricate and align the parallel-plate contact device. (a) Top view (left) and (b) side view (right) of holder for the parallel plate device used to perform impedance measurements. (c) Top view (left) and side view (right) of slider used to position the double-sided tape exactly to fabricate the device. (d) Top view (left) and side view (right) of the holder used to position the upper contact precisely on the lower contact.

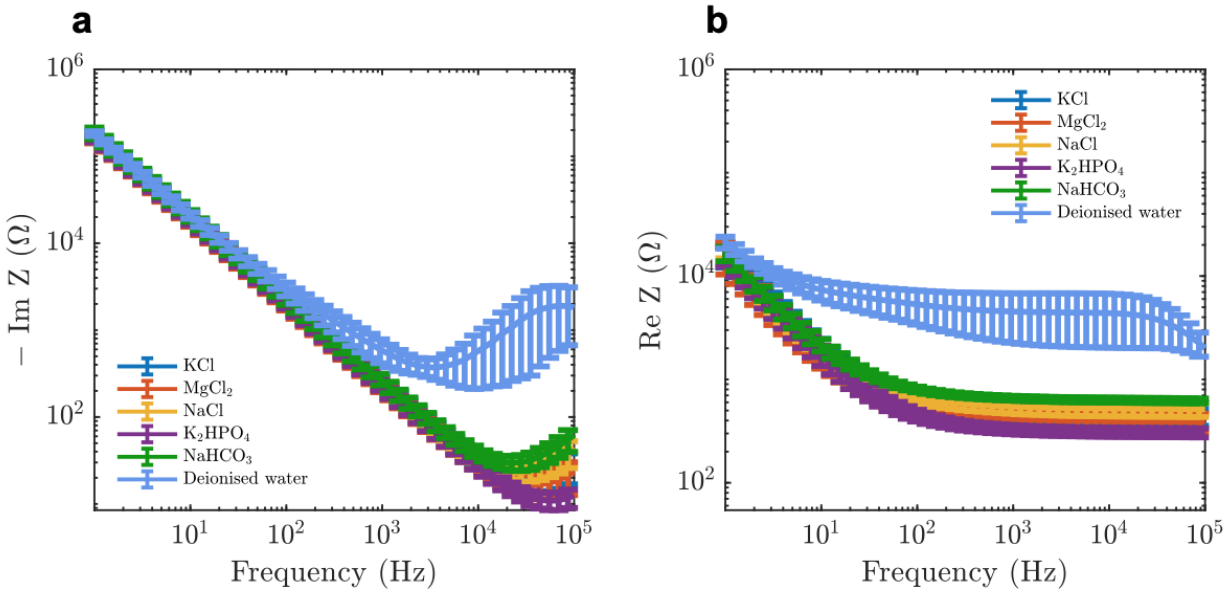

Figure B2. Validation of parallel-plate contact device using 0.5 mM electrolytic solutions (a) Imaginary component of impedance for electrolytic solutions at 0.5 mM and de-ionized water. (b) Real component of impedance for electrolytic solutions at 100 mM and de-ionized water. Data displays average values collected between 15 and 21 times. Error bars represent standard deviation.

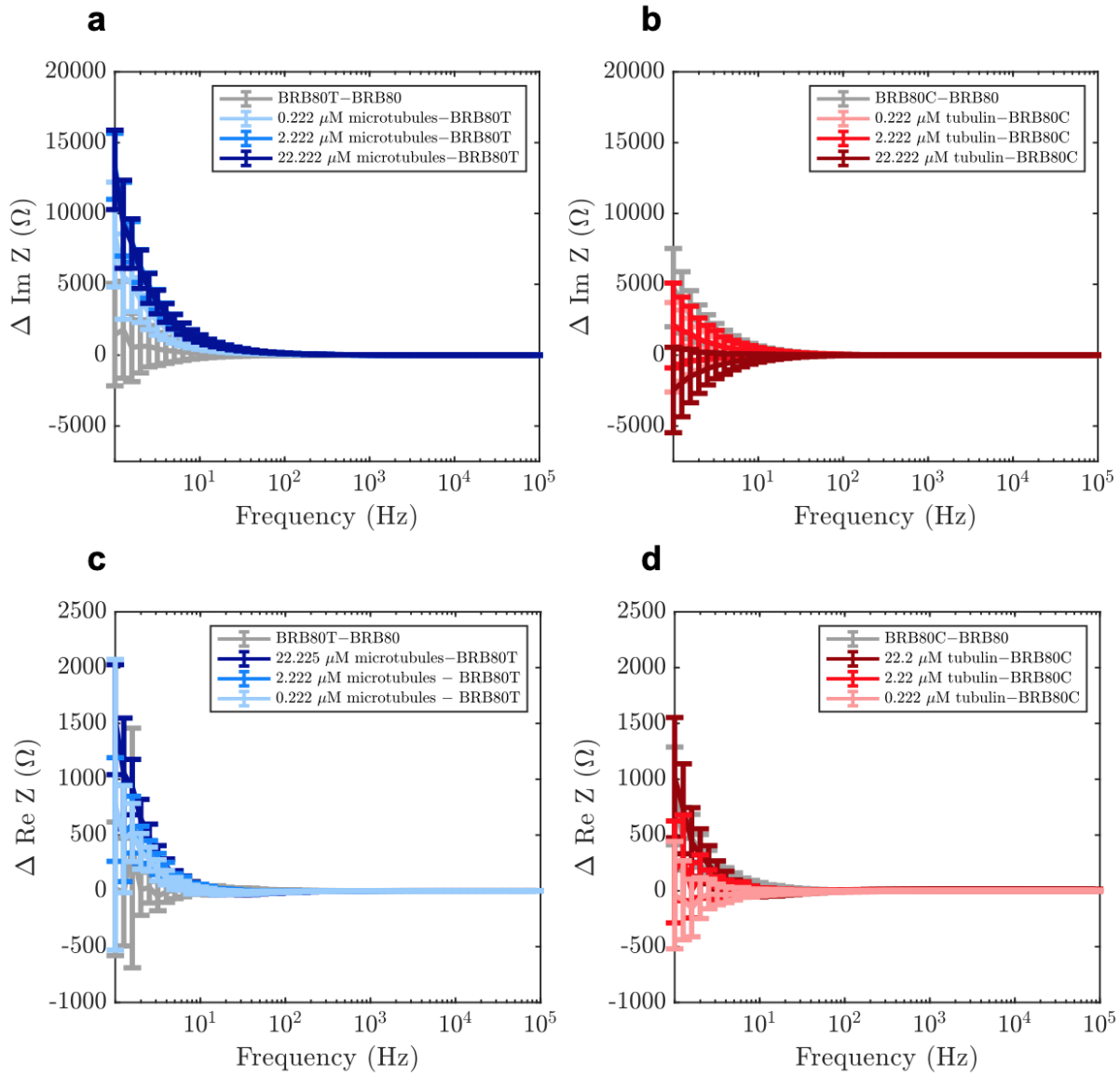

Figure B3. Example of microtubule and tubulin subtraction with backgrounds, to display typical impedance.

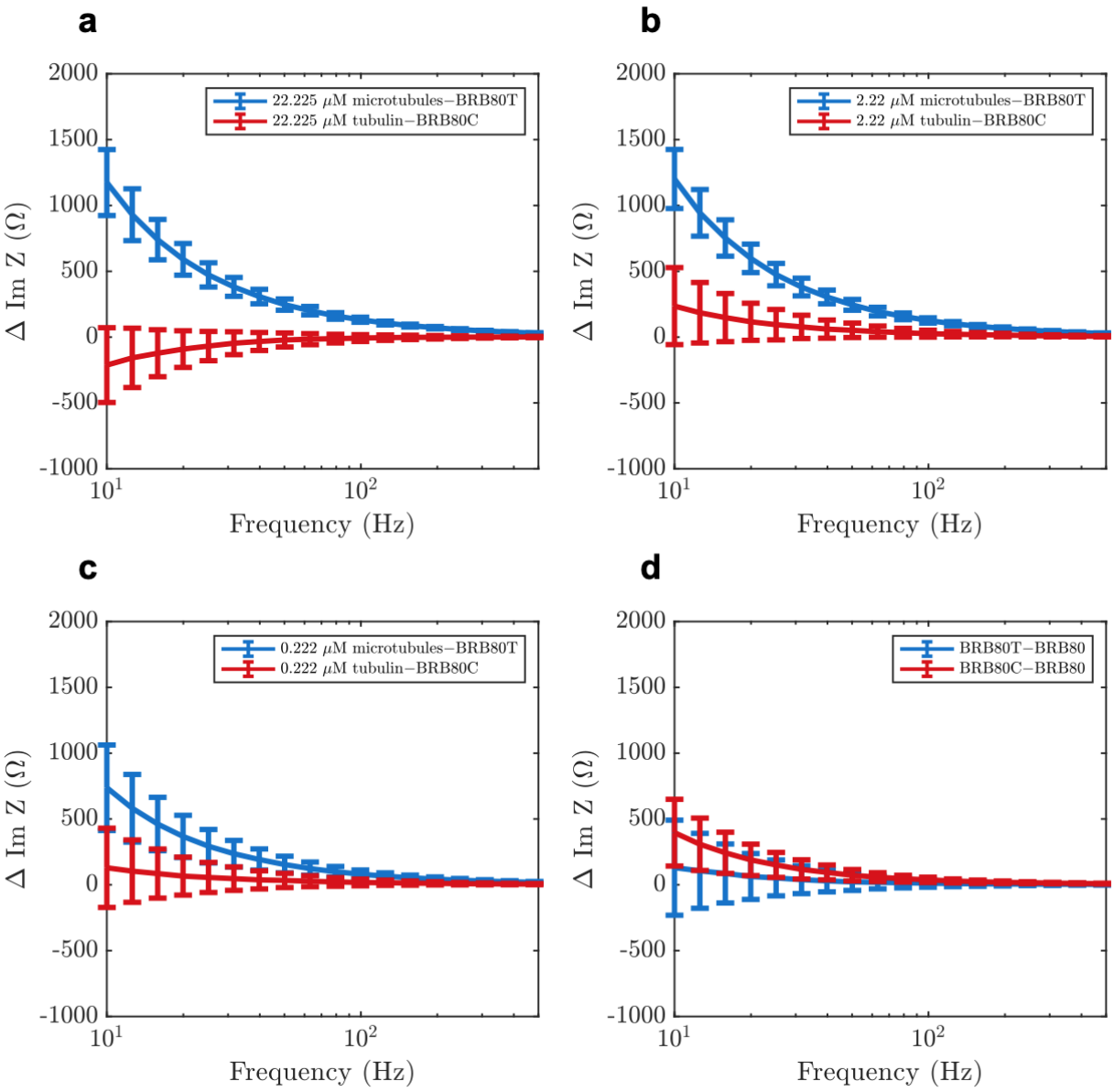

Figure B4. No 'reversal' in the resistive behavior of microtubules is observed between 10 and 100 Hz. Graphs showing differences in the real component of impedance as a function of decreasing input AC frequency at total tubulin concentrations of (a) 22.225 μM, (b) 2.222 μM, (c) 0.222 μM, (d) comparison of the effect of paclitaxel and colchicine on impedance.

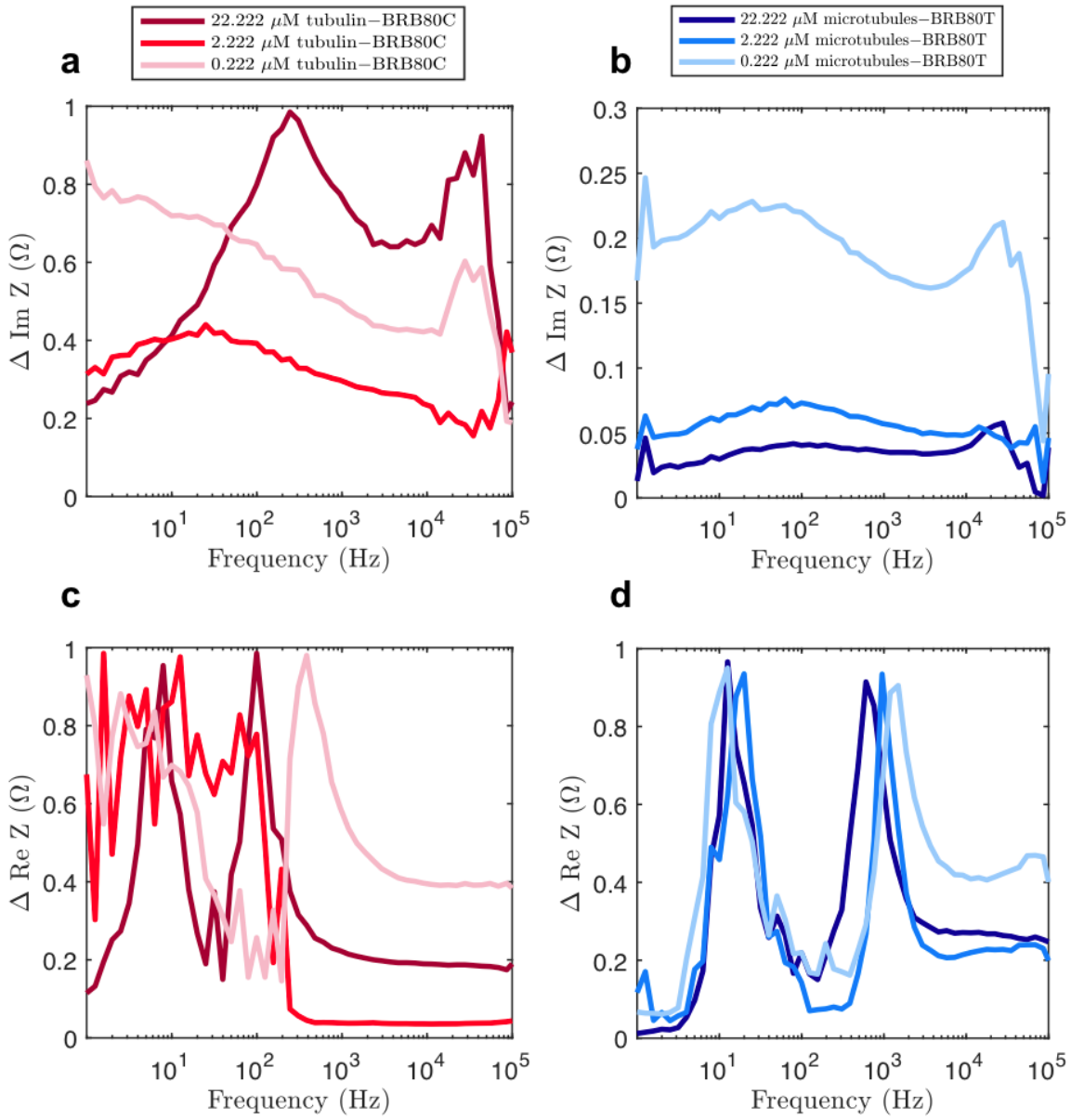

Figure B5. One-sample t-tests were performed using to determine if the impedance difference values were significantly above zero. This was carried out using the ttest function within MATLAB. Graphs showing the variation of obtained p-values for the imaginary components of impedance in (a) tubulin and (b) MT-containing solutions. Graphs showing the variation of obtained p-values for the real components of impedance in (a) tubulin and (b) MT-containing solutions.

Appendix C: Supplementary materials for Chapter 4

DMSO % (v/v)	Parameter y_0 (nm)		Parameter x_c (nm)		Parameter A (nm^2)		Parameter w (nm)		Reduced Chi-Sqr	Adj. R-Square
	Value	SE	Value	SE	Value	SE	Value	SE		
Number distribution										
0	0.440	0.277	7.038	0.0703 1	68.099	3.619	3.306	0.176	1.425	0.957
5	0.049	0.267	9.459	0.0684	104.167	4.401	3.922	0.170	1.432	0.971
10	0.022	0.266	10.784	0.064	120.210	4.701	3.883	0.157	1.518	0.975
15	0.042	0.260	11.641	0.069	129.220	4.991	4.220	0.169	1.449	0.976
20	0.018	0.261	13.15	0.077	148.179	5.663	4.773	0.190	1.467	0.976
Volume distribution										
0	0.208	0.278	8.178	0.094	81.773	4.525	4.656	0.246	1.165	0.957
5	-0.003	0.271	10.457	0.091	114.040	5.276	4.965	0.229	1.349	0.967
10	-0.025	0.239	11.536	0.072	126.503	4.767	4.608	0.178	1.175	0.977
15	-0.001	0.248	12.436	0.083	134.199	5.346	5.031	0.206	1.25	0.974
20	-0.033	0.236	14.036	0.086	154.134	5.691	5.611	0.213	1.139	0.977
Intensity distribution										
0	0.109	0.116	10.527	0.194	29.376	2.520	6.593	0.524	0.170	0.912
5	-0.025	0.053	12.105	0.091	31.476	1.223	6.010	0.230	0.049	0.977
10	-0.016	0.031	12.433	0.064	21.009	0.666	4.847	0.159	0.020	0.983
15	-0.020	0.049	13.856	0.089	31.611	1.189	5.772	0.222	0.048	0.977
20	-0.025	0.045	15.113	0.077	37.259	1.173	5.872	0.190	0.043	0.983

Table C1. A schematic displaying the variation of all Gaussian fit parameters for equation (1), with Standard Errors (SE) with increasing DMSO concentration.

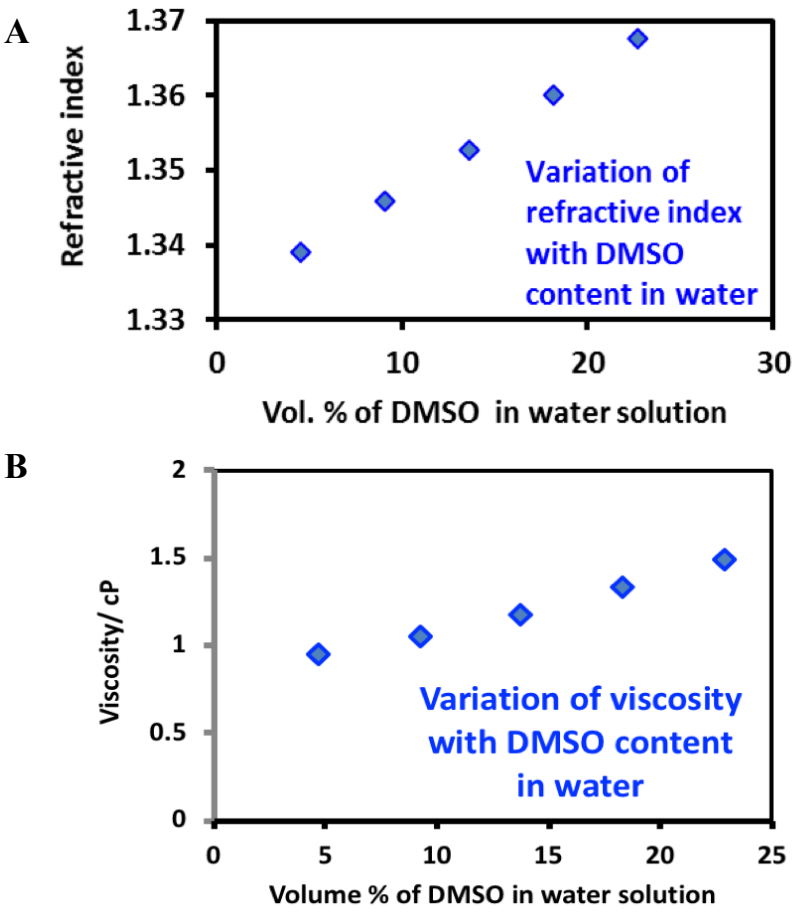

Fig. C1 (A) Variation of viscosity and (B) refractive index with increasing DMSO volume fractions in water.

Appendix D: Supplementary materials for Chapter 5

MATERIALS AND METHODS

S1. Simulation of electric field distribution around tubulin

A structure of a human tubulin dimer was created by homology modeling. The template structure used was 1JFF (PMID:11700061), which is bovine tubulin stabilized with a taxol ligand. 1JFF is considered to be a good structure for a tubulin dimer in a microtubule-like conformation. Sequences for human tubulin were obtained from UniProt, with Q71U36 used for alpha-tubulin and P07437 used for beta-tubulin. Sequence Q71U36 is the sequence for alpha-tubulin gene TUBA1A, which is an alpha-tubulin isotype that is highly expressed in the brain. Sequence P07437 is the sequence for beta-tubulin gene TUBB, which is a ubiquitously expressed beta-tubulin isotype. The Molecular Operating Environment (MOE; Chemical Computing Group, Montreal, Canada) was used to perform the homology modeling. The MOE loop modeler was used to generate conformations for a missing loop of the structure (alpha-tubulin positions 35-60), and for the C-terminals in both alpha-tubulin and beta-tubulin, which are highly flexible disordered regions (alpha-tubulin C-terminal was defined as positions 440-451, and beta-tubulin C-terminal was defined as positions 428-444). The best structure as determined by MOE's homology model scoring function was selected for further processing. Note that in the best scoring function structure the C-terminals had a conformation with electrostatic interactions with rest of the protein, as opposed to being extended in the solvent.

The tubulin structure thus obtained was protonated to various pH values using the 'protonate 3D' utility (solvent dielectric constant = 80 F m^{-1}; protein dielectric constant = 2 F m^{-1}; salt concentration = 0.2 M; viscosity = 0.89 × 10^{-3} Pa·s) in MOE (Molecular Operating Environment; Chemical Computing Group, Montréal, Quebéc, Canada). The final protonated structure was opened in VMD (Visual Molecular Dynamics, University of Illinois at Urbana-Champaign), and rendered to determine its surface using the 'Quicksurf' utility (grain-size = 1 unit). The resulting tubulin surface was saved and imported into SpaceClaim modeling software (SpaceClaim Corporation, Concord, Massachusetts) as a faceted body, where a 0.1 nm shrink-wrap is applied to produce an atomically correct solid body model. The tubulin surface is subsequently imported into COMSOL Multiphysics (COMSOL Inc, Burlington, MA), where the the protein is centered in a 20 nm radius spherical domain. to obtain a far-

field approximation for the electrical potential profile outside the protein surface, as a function of pH value.

pH	5	7	9
Overall charge on heterodimer	-25.95· e	-54.86· e	-75.00· e
Charge on α-tubulin C-terminal region	-7.38· e	-9.24· e	-9.31· e
Charge on β-tubulin C-terminal region	-9.37· e	-11.45· e	-11.54· e

Table D1. Charge distribution present on various regions of the tubulin heterodimer.

The region between the outer surface of the tubulin body and the and edge of the spherical domain is taken to be the computational domain. An electrical ground boundary condition is applied at the outer spherical shell, whereas the charge on the tubulin model is used as the second boundary condition.

In the calculated charge distribution of the tubulin protein, we do not account for the surface charge arising from the atomistic protein structure, instead we use a use a far-field approximation. The protein is considered as a union of two regions, the first being the main body, and the second being the 'tail-like' C-termini regions. The corresponding charges in these areas are shown in Table S1. This allows us to compute the surface charge densities on each respective region of the protein model.

$$\nabla^2 V = \frac{-\rho}{\epsilon_o} \qquad \text{(Equation D1)}$$

Finite element analysis is conducted in COMSOL to solve Poisson's equation (Equation 1) in the computational domain with the specified boundary conditions. Notably, the second boundary condition changes as a function of the model's surrounding chemical environment. This yields the static electric potential around the tubulin protein as shown in Figure 1f. To account for ionic screening on the electric potential as a function of distance, values of electric potential are corrected along the x-axis Debye-Hückel theory for ionic screening.

$$V_f(r) = V_i(r)e^{-r/\lambda_D} \qquad \text{(Equation D2)}$$

In Equation D2, the electric potential corrected with ionic screening is represented by $V_f(r)$, which is a function of radial distance from the protein. The un-screened electric potential is $V_i(r)$, and the Debye length is λ_D, given by eq. (4.3).

$$\lambda_D = \sqrt{\frac{\epsilon K_B T}{\sum_i n_i z_i^2}} \qquad \text{(Equation D3)}$$

In Equation D3, K_B is the Boltzmann constant, T is the temperature, ϵ represents the permittivity of the surrounding environment, n_i represents the ion species concentration, and z_i represents the charge of the corresponding ion. To match with experimental parameters, ϵ is taken to be $80\epsilon_o$, and T is taken to be 298.15 K. At every pH, Mg^{2+} and K^+ ions are present in concentrations of 1 mM and 160 mM respectively. H^+ ions are present at a concentration of 10^{-pH} M at each pH.

S2. Tubulin reconstitution, polymerization and stabilization

Lyophilized tubulin powder (Cytoskeleton Inc, Denver, CO, USA; T240) was reconstituted and with labelled tubulin (Cytoskeleton Inc, Denver, CO, USA; TL590M) as described previously [13, 161]. 45.45 µM tubulin was polymerized in a 37 °C water bath for 30 minutes in BRB80 pH 6.9 supplemented with 1 mM GTP (guanosine triphosphate; Cytoskeleton Inc, Denver, CO, USA; BST06). This step was followed by stabilization using 40 µM paclitaxel (Cytoskeleton Inc, Denver, CO, USA; TXD01; stock concentration 2mM).

S3. Determination of ZP and electrophoretic mobility using DLS

BRB80 buffers contained 80 mM PIPES, 2 mM $MgCl_2$, 0.5 mM EGTA. All MES80 buffers contained 80 mM MES, 2 mM $MgCl_2$, 0.5 mM EGTA. All C80 buffers contained 80 mM Citric acid, 2 mM $MgCl_2$, 0.5 mM EGTA. Milli-Q water was used for all experiments. The pH value of solutions was adjusted using KOH or HCl. All mobility and ZP measurements were performed using a Malvern Zetasizer Nano ZS (Malvern Instruments, Malvern, United Kingdom). Measurements in various aqueous media was preformed using folded capillary Zeta cells (DTS1070; Malvern Instruments, Malvern, United Kingdom). The Smoluchowski approximation for a monomodal distribution of particle ZP was used to perform experiments.

Tubulin (stock concentration 45.45 μM; reconstitution described above) was diluted in buffer (MES80, BRB80 or C80) to a final concentration of 113.6 nM for all experiments.
For measurements in increasing volume fractions of DMSO, glycerol and water, the ZEN1002 cell (Malvern Instruments, Malvern, United Kingdom) was used. The remaining volume fraction was composed of MES80 buffer. The dynamic viscosity, refractive index and relative permittivity used were adapted from previously published sources [280-282] and are displayed in Table S2. All measurements were conducted at 25 °C.

Solution	DMSO or Glycerol (w/w %)	Dynamic viscosity (cP)	Refractive index (n)	Relative permittivity (ε_r)
DMSO				
5 % DMSO	5.5	0.97	1.3397	78.4
10 % DMSO	11	1.084	1.3472	76.7
15 % DMSO	16.5	1.228	1.3459	75.1
20 % DMSO	22	1.404	1.3631	73.4
40 % DMSO	44	2.452	1.3977	66.7
60 % DMSO	66	3.658	1.4325	60.1
80 % DMSO	88	2.864	1.4625	53.4
99 % DMSO	108.9	1.99	1.4783	46.7
Glycerol				
5% Glycerol	1.22	1.22	1.347	75.05
10% Glycerol	1.73	1.73	1.363	71.74
20 % Glycerol	2.57	2.57	1.377	68.52
30 % Glycerol	4.05	4.05	1.391	65.33
40% Glycerol	6.86	6.86	1.406	61.68
50% Glycerol	12.76	12.76	1.420	57.62

Table D2. Table displaying the values of dynamic viscosity, refractive index and relative permittivity input for measuring the mobility of various tubulin solutions.

To investigate if negatively charged tubulin could acquire a positive charge upon the addition of increasingly large volume fractions of DMSO, solutions containing varying volume

fractions of DMSO to 80 µL of '10 x tubulin' (13.6 µM protein concentration) in MES80 pH 7 solution were added. The volumes for each mixture are shown in table S3.

	DMSO	MES buffer pH 7	MES80 solution 10x tubulin
90 % DMSO	720 µL	0 µL	80 µL
80 % DMSO	640 µL	80 µL	80 µL
60 % DMSO	480 µL	240 µL	80 µL
40% DMSO	320 µL	400 µL	80 µL
20 % DMSO	160 µL	560 µL	80 µL
10 % DMSO	80 µL	640 µL	80 µL

Table D3. Volumes of solutions used for to investigate if negatively surface charged tubulin may acquire a positive charge using varying volume fractions of DMSO. To investigate if positively charged tubulin can acquire a negative surface charge, similar experiments were performed using volumes displayed in Table S4. Importantly, the 10x tubulin solution was prepared in 99 % DMSO as a solvent. For experimental data analysis on mobility and ZP presented in this work, each experiment was performed in three sets of three experiments. Analysis was performed after combining all datapoints as one long experiment.

	DMSO	MES buffer pH 7	99 % DMSO solution 10x tubulin
99 % DMSO	720 µL	0 µL	80 µL
80 % DMSO	560 µL	160 µL	80 µL
60 % DMSO	400 µL	320 µL	80 µL
40% DMSO	240 µL	480 µL	80 µL
20 % DMSO	80 µL	640 µL	80 µL
10 % DMSO	0 µL	720 µL	80 µL

Table D4. Volumes of solutions used for to investigate if positively surface charged tubulin may acquire a negative charge using varying volume fractions of DMSO.

S4. Electrophoretic transport assay and simulation of electric field

For the electrophoretic transport assay, paclitaxel supplemented DMSO (DMSOT) was prepared by adding 5 µL of paclitaxel stock (2 mM) to 45 µL of DMSO, resulting in a final solution containing 200 µM paclitaxel. Similarly, BRB80 containing paclitaxel solutions (BRB80T) were prepared by adding 5 µL of paclitaxel stock to 45 µL of BRB80. To prepare a solution of microtubules (final concentration 450 µM tubulin), 49.5 µL of BRB80T was added to 0.5 µL of polymerized tubulin stock. To prepare microtubules (final concentration 4.5 µM tubulin) in 99 % DMSO, 49.5 µL of DMSOT was added to 0.5 µL of polymerized tubulin.

For the fabrication of contacts, sputtering of 10 nm Ti (as an adhesion layer) was performed onto a rectangular glass slide (70 mm x 25 mm x 1 mm), followed by a 75 nm thick Pt layer. The centre of the rectangular slide was covered using Kapton tape to enable the formation of two Pt pads extending symmetrically along the long axis from the edge to 3.3 mm from the centre and along the entirety of the short axis (top view (Figure 3A); side view (Figure 3B)). A borosilicate coverslip (18 mm in diameter and 0.17 mm in thickness) was placed atop 2 µL of 450 nM tubulin polymer solution on the gap between the pads in the centre of the slide. A d.c power source was used to source this voltage. Electrophoretic flow direction was monitored using an epifluorescence microscope, using an exposure time of 100 ms, taking snapshots every 5 s for 3 minutes. During experiments, we observed that microtubules and two-dimensional tubulin polymers stuck on the surface of glass did not undergo electrophoresis even under the influence of electric fields > 24 $V.cm^{-1}$. Thus, tubulin polymers that were not stuck to the glass slide were evaluated. Cleaning of the slides after experimentation was performed with acetone and methanol rinsing, followed by five minutes exposure to oxygen plasma (Oxford Instruments, Abingdon, UK; NGP80) to remove inorganic impurities from the slide surface.

S5. Simulation of electric fields generated by Pt contacts for electrophoretic transport assay

The slide was simulated using the Electrostatics Module in COMSOL Multiphysics 5.5 as being at the centre of a sphere of air 1 m in radius. The Ti and Pt layers were computationally fabricated using the Layered Material function. The outer boundary of this sphere was specified to be ground. The surface of one of the sputtered layers of the slide was also specified to be 0 V, while the potential on the surface of the other sputtered layer was set to 3 V. The stationary state electric potential through the sphere was subsequently simulated.

S5. G-C_3N_4 and tubulin sheet co-localization fluorescence imaging

Stock G-C_3N_4 solution in water or DMSO was prepared by mixing 0.026 g of G-C_3N_4 powder [283-284] in 5 mL water and DMSO. To investigate co-localization between G-C_3N_4 and tubulin-polymers in 99 % DMSO solutions, 0.5 µL of tubulin stock solution (Section S2) was added to 20 µL of DMSOT. This was followed by the addition of 30 µL of G-C_3N_4 solution. The 50 % DMSOT solution was prepared by adding 30 µL of G-C_3N_4 solution prepared in water and 19.5 µL of DMSOT to 2 uL of polymerized Rhodamine-labelled tubulin stock solution. The 0 % DMSO solution was prepared by adding 30 µL of G-C_3N_4 solution prepared in water and 19.5 µL of BRB80T to 2 uL of 45.45 µM polymerized Rhodamine-labelled tubulin stock solution. G-C_3N_4 solutions were sonicated in a water bath for 30 minutes before adding to tubulin solutions.

S6. Calculation of effective charge of tubulin in DMSO containing solutions

To determine the effective charge of tubulin from ZP values, tubulin was approximated as a charged sphere. Thus, the potential was determined using Equation D4 below:

$$ZP = \frac{Q}{4\pi\varepsilon_0\varepsilon_r} \qquad \text{(Equation D4)}$$

Here, Q is the effective charge of tubulin, while ZP represents zeta potential. $\varepsilon_0$and $\varepsilon_r$are the permittivity of free space and relative permittivity. In the case of 99 % DMSO solutions, the value ε_r of was assumed to be 46.7, in accordance with values shown in Table S2. In the 0 % DMSO solution case, the value of ε_r was assumed to be 78.2.

DYNAMIC LIGHT SCATTERING

To ensure that we had no initial aggregates in these 'starting point' solutions, we measured the hydrodynamic diameter of tubulin (1.13 µM) using DLS (Dynamic Light Scattering). As expected, we found that the hydrodynamic diameter was 6.14 ± 1.97 nm as shown in Figure S2a. This result is consistent with values expected for unpolymerized tubulin, previously reported by us in a previous publication [161]. After polymerization into microtubules, our work reports observations on solutions diluted with either (a) MES80T pH 7 (containing 0% DMSO), which led to the continued stabilization of negatively charged microtubules, or (b) 80 %

DMSOT (20% MES80T), which led to the stabilization of positively charged sheets and aggregates. To compare the size distribution of tubulin polymorphs in both cases, we performed DLS on both dilutions (Figure S2b). Our results showed different size distribution peaks, indicating differing polymorphic size distributions. Our results are consistent with microscopy-based data that indicate the transition of a different polymeric forms of tubulin when it becomes positively charged. Additionally, due to the positive charge of tubulin at MES80 pH 5, we also performed DLS measurements on microtubules diluted in MES80 pH 5. We found that that the size distribution matched that of 80 % DMSO, consistent with a polymorphic transition from microtubules to sheets at low pH values. The noise in Figure S2b is due to Mie scattering, that takes place due to large particles such as microtubules (> 1 um) which can be several micrometers long in our preparations.

SUPPLEMENTARY FIGURES

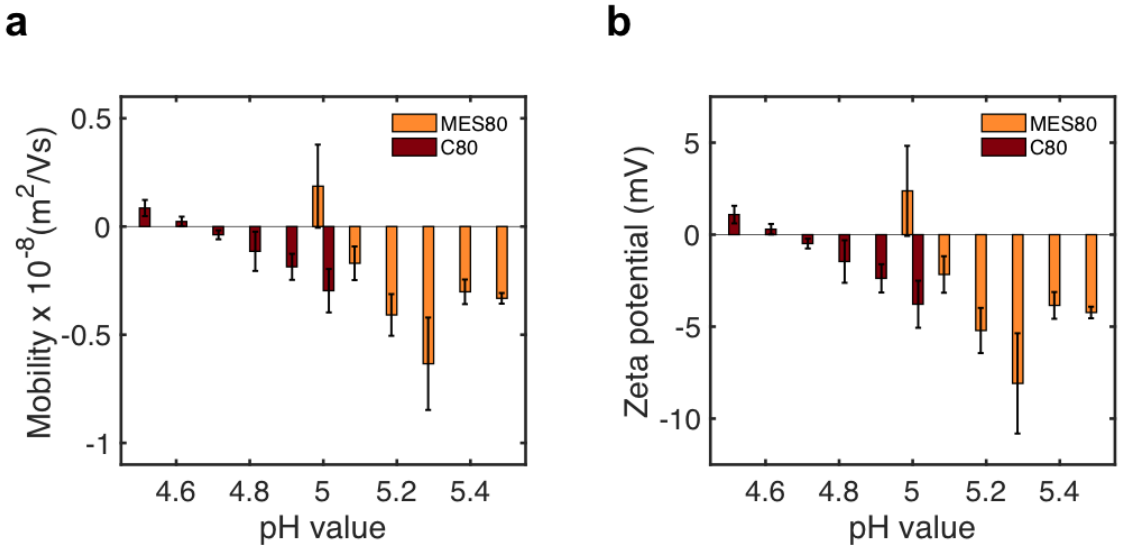

Figure D1. Graphs displaying the variation of (a) mobility and (b) zeta potential as a function of solution pH value for C80 and MES80 buffers. The isoelectric point (pI) of tubulin is approximately 4.6 in C80 and 5 in MES80.

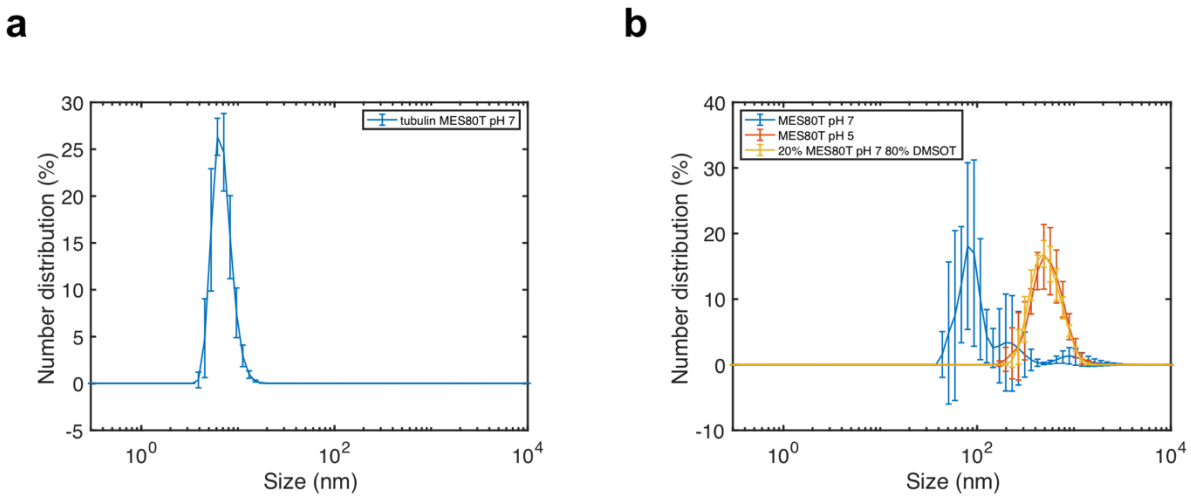

Figure D2. (a) DLS size distribution profiles of unpolymerized 1.13 μm tubulin dissolved in MES80T pH 7. (b) DLS size distribution profiles of polymerized 1.13 μm tubulin diluted in MES80T pH 7, compared to MES80T pH 7 and 80% DMSOT solutions. Error bars represent standard deviation values achieved from n = 5 measurements.

Appendix E: Images of instrumentation used

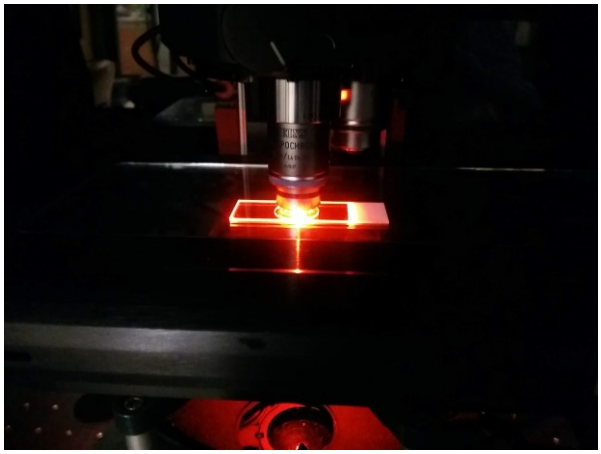

Figure E1. Image showing microtubule solution being exposed to fluorescence microscopy setup for imagining.

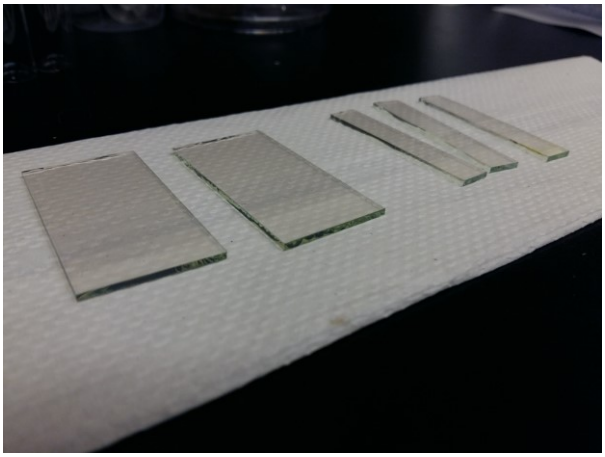

Figure E2. FTO-coated glass slides in broad and thin conformations to fabricate the parallel plate contact electrode geometry used for experiments in Chapter 3.

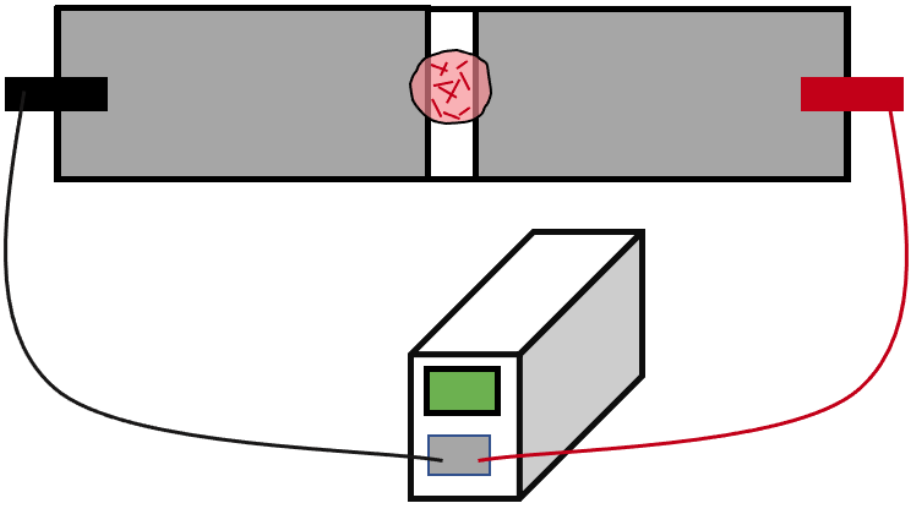

Figure E3. Schematic of setup used for electrophoretic transport assay in Chapter 5. Electrode contact pads are shown in grey. Solution containing microtubules have been shown in red.

References

1. Hagen, J. A.; Li, W.; Steckl, A.; Grote, J., Enhanced Emission Efficiency in Organic Light-Emitting Diodes Using Deoxyribonucleic Acid Complex as an Electron Blocking Layer. *Applied Physics Letters* **2006,** *88* (17), 171109.
2. Hou, Y.; Wang, K.; Yang, D.; Jiang, Y.; Yennawar, N.; Wang, K.; Sanghadasa, M.; Wu, C.; Priya, S., Enhanced performance and stability in DNA-perovskite heterostructure-based solar cells. *ACS Energy Letters* **2019,** *4* (11), 2646-2655.
3. Vahidzadeh, E.; Kalra, A. P.; Shankar, K., Melanin-Based Electronics: From Proton Conductors to Photovoltaics and Beyond. *Biosensors and Bioelectronics* **2018,** *122*, 127-139.
4. Davies, A. M.; Weinberg, U.; Palti, Y., Tumor Treating Fields: A New Frontier in Cancer Therapy. *Annals of the New York Academy of Sciences* **2013,** *1291* (1), 86-95.
5. Nachury, M. V.; Mick, D. U., Establishing and Regulating the Composition of Cilia for Signal Transduction. *Nature Reviews Molecular Cell Biology* **2019,** *20* (7), 389-405.
6. Ichikawa, M.; Bui, K. H., Microtubule Inner Proteins: A Meshwork of Luminal Proteins Stabilizing the Doublet Microtubule. *BioEssays* **2018,** *40* (3), 1700209.
7. de Forges, H.; Bouissou, A.; Perez, F., Interplay Between Microtubule Dynamics and Intracellular Organization. *The international journal of biochemistry & cell biology* **2012,** *44* (2), 266-274.
8. Kapitein, L. C.; Hoogenraad, C. C., Building the Neuronal Microtubule Cytoskeleton. *Neuron* **2015,** *87* (3), 492-506.
9. Tanaka, T. U., Kinetochore–Microtubule Interactions: Steps Towards Bi-Orientation. *The EMBO journal* **2010,** *29* (24), 4070-4082.
10. Hirokawa, N.; Niwa, S.; Tanaka, Y., Molecular Motors in Neurons: Transport Mechanisms and Roles in Brain Function, Development, and Disease. *Neuron* **2010,** *68* (4), 610-638.
11. Maday, S.; Twelvetrees, A. E.; Moughamian, A. J.; Holzbaur, E. L., Axonal Transport: Cargo-Specific Mechanisms of Motility and Regulation. *Neuron* **2014,** *84* (2), 292-309.
12. Kalra, A. P.; Eakins, B. B.; Patel, S. D.; Ciniero, G.; Rezania, V.; Shankar, K.; Tuszynski, J. A., All Wired Up: An Exploration of the Electrical Properties of Microtubules and Tubulin. *ACS Nano* **2020,** *14* (12), 16301-16320.
13. Kalra, A. P.; Patel, S. D.; Bhuiyan, A. F.; Preto, J.; Scheuer, K. G.; Mohammed, U.; Lewis, J. D.; Rezania, V.; Shankar, K.; Tuszynski, J. A., Investigation of the Electrical

Properties of Microtubule Ensembles under Cell-Like Conditions. *Nanomaterials* **2020,** *10* (2), 265.

14. Priel, A.; Tuszyński, J., A Nonlinear Cable-Like Model of Amplified Ionic Wave Propagation along Microtubules. *EPL (Europhysics Letters)* **2008,** *83* (6), 68004.

15. Priel, A.; Ramos, A. J.; Tuszynski, J. A.; Cantiello, H. F., A Biopolymer Transistor: Electrical Amplification by Microtubules. *Biophysical journal* **2006,** *90* (12), 4639-4643.

16. Sekulić, D.; Satarić, M. V., An Improved Nanoscale Transmission Line Model of Microtubule: The Effect of Nonlinearity on the Propagation of Electrical Signals. *Facta Universitatis, Series: Electronics and Energetics* **2014,** *28* (1), 133-142.

17. Sekulić, D. L.; Satarić, M. V., Microtubule as Nanobioelectronic Nonlinear Circuit. *Serbian Journal of Electrical Engineering* **2012,** *9* (1), 107-119.

18. Satarić, M. V.; Nemeš, T.; Sekulić, D.; Tuszynski, J. A., How Signals of Calcium Ions Initiate the Beats of Cilia and Flagella. *Biosystems* **2019,** *182*, 42-51.

19. Cantero, M. d. R.; Gutierrez, B. C.; Cantiello, H. F., Actin Filaments Modulate Electrical Activity of Brain Microtubule Protein Two-Dimensional Sheets. *Cytoskeleton* **2020**.

20. del Rocío Cantero, M.; Perez, P. L.; Scarinci, N.; Cantiello, H. F., Two-Dimensional Brain Microtubule Structures Behave as Memristive Devices. *Scientific reports* **2019,** *9* (1), 1-10.

21. del Rocío Cantero, M.; Etchegoyen, C. V.; Perez, P. L.; Scarinci, N.; Cantiello, H. F., Bundles of Brain Microtubules Generate Electrical Oscillations. *Scientific reports* **2018,** *8* (1), 11899.

22. Mitchison, T.; Kirschner, M., Dynamic Instability of Microtubule Growth. *nature* **1984,** *312* (5991), 237.

23. Mitchison, T.; Kirschner, M., Microtubule Assembly Nucleated by Isolated Centrosomes. *Nature* **1984,** *312* (5991), 232.

24. Gardner, M. K.; Charlebois, B. D.; Jánosi, I. M.; Howard, J.; Hunt, A. J.; Odde, D. J., Rapid Microtubule Self-Assembly Kinetics. *Cell* **2011,** *146* (4), 582-592.

25. Kellogg, E. H.; Hejab, N. M.; Poepsel, S.; Downing, K. H.; DiMaio, F.; Nogales, E., Near-Atomic Model of Microtubule-Tau Interactions. *Science* **2018,** *360* (6394), 1242-1246.

26. Trinczek, B.; Biernat, J.; Baumann, K.; Mandelkow, E.-M.; Mandelkow, E., Domains of Tau Protein, Differential Phosphorylation, and Dynamic Instability of Microtubules. *Molecular biology of the cell* **1995,** *6* (12), 1887-1902.

27. Helenius, J.; Brouhard, G.; Kalaidzidis, Y.; Diez, S.; Howard, J., The Depolymerizing Kinesin MCAK Uses Lattice Diffusion to Rapidly Target Microtubule Ends. *Nature* **2006,** *441* (7089), 115.

28. Vale, R. D.; Milligan, R. A., The Way Things Move: Looking under the Hood of Molecular Motor Proteins. *Science* **2000,** *288* (5463), 88-95.

29. Yildiz, A.; Selvin, P. R., Fluorescence Imaging with One Nanometer Accuracy: Application to Molecular Motors. *Accounts of chemical research* **2005,** *38* (7), 574-582.

30. Arnal, I.; Wade, R. H., How Does Taxol Stabilize Microtubules? *Current biology* **1995,** *5* (8), 900-908.

31. Schiff, P. B.; Fant, J.; Horwitz, S. B., Promotion of Microtubule Assembly *in Vitro* by Taxol. *Nature* **1979,** *277* (5698), 665.

32. Churchill, C. D.; Klobukowski, M.; Tuszynski, J. A., The Unique Binding Mode of Laulimalide to Two Tubulin Protofilaments. *Chemical biology & drug design* **2015,** *86* (2), 190-199.

33. van Echteld, I.; Wechalekar, M. D.; Schlesinger, N.; Buchbinder, R.; Aletaha, D., Colchicine for Acute Gout. *Cochrane database of systematic reviews* **2014,** (8).

34. Margolis, R. L.; Wilson, L., Addition of Colchicine-Tubulin Complex to Microtubule Ends: The Mechanism of Substoichiometric Colchicine Poisoning. *Proceedings of the National Academy of Sciences* **1977,** *74* (8), 3466-3470.

35. Hawkins, T.; Mirigian, M.; Yasar, M. S.; Ross, J. L., Mechanics of Microtubules. *Journal of biomechanics* **2010,** *43* (1), 23-30.

36. Howard, J., Mechanics of motor Proteins and the Cytoskeleton. **2001**.

37. Gittes, F.; Mickey, B.; Nettleton, J.; Howard, J., Flexural Rigidity of Microtubules and Actin Filaments Measured from Thermal Fluctuations in Shape. *The Journal of cell biology* **1993,** *120* (4), 923-934.

38. Jiang, H.; Jiang, L.; Posner, J. D.; Vogt, B. D., Atomistic-Based Continuum Constitutive Relation for Microtubules: Elastic Modulus Prediction. *Computational Mechanics* **2008,** *42* (4), 607-618.

39. Wells, D. B.; Aksimentiev, A., Mechanical Properties of a Complete Microtubule Revealed through Molecular Dynamics Simulation. *Biophysical journal* **2010,** *99* (2), 629-637.

40. Pampaloni, F.; Florin, E.-L., Microtubule Architecture: Inspiration for Novel Carbon Nanotube-Based Biomimetic Materials. *Trends in biotechnology* **2008,** *26* (6), 302-310.

41. Xu, J.; Teslaa, T.; Wu, T.-H.; Chiou, P.-Y.; Teitell, M. A.; Weiss, S., Nanoblade Delivery and Incorporation of Quantum Dot Conjugates into Tubulin Networks in Live Cells. *Nano letters* **2012,** *12* (11), 5669-5672.

42. Platt, M.; Muthukrishnan, G.; Hancock, W. O.; Williams, M. E., Millimeter Scale Alignment of Magnetic Nanoparticle Functionalized Microtubules in Magnetic Fields. *Journal of the American Chemical Society* **2005,** *127* (45), 15686-15687.

43. Saper, G.; Hess, H., Synthetic Systems Powered by Biological Molecular Motors. *Chemical reviews* **2019**.

44. Hiratsuka, Y.; Tada, T.; Oiwa, K.; Kanayama, T.; Uyeda, T. Q., Controlling the Direction of Kinesin-Driven Microtubule Movements along Microlithographic Tracks. *Biophysical Journal* **2001,** *81* (3), 1555-1561.

45. van den Heuvel, M. G.; Butcher, C. T.; Lemay, S. G.; Diez, S.; Dekker, C., Electrical Docking of Microtubules for KInesin-Driven Motility in Nanostructures. *Nano letters* **2005,** *5* (2), 235-241.

46. Lin, C.-T.; Kao, M.-T.; Kurabayashi, K.; Meyhofer, E., Self-Contained,Biomolecular Motor-Driven Protein Sorting and Concentrating in an Ultrasensitive Microfluidic Chip. *Nano Letters* **2008,** *8* (4), 1041-1046.

47. Hess, H.; Vogel, V., Molecular Shuttles Based on Motor Proteins: Active Transport in Synthetic Environments. *Reviews in Molecular Biotechnology* **2001,** *82* (1), 67-85.

48. Reuther, C.; Mittasch, M. u.; Naganathan, S. R.; Grill, S. W.; Diez, S., Highly-Efficient Guiding of Motile Microtubules on Non-Topographical Motor Patterns. *Nano letters* **2017,** *17* (9), 5699-5705.

49. Tas, R. P.; Chen, C.-Y.; Katrukha, E. A.; Vleugel, M.; Kok, M.; Dogterom, M.; Akhmanova, A.; Kapitein, L. C., Guided by Light: Optical Control of Microtubule Gliding Assays. *Nano letters* **2018,** *18* (12), 7524-7528.

50. Hess, H.; Clemmens, J.; Qin, D.; Howard, J.; Vogel, V., Light-Controlled Molecular Shuttles Made from Motor Proteins Carrying Cargo on Engineered Surfaces. *Nano Letters* **2001,** *1* (5), 235-239.

51. Roos, W.; Ulmer, J.; Gräter, S.; Surrey, T.; Spatz, J. P., Microtubule Gliding and Cross-Linked Microtubule Networks on Micropillar Interfaces. *Nano letters* **2005,** *5* (12), 2630-2634.

52. Sikora, A.; Ramón-Azcón, J.; Kim, K.; Reaves, K.; Nakazawa, H.; Umetsu, M.; Kumagai, I.; Adschiri, T.; Shiku, H.; Matsue, T., Molecular Motor-Powered Shuttles along Multi-Walled Carbon Nanotube Tracks. *Nano letters* **2014,** *14* (2), 876-881.

53. Li, J.; Jia, Y.; Dong, W.; Feng, X.; Fei, J.; Li, J., Transporting a Tube in a Tube. *Nano letters* **2014,** *14* (11), 6160-6164.

54. Hess, H.; Howard, J.; Vogel, V., A Piconewton Forcemeter Assembled from Microtubules and Kinesins. *Nano Letters* **2002,** *2* (10), 1113-1115.

55. Dinu, C. Z.; Bale, S. S.; Chrisey, D. B.; Dordick, J. S., Manipulation of Individual Carbon Nanotubes by Reconstructing the Intracellular Transport of a Living Cell. *Advanced Materials* **2009,** *21* (10-11), 1182-1186.

56. Ndlec, F.; Surrey, T.; Maggs, A. C.; Leibler, S., Self-Organization of Microtubules and Motors. *Nature* **1997,** *389* (6648), 305.

57. Sikora, A.; Canova, F. F.; Kim, K.; Nakazawa, H.; Umetsu, M.; Kumagai, I.; Adschiri, T.; Hwang, W.; Teizer, W., Behavior of Kinesin Driven Quantum Dots Trapped in a Microtubule Loop. *ACS Nano* **2015,** *9* (11), 11003-11013.

58. Nicolau, D. V.; Lard, M.; Korten, T.; van Delft, F. C.; Persson, M.; Bengtsson, E.; Månsson, A.; Diez, S.; Linke, H., Parallel Computation with Molecular-Motor-Propelled Agents in Aanofabricated Networks. *Proceedings of the National Academy of Sciences* **2016,** *113* (10), 2591-2596.

59. Nawrotek, A.; Knossow, M.; Gigant, B., The Determinants That Govern Microtubule Assembly from the Atomic Structure of GTP-Tubulin. *Journal of molecular biology* **2011,** *412* (1), 35-42.

60. Baker, N. A.; Sept, D.; Joseph, S.; Holst, M. J.; McCammon, J. A., Electrostatics of Nanosystems: Application to Microtubules and the Ribosome. *Proceedings of the National Academy of Sciences* **2001,** *98* (18), 10037-10041.

61. Dolinsky, T. J.; Nielsen, J. E.; McCammon, J. A.; Baker, N. A., PDB2PQR: An Automated Pipeline for the Setup of Poisson–Boltzmann Electrostatics Calculations. *Nucleic acids research* **2004,** *32* (suppl_2), W665-W667.

62. Isozaki, N.; Shintaku, H.; Kotera, H.; Hawkins, T. L.; Ross, J. L.; Yokokawa, R., Control of Molecular Shuttles by Designing Electrical and Mechanical Properties of Microtubules. *Science Robotics* **2017,** *2* (10), eaan4882.

63. Isozaki, N.; Ando, S.; Nakahara, T.; Shintaku, H.; Kotera, H.; Meyhöfer, E.; Yokokawa, R., Control of Microtubule Trajectory within an Electric Field by Altering Surface Charge Density. *Scientific reports* **2015,** *5*, 7669.

64. Kirson, E. D.; Gurvich, Z.; Schneiderman, R.; Dekel, E.; Itzhaki, A.; Wasserman, Y.; Schatzberger, R.; Palti, Y., Disruption of Cancer Cell Replication by Alternating Electric Fields. *Cancer research* **2004,** *64* (9), 3288-3295.

65. Kirson, E. D.; Schneiderman, R. S.; Dbalý, V.; Tovaryš, F.; Vymazal, J.; Itzhaki, A.; Mordechovich, D.; Gurvich, Z.; Shmueli, E.; Goldsher, D., Chemotherapeutic Treatment Efficacy and Sensitivity Are Increased by Adjuvant Alternating Electric Fields (TTFields). *BMC medical physics* **2009,** *9* (1), 1.

66. Giladi, M.; Schneiderman, R. S.; Voloshin, T.; Porat, Y.; Munster, M.; Blat, R.; Sherbo, S.; Bomzon, Z.; Urman, N.; Itzhaki, A., Mitotic Spindle Disruption by Alternating Electric Fields Leads to Improper Chromosome Segregation and Mitotic Catastrophe in Cancer Cells. *Scientific reports* **2015,** *5*, 18046.

67. Chafai, D. E.; Sulimenko, V.; Havelka, D.; Kubínová, L.; Dráber, P.; Cifra, M., Reversible and Irreversible Modulation of Tubulin Self-Assembly by Intense Nanosecond Pulsed Electric Fields. *Advanced Materials* **2019,** *31* (39), 1903636.

68. Chafai, D. E.; Vostárek, F.; Dráberová, E.; Havelka, D.; Arnaud-Cormos, D.; Leveque, P.; Janáček, J.; Kubínová, L.; Cifra, M.; Dráber, P., Microtubule Cytoskeleton Remodeling by Nanosecond Pulsed Electric Fields. *Advanced Biosystems* **2020**, 2000070.

69. Inoué, S., Polarization Optical Studies of the Mitotic Spindle. *Chromosoma* **1953,** *5* (1), 487-500.

70. Weisenberg, R. C.; Broisy, G. G.; Taylor, E. W., Colchicine-Binding Protein of Mammalian Brain and Its Relation to Microtubules. *Biochemistry* **1968,** *7* (12), 4466-4479.

71. Shelanski, M.; Taylor, E., Isolation of a Protein Subunit from Microtubules. *The Journal of cell biology* **1967,** *34* (2), 549-554.

72. Ponstingl, H.; Krauhs, E.; Little, M.; Kempf, T., Complete Amino Acid Sequence of Alpha-Tubulin from Porcine Brain. *Proceedings of the National Academy of Sciences* **1981,** *78* (5), 2757-2761.

73. Ponstingl, H.; Little, M.; Krauhs, E.; Kempf, T., Carboxy-Terminal Amino Acid Sequence of α-Tubulin from Porcine Brain. *Nature* **1979,** *282* (5737), 423-424.

74. Vassilev, P.; Kanazirska, M.; Tien, H. T., Intermembrane Linkage Mediated by Tubulin. *Biochemical and biophysical research communications* **1985,** *126* (1), 559-565.

75. Vassilev, P. M.; Dronzine, R. T.; Vassileva, M. P.; Georgiev, G. A., Parallel Arrays of Microtubles Formed in Electric and Magnetic Fields. *Bioscience reports* **1982,** *2* (12), 1025-1029.

76. Turner, D. C.; Chang, C.; Fang, K.; Brandow, S. L.; Murphy, D. B., Selective Adhesion of Functional Microtubules to Patterned Silane Surfaces. *Biophysical Journal* **1995,** *69* (6), 2782-2789.

77. Freedman, H.; Rezania, V.; Priel, A.; Carpenter, E.; Noskov, S. Y.; Tuszynski, J. A., Model of Ionic Currents through Microtubule Nanopores and the Lumen. *Physical Review E* **2010,** *81* (5), 051912.

78. Priel, A.; Tuszynski, J. A.; Woolf, N. J., Transitions in Microtubule C-Termini Conformations as a Possible Dendritic Signaling Phenomenon. *European Biophysics Journal* **2005,** *35* (1), 40.

79. Van den Heuvel, M.; De Graaff, M.; Lemay, S.; Dekker, C., Electrophoresis of Individual Microtubules in Microchannels. *Proceedings of the National Academy of Sciences* **2007,** *104* (19), 7770-7775.

80. Van den Heuvel, M. G.; De Graaff, M. P.; Dekker, C., Molecular Sorting by Electrical Steering of Microtubules in Kinesin-Coated Channels. *Science* **2006,** *312* (5775), 910-914.

81. Santelices, I. B.; Friesen, D. E.; Bell, C.; Hough, C. M.; Xiao, J.; Kalra, A.; Kar, P.; Freedman, H.; Rezania, V.; Lewis, J. D.; Shankar, K.; Tuszyński, J., Response to Alternating Electric Fields of Tubulin Dimers and Microtubule Ensembles in Electrolytic Solutions. *Scientific reports* **2017,** *7* (1), 9594.

82. Bachand, G. D.; Rivera, S. B.; Boal, A. K.; Gaudioso, J.; Liu, J.; Bunker, B. C., Assembly and Transport of Nanocrystal CdSe Quantum Dot Nanocomposites Using Microtubules and Kinesin Motor Proteins. *Nano Letters* **2004,** *4* (5), 817-821.

83. Adrian, M.; Nijenhuis, W.; Hoogstraaten, R. I.; Willems, J.; Kapitein, L. C., A Phytochrome-Derived Photoswitch for Intracellular Transport. *ACS synthetic biology* **2017,** *6* (7), 1248-1256.

84. Hutchins, B. M.; Platt, M.; Hancock, W. O.; Williams, M. E., Directing Transport of CoFe2O4-Functionalized Microtubules With Magnetic Fields. *small* **2007,** *3* (1), 126-131.

85. Jia, L.; Moorjani, S. G.; Jackson, T. N.; Hancock, W. O., Microscale Transport and Sorting by Kinesin Molecular Motors. *Biomedical microdevices* **2004,** *6* (1), 67-74.

86. Hyman, A. A.; Salser, S.; Drechsel, D.; Unwin, N.; Mitchison, T. J., Role of GTP Hydrolysis in Microtubule Dynamics: Information from a Slowly Hydrolyzable Analogue, GMPCPP. *Molecular biology of the cell* **1992,** *3* (10), 1155-1167.

87. Stracke, R.; Böhm, K.; Wollweber, L.; Tuszynski, J.; Unger, E., Analysis of the Migration Behaviour of Single Microtubules in Electric Fields. *Biochemical and biophysical research communications* **2002,** *293* (1), 602-609.

88. Böhm, K. J.; Mavromatos, N. E.; Michette, A.; Stracke, R.; Unger, E., Movement and Alignment of Microtubules in Electric Fields and Electric-Dipole-Moment Estimates. *Electromagnetic Biology and Medicine* **2005,** *24* (3), 319-330.

89. Detrich, H. W.; Overton, S., Heterogeneity and Structure of Brain Tubulins from Cold-Adapted Antarctic fishes. Comparison to Brain Tubulins from a Temperate Fish and a Mammal. *Journal of Biological Chemistry* **1986,** *261* (23), 10922-10930.

90. Linhartová, I.; Dráberová, E.; Viklický, V.; Dráber, P., Distribution of Non-Class-III β-Tubulin Isoforms in Neuronal and Non-Neuronal Cells. *FEBS letters* **1993,** *320* (1), 79-82.

91. Ramalho, R.; Soares, H.; Melo, L., Microtubule Behavior under Strong Electromagnetic Fields. *Materials Science and Engineering: C* **2007,** *27* (5-8), 1207-1210.

92. Vale, R. D., The Molecular Motor Toolbox for Intracellular Transport. *Cell* **2003,** *112* (4), 467-480.

93. Guzman-Sepulveda, J. R.; Wu, R.; Kalra, A. P.; Aminpour, M.; Tuszynski, J. A.; Dogariu, A., Tubulin Polarizability in Aqueous Suspensions. *ACS omega* **2019,** *4* (5), 9144-9149.

94. Kim, T.; Kao, M.-T.; Hasselbrink, E. F.; Meyhöfer, E., Nanomechanical Model of Microtubule Translocation in the Presence of Electric Fields. *Biophysical journal* **2008,** *94* (10), 3880-3892.

95. Tuszyński, J.; Brown, J.; Crawford, E.; Carpenter, E.; Nip, M.; Dixon, J.; Satarić, M., Molecular Dynamics Simulations of Tubulin Structure and Calculations of Electrostatic Properties of Microtubules. *Mathematical and Computer Modelling* **2005,** *41* (10), 1055-1070.

96. Freedman, H.; Luchko, T.; Luduena, R. F.; Tuszynski, J. A., Molecular Dynamics Modeling of Tubulin C-Terminal Tail Interactions with the Microtubule Surface. *Proteins: Structure, Function, and Bioinformatics* **2011,** *79* (10), 2968-2982.

97. Luchko, T.; Huzil, J. T.; Stepanova, M.; Tuszynski, J., Conformational Analysis of the Carboxy-Terminal Tails of Human β-Tubulin Isotypes. *Biophysical Journal* **2008,** *94* (6), 1971-1982.

98. Gaskin, F.; Cantor, C. R.; Shelanski, M. L., Turbidimetric Studies of the *in Vitro* Assembly and Disassembly of Porcine Neurotubules. *Journal of molecular biology* **1974,** *89* (4), 737-755.

99. Bonhaus, D. W.; McCormack, K. M.; Mayor, G. H.; Mattson, J. C.; Hook, J. B., The Effects of Aluminum on Microtubular Integrity Using *in Vitro* and *in Vivo* Models. *Toxicology Letters* **1980,** *6* (3), 141-147.

100. Shevtsov, P.; Shevtsova, E.; Burbaeva, G. S., Effect of Aluminum, Iron, and Zinc Ions on the Assembly of Microtubules from Brain Microtubule Proteins. *Bulletin of experimental biology and medicine* **2016,** *161* (4), 451-455.

101. Bouxsein, N. F.; Bachand, G. D., Single Filament Behavior of Microtubules in the Presence of Added Divalent Counterions. *Biomacromolecules* **2014,** *15* (10), 3696-3705.

102. Nicholson, W. V.; Lee, M.; Downing, K. H.; Nogales, E., Cryo-Electron Microscopy of GDP-Tubulin Rings. *Cell biochemistry and biophysics* **1999,** *31* (2), 175-183.

103. Bhattacharya, A.; Bhattacharyya, B.; Roy, S., Magnesium-Induced Structural Changes in Tubulin. *Journal of Biological Chemistry* **1994,** *269* (46), 28655-28661.

104. Gaskin, F.; Kress, Y., Zinc Ion-Induced Assembly of Tubulin. *Journal of Biological Chemistry* **1977,** *252* (19), 6918-6924.

105. Gaskin, F., *In Vitro* Microtubule Assembly Regulation by Divalent Cations and Nucleotides. *Biochemistry* **1981,** *20* (5), 1318-1322.

106. Larsson, H.; Wallin, M.; Edström, A., Induction of a Sheet Polymer of Tubulin by Zn2+. *Experimental cell research* **1976,** *100* (1), 104-110.

107. Serrano, L.; De La Torre, J.; Maccioni, R. B.; Avila, J., Involvement of the Carboxyl-Terminal Domain of Tubulin in the Regulation of Its Assembly. *Proceedings of the National Academy of Sciences* **1984,** *81* (19), 5989-5993.

108. Wolf, S. G.; Mosser, G.; Downing, K. H., Tubulin Conformation in Zinc-Induced Sheets and Macrotubes. *Journal of structural biology* **1993,** *111* (3), 190-199.

109. Weisenberg, R. C., Microtubule Formation *in Vitro* in Solutions Containing Low Calcium Concentrations. *Science* **1972,** *177* (4054), 1104-1105.

110. O'Brien, E. T.; Salmon, E.; Erickson, H. P., How Calcium Causes Microtubule Depolymerization. *Cell motility and the cytoskeleton* **1997,** *36* (2), 125-135.

111. Olmsted, J.; Borisy, G., Ionic and Nucleotide Requirements for Microtubule Polymerization *in Vitro*. *Biochemistry* **1975,** *14* (13), 2996-3005.

112. Vogel, D. G.; Margolis, R. L.; Mottet, N. K., Analysis of Methyl Mercury Binding Sites on Tubulin Subunits and Microtubules. *Pharmacology & toxicology* **1989,** *64* (2), 196-201.

113. Vogel, D. G.; Margolis, R. L.; Mottet, N. K., The Effects of Methyl Mercury Binding to Microtubules. *Toxicology and applied pharmacology* **1985,** *80* (3), 473-486.

114. Needleman, D. J.; Ojeda-Lopez, M. A.; Raviv, U.; Miller, H. P.; Wilson, L.; Safinya, C. R., Higher-Order Assembly of Microtubules by Counterions: From Hexagonal Bundles to Living Necklaces. *Proceedings of the National Academy of Sciences* **2004,** *101* (46), 16099-16103.

115. Maurer, S. P.; Cade, N. I.; Bohner, G.; Gustafsson, N.; Boutant, E.; Surrey, T., EB1 Accelerates Two Conformational Transitions Important for Microtubule Maturation and Dynamics. *Current Biology* **2014,** *24* (4), 372-384.

116. Duellberg, C.; Fourniol, F. J.; Maurer, S. P.; Roostalu, J.; Surrey, T., End-Binding Proteins and Ase1/PRC1 Define Local Functionality of Structurally Distinct Parts of the Microtubule Cytoskeleton. *Trends in cell biology* **2013,** *23* (2), 54-63.

117. Honnappa, S.; Gouveia, S. M.; Weisbrich, A.; Damberger, F. F.; Bhavesh, N. S.; Jawhari, H.; Grigoriev, I.; van Rijssel, F. J.; Buey, R. M.; Lawera, A., An EB1-Binding Motif Acts as a Microtubule Tip Localization Signal. *Cell* **2009,** *138* (2), 366-376.

118. Carr, L.; Bardet, S. M.; Burke, R. C.; Arnaud-Cormos, D.; Lévêque, P.; O'connor, R. P., Calcium-Independent Disruption of Microtubule Dynamics by Nanosecond Pulsed Electric Fields in U87 Human Glioblastoma Cells. *Scientific reports* **2017,** *7* (1), 1-12.

119. Thompson, G. L.; Roth, C. C.; Dalzell, D. R.; Kuipers, M. A.; Ibey, B. L., Calcium Influx Affects Intracellular Transport and Membrane Repair following Nanosecond Pulsed Electric Field Exposure. *Journal of biomedical optics* **2014,** *19* (5), 055005.

120. Kim, T.; Kao, M.-T.; Hasselbrink, E. F.; Meyhöfer, E., Active Alignment of Microtubules with Electric Fields. *Nano Letters* **2007,** *7* (1), 211-217.

121. Shibata, K.; Miura, M.; Watanabe, Y.; Saito, K.; Nishimura, A.; Furuta, K. y.; Toyoshima, Y. Y., A Single Protofilament is Sufficient to Support Unidirectional Walking of Dynein and Kinesin. *PLoS One* **2012,** *7* (8), e42990.

122. Wenger, C.; Miranda, P. C.; Salvador, R.; Thielscher, A.; Bomzon, Z.; Giladi, M.; Mrugala, M. M.; Korshoej, A. R., A Review on Tumor-Treating Tields (TTFields): Clinical Implications Inferred from Computational Modeling. *IEEE Reviews in Biomedical Engineering* **2018,** *11*, 195-207.

123. Hille, B., *Ionic Channels of Excitable Membranes*. Sinauer Associates: Sunderland, Massachusetts, 1984.

124. King, R. W.; Wu, T. T., Calculated Electric Field Induced in Bundles of Long Cells in the Human Body When It Is Exposed to Low-Frequency Electric Fields. *Radiation Research* **2000,** *153* (5), 715-721.

125. Satarić, M.; Ilić, D.; Ralević, N.; Tuszynski, J. A., A Nonlinear Model of Ionic Wave Propagation along Microtubules. *European biophysics journal* **2009,** *38* (5), 637-647.

126. Umnov, M.; Palusinski, O.; Deymier, P. A.; Guzman, R.; Hoying, J.; Barnaby, H.; Yang, Y.; Raghavan, S., Experimental Evaluation of Electrical Conductivity of Microtubules. *Journal of materials science* **2007,** *42* (1), 373-378.

127. Minoura, I.; Muto, E., Dielectric Measurement of Individual Microtubules Using the Electroorientation Method. *Biophysical journal* **2006,** *90* (10), 3739-3748.

128. Uppalapati, M.; Huang, Y. M.; Jackson, T. N.; Hancock, W. O., Microtubule Alignment and Manipulation Using AC Electrokinetics. *small* **2008,** *4* (9), 1371-1381.

129. Wenger, C.; Salvador, R.; Basser, P. J.; Miranda, P. C., The Electric Field Distribution in the Brain during TTFields Therapy and Its Dependence on Tissue Dielectric Properties and Anatomy: A Computational Study. *Physics in Medicine & Biology* **2015,** *60* (18), 7339.

130. Van Eunen, K.; Bouwman, J.; Daran-Lapujade, P.; Postmus, J.; Canelas, A. B.; Mensonides, F. I.; Orij, R.; Tuzun, I.; Van Den Brink, J.; Smits, G. J., Measuring Enzyme Activities under Standardized *in Vivo*-Like Conditions for Systems Biology. *The FEBS journal* **2010,** *277* (3), 749-760.

131. Theillet, F.-X.; Binolfi, A.; Frembgen-Kesner, T.; Hingorani, K.; Sarkar, M.; Kyne, C.; Li, C.; Crowley, P. B.; Gierasch, L.; Pielak, G. J., Physicochemical Properties of Cells and Their Effects on Intrinsically Disordered Proteins (IDPs). *Chemical reviews* **2014,** *114* (13), 6661-6714.

132. Shen, C.; Guo, W., Ion Permeability of a Microtubule in Neuron Environment. *The journal of physical chemistry letters* **2018,** *9* (8), 2009-2014.

133. del Rocío Cantero, M.; Perez, P. L.; Smoler, M.; Etchegoyen, C. V.; Cantiello, H. F., Electrical Oscillations in Two-Dimensional Microtubular Structures. *Scientific Reports* **2016,** *6*, 27143.

134. Gutierrez, B. C.; Cantiello, H. F.; del Rocío Cantero, M., Electrical Oscillations of Brain Microtubules. *bioRxiv* **2020**.

135. Tuszynski, J. A.; Friesen, D.; Freedman, H.; Sbitnev, V. I.; Kim, H.; Santelices, I.; Kalra, A. P.; Patel, S. D.; Shankar, K.; Chua, L. O., Microtubules as Sub-Cellular Memristors. *Scientific Reports* **2020,** *10* (1), 1-11.

136. Sackett, D. L.; Bhattacharyya, B.; Wolff, J., Tubulin Subunit Carboxyl Termini Determine Polymerization Efficiency. *Journal of Biological Chemistry* **1985,** *260* (1), 43-45.

137. Zhang, R.; Roostalu, J.; Surrey, T.; Nogales, E., Structural Insight into TPX2-Stimulated Microtubule Assembly. *Elife* **2017,** *6*, e30959.

138. Coles, C. H.; Bradke, F., Coordinating Neuronal Actin–Microtubule Dynamics. *Current Biology* **2015,** *25* (15), R677-R691.

139. Griffith, L.; Pollard, T., The Interaction of Actin Filaments with Microtubules and Microtubule-Associated Proteins. *Journal of Biological Chemistry* **1982,** *257* (15), 9143-9151.

140. Lin, E. C.; Cantiello, H., A Novel Method to Study the Electrodynamic Behavior of Actin Filaments. Evidence for Cable-Like Properties of Actin. *Biophysical journal* **1993,** *65* (4), 1371.

141. Chua, L., Memristor-The Missing Circuit Element. *IEEE Transactions on circuit theory* **1971,** *18* (5), 507-519.

142. Tuszynski, J., Microtubule IV Characteristics Are Consistent with Memristor-Like Behavior. **2016**.

143. Chiolerio, A.; Draper, T. C.; Mayne, R.; Adamatzky, A., On Resistance Switching and Oscillations in Tubulin Microtubule Droplets. *Journal of colloid and interface science* **2020,** *560*, 589-595.

144. Borghetti, J.; Snider, G. S.; Kuekes, P. J.; Yang, J. J.; Stewart, D. R.; Williams, R. S., 'Memristive' Switches Enable 'Stateful' Logic Operations *via* Material Implication. *Nature* **2010,** *464* (7290), 873-876.

145. Jo, S. H.; Chang, T.; Ebong, I.; Bhadviya, B. B.; Mazumder, P.; Lu, W., Nanoscale Memristor Device as Synapse in Neuromorphic Systems. *Nano letters* **2010,** *10* (4), 1297-1301.

146. He, H.; Mortellaro, M. A.; Leiner, M. J. P.; Fraatz, R. J.; Tusa, J. K., A Fluorescent Sensor with High Selectivity and Sensitivity for Potassium in Water. *Journal of the American Chemical Society* **2003,** *125* (6), 1468-1469.

147. Wang, H.; Vagin, S. I.; Rieger, B.; Meldrum, A., An Ultrasensitive Fluorescent Paper-Based CO2 Sensor. *ACS Applied Materials & Interfaces* **2020,** *12* (18), 20507-20513.

148. Merzlyak, P. G.; Capistrano, M.-F. P.; Valeva, A.; Kasianowicz, J. J.; Krasilnikov, O. V., Conductance and Ion Selectivity of a Mesoscopic Protein Nanopore Probed with Cysteine Scanning Mutagenesis. *Biophysical Journal* **2005,** *89* (5), 3059-3070.

149. Chen, C.-C.; Zhou, Y.; Baker, L. A., Single-Nanopore Investigations with Ion Conductance Microscopy. *ACS Nano* **2011,** *5* (10), 8404-8411.

150. Carlsen, A. T.; Zahid, O. K.; Ruzicka, J.; Taylor, E. W.; Hall, A. R., Interpreting the Conductance Blockades of DNA Translocations through Solid-State Nanopores. *ACS Nano* **2014,** *8* (5), 4754-4760.

151. Gracheva, M. E.; Melnikov, D. V.; Leburton, J.-P., Multilayered Semiconductor Membranes for Nanopore Ionic Conductance Modulation. *ACS Nano* **2008,** *2* (11), 2349-2355.

152. Adamatzky, A.; Tuszynski, J.; Pieper, J.; Nicolau, D. V.; Rinalndi, R.; Sirakoulis, G.; Erokhin, V.; Schnauss, J.; Smith, D. M., Towards Cytoskeleton Computers. A Proposal. *arXiv preprint arXiv:1810.04981* **2018**.

153. Singh, S.; Krishnaswamy, J. A.; Melnik, R., Biological Cells and Coupled Electro-Mechanical Effects: The Role of Organelles, Microtubules, and Nonlocal Contributions. *Journal of the Mechanical Behavior of Biomedical Materials* **2020**, 103859.

154. Gerdes, H.-H.; Carvalho, R. N., Intercellular Transfer Mediated by Tunneling Nanotubes. *Current opinion in cell biology* **2008,** *20* (4), 470-475.
155. Gerdes, H.-H.; Rustom, A.; Wang, X., Tunneling Nanotubes, an Emerging Intercellular Communication Route in Development. *Mechanisms of development* **2013,** *130* (6-8), 381-387.
156. Önfelt, B.; Nedvetzki, S.; Benninger, R. K.; Purbhoo, M. A.; Sowinski, S.; Hume, A. N.; Seabra, M. C.; Neil, M. A.; French, P. M.; Davis, D. M., Structurally Distinct Membrane Nanotubes between Human Macrophages Support Long-Distance Vesicular Traffic or Surfing of Bacteria. *The Journal of Immunology* **2006,** *177* (12), 8476-8483.
157. Wang, X.; Gerdes, H.-H., Transfer of Mitochondria *via* Tunneling Nanotubes Rescues Apoptotic PC12 Cells. *Cell Death & Differentiation* **2015,** *22* (7), 1181-1191.
158. Osswald, M.; Jung, E.; Sahm, F.; Solecki, G.; Venkataramani, V.; Blaes, J.; Weil, S.; Horstmann, H.; Wiestler, B.; Syed, M., Brain Tumour Cells Interconnect to a Functional and Resistant Network. *Nature* **2015,** *528* (7580), 93-98.
159. Smith, I. F.; Shuai, J.; Parker, I., Active Generation and Propagation of Ca2+ Signals within Tunneling Membrane Nanotubes. *Biophysical journal* **2011,** *100* (8), L37-L39.
160. Osswald, M.; Jung, E.; Wick, W.; Winkler, F., Tunneling Nanotube-Like Structures in Brain Tumors. *Cancer Reports* **2019,** *2* (6), e1181.
161. Kalra, A. P.; Kar, P.; Preto, J.; Rezania, V.; Dogariu, A.; Lewis, J. D.; Tuszynski, J.; Shankar, K., Behavior of α, β Tubulin in DMSO-Containing Electrolytes. *Nanoscale Advances* **2019**.
162. Habicht, W.; Behrens, S.; Unger, E.; Dinjus, E., Cylindrical and Ring-Shaped Tubulin Assemblies as Metallization Templates Explored by FESEM/EDX and SFM. *Surface and Interface Analysis: An International Journal devoted to the development and application of techniques for the analysis of surfaces, interfaces and thin films* **2006,** *38* (4), 194-197.
163. Kirsch, R.; Mertig, M.; Pompe, W.; Wahl, R.; Sadowski, G.; Böhm, K.; Unger, E., Three-Dimensional Metallization of Microtubules. *Thin solid films* **1997,** *305* (1-2), 248-253.
164. Habicht, W.; Behrens, S.; Böhm, K.; Dinjus, E. In *Imaging of Self-Assembled Tubulin Polymorphs Used as Metallization Templates*, J. Phys.: Conf. Ser, 2007; pp 374-378.
165. Mershin, A.; Kolomenski, A. A.; Schuessler, H. A.; Nanopoulos, D. V., Tubulin dipole moment, dielectric constant and quantum behavior: computer simulations, experimental results and suggestions. *Biosystems* **2004,** *77* (1-3), 73-85.
166. Timmons, J. J.; Preto, J.; Tuszynski, J. A.; Wong, E. T., Tubulin's response to external electric fields by molecular dynamics simulations. *PloS one* **2018,** *13* (9), e0202141.

167. Preto, J.; Pettini, M.; Tuszynski, J. A., Possible role of electrodynamic interactions in long-distance biomolecular recognition. *Physical Review E* **2015,** *91* (5), 052710.

168. Barvitenko, N.; Lawen, A.; Aslam, M.; Pantaleo, A.; Saldanha, C.; Skverchinskaya, E.; Regolini, M.; Tuszynski, J. A., Integration of intracellular signaling: Biological analogues of wires, processors and memories organized by a centrosome 3D reference system. *Biosystems* **2018**.

169. Friesen, D. E.; Craddock, T. J.; Kalra, A. P.; Tuszynski, J. A., Biological wires, communication systems, and implications for disease. *Biosystems* **2015,** *127*, 14-27.

170. Sekulić, D. L.; Satarić, B. M.; Tuszynski, J. A.; Satarić, M. V., Nonlinear ionic pulses along microtubules. *The European Physical Journal E* **2011,** *34* (5), 49.

171. Cifra, M.; Pokorný, J.; Havelka, D.; Kučera, O., Electric field generated by axial longitudinal vibration modes of microtubule. *BioSystems* **2010,** *100* (2), 122-131.

172. Dujovne, I.; van den Heuvel, M.; Shen, Y.; de Graaff, M.; Dekker, C., Velocity modulation of microtubules in electric fields. *Nano letters* **2008,** *8* (12), 4217-4220.

173. Tuszynski, J.; Wenger, C.; Friesen, D.; Preto, J., An overview of sub-cellular mechanisms involved in the action of TTFields. *International journal of environmental research and public health* **2016,** *13* (11), 1128.

174. Shelden, E.; Wadsworth, P., Observation and quantification of individual microtubule behavior in vivo: microtubule dynamics are cell-type specific. *The Journal of cell biology* **1993,** *120* (4), 935-945.

175. Van de Water, L.; Olmsted, J., The quantitation of tubulin in neuroblastoma cells by radioimmunoassay. *Journal of Biological Chemistry* **1980,** *255* (22), 10744-10751.

176. Umnov, M.; Palusinski, O.; Deymier, P.; Guzman, R.; Hoying, J.; Barnaby, H.; Yang, Y.; Raghavan, S., Experimental evaluation of electrical conductivity of microtubules. *Journal of materials science* **2007,** *42* (1), 373-378.

177. Fritzsche, W.; Böhm, K.; Unger, E.; Köhler, J. M., Making electrical contact to single molecules. *Nanotechnology* **1998,** *9* (3), 177.

178. Fritzsche, W.; Köhler, J. M.; Böhm, K. J.; Unger, E.; Wagner, T.; Kirsch, R.; Mertig, M.; Pompe, W., Wiring of metallized microtubules by electron beam-induced structuring. *Nanotechnology* **1999,** *10* (3), 331.

179. Gell, C.; Bormuth, V.; Brouhard, G. J.; Cohen, D. N.; Diez, S.; Friel, C. T.; Helenius, J.; Nitzsche, B.; Petzold, H.; Ribbe, J., Microtubule dynamics reconstituted in vitro and imaged by single-molecule fluorescence microscopy. In *Methods in cell biology*, Elsevier: 2010; Vol. 95, pp 221-245.

180. Taylor, S.; Gileadi, E., Physical interpretation of the Warburg impedance. *Corrosion* **1995,** *51* (9), 664-671.

181. Ramos-Barrado, J.; Galan Montenegro, P.; Cambón, C. C., A generalized Warburg impedance for a nonvanishing relaxation process. *The Journal of chemical physics* **1996,** *105* (7), 2813-2815.

182. Sanabria, H.; Miller Jr, J. H., Relaxation processes due to the electrode-electrolyte interface in ionic solutions. *Physical Review E* **2006,** *74* (5), 051505.

183. Lima, L. F.; Vieira, A. L.; Mukai, H.; Andrade, C. M.; Fernandes, P. R., Electric impedance of aqueous KCl and NaCl solutions: Salt concentration dependence on components of the equivalent electric circuit. *Journal of Molecular Liquids* **2017,** *241*, 530-539.

184. Lenzi, E.; Fernandes, P.; Petrucci, T.; Mukai, H.; Ribeiro, H.; Lenzi, M.; Gonçalves, G., Anomalous diffusion and electrical response of ionic solutions. *Int. J. Electrochem. Sci* **2013,** *8*, 2849-2862.

185. Wilson, L.; Miller, H. P.; Farrell, K. W.; Snyder, K. B.; Thompson, W. C.; Purich, D. L., Taxol stabilization of microtubules in vitro: dynamics of tubulin addition and loss at opposite microtubule ends. *Biochemistry* **1985,** *24* (19), 5254-5262.

186. Mikhaylova, M.; Cloin, B. M.; Finan, K.; Van Den Berg, R.; Teeuw, J.; Kijanka, M. M.; Sokolowski, M.; Katrukha, E. A.; Maidorn, M.; Opazo, F., Resolving bundled microtubules using anti-tubulin nanobodies. *Nature communications* **2015,** *6*, 7933.

187. Herold, C.; Leduc, C.; Stock, R.; Diez, S.; Schwille, P., Long-Range Transport of Giant Vesicles along Microtubule Networks. *ChemPhysChem* **2012,** *13* (4), 1001-1006.

188. Kulić, I. M.; Brown, A. E.; Kim, H.; Kural, C.; Blehm, B.; Selvin, P. R.; Nelson, P. C.; Gelfand, V. I., The role of microtubule movement in bidirectional organelle transport. *Proceedings of the National Academy of Sciences* **2008,** *105* (29), 10011-10016.

189. Olmsted, J.; Borisy, G., Characterization of microtubule assembly in porcine brain extracts by viscometry. *Biochemistry* **1973,** *12* (21), 4282-4289.

190. Satarić, M.; Sekulić, D.; Živanov, M., Solitonic ionic currents along microtubules. *Journal of Computational and Theoretical Nanoscience* **2010,** *7* (11), 2281-2290.

191. Sanabria, H.; Miller Jr, J. H.; Mershin, A.; Luduena, R. F.; Kolomenski, A. A.; Schuessler, H. A.; Nanopoulos, D. V., Impedance spectroscopy of α-β tubulin heterodimer suspensions. *Biophysical journal* **2006,** *90* (12), 4644-4650.

192. Manning, G. S., Limiting laws and counterion condensation in polyelectrolyte solutions I. Colligative properties. *The journal of chemical Physics* **1969,** *51* (3), 924-933.

193. Tuszyński, J.; Portet, S.; Dixon, J.; Luxford, C.; Cantiello, H., Ionic wave propagation along actin filaments. *Biophysical journal* **2004,** *86* (4), 1890-1903.

194. Aouaichia, M.; McCullen, N.; Bowen, C. R.; Almond, D. P.; Budd, C.; Bouamrane, R., Understanding the anomalous frequency responses of composite materials using very large random resistor-capacitor networks. *The European Physical Journal B* **2017,** *90* (3), 39.

195. Panteny, S.; Stevens, R.; Bowen, C., The frequency dependent permittivity and AC conductivity of random electrical networks. *Ferroelectrics* **2005,** *319* (1), 199-208.

196. Parri, H. R.; Gould, T. M.; Crunelli, V., Spontaneous astrocytic Ca 2+ oscillations in situ drive NMDAR-mediated neuronal excitation. *Nature neuroscience* **2001,** *4* (8), 803.

197. Regula, C.; Berlin, R., Microtubule assembly and disassembly at alkaline pH. *The Journal of cell biology* **1981,** *89* (1), 45-53.

198. Borisy, G.; Marcum, J.; Olmsted, J.; Murphy, D.; Johnson, K., Purification of tubulin and associated high molecular weight proteins from porcine brain and characterization of microtubule assembly in vitro. *Annals of the New York Academy of Sciences* **1975,** *253* (1), 107-132.

199. Zhai, Y.; Kronebusch, P. J.; Simon, P. M.; Borisy, G. G., Microtubule dynamics at the G2/M transition: abrupt breakdown of cytoplasmic microtubules at nuclear envelope breakdown and implications for spindle morphogenesis. *The Journal of cell biology* **1996,** *135* (1), 201-214.

200. Zhai, Y.; Borisy, G. G., Quantitative determination of the proportion of microtubule polymer present during the mitosis-interphase transition. *Journal of Cell Science* **1994,** *107* (4), 881-890.

201. Kline-Smith, S. L.; Walczak, C. E., Mitotic spindle assembly and chromosome segregation: refocusing on microtubule dynamics. *Molecular cell* **2004,** *15* (3), 317-327.

202. Akhmanova, A.; Dogterom, M., Kinesins lead aging microtubules to catastrophe. *Cell* **2011,** *147* (5), 966-968.

203. Bugiel, M.; Mitra, A.; Girardo, S.; Diez, S.; Schäffer, E., Measuring microtubule supertwist and defects by three-dimensional-force-clamp tracking of single kinesin-1 motors. *Nano letters* **2018,** *18* (2), 1290-1295.

204. Diez, S.; Reuther, C.; Dinu, C.; Seidel, R.; Mertig, M.; Pompe, W.; Howard, J., Stretching and transporting DNA molecules using motor proteins. *Nano Letters* **2003,** *3* (9), 1251-1254.

205. Hess, H.; Saper, G., Engineering with biomolecular motors. *Accounts of chemical research* **2018,** *51* (12), 3015-3022.

206. Song, W.; Zhu, J.; Kong, W.; Möhwald, H.; Li, J., Different Microtubule Structures Assembled by Kinesin Motors. *Langmuir* **2018,** *34* (33), 9768-9773.

207. Fujimoto, K.; Kitamura, M.; Yokokawa, M.; Kanno, I.; Kotera, H.; Yokokawa, R., Colocalization of quantum dots by reactive molecules carried by motor proteins on polarized microtubule arrays. *ACS nano* **2012,** *7* (1), 447-455.

208. Lam, A. T.-C.; Tsitkov, S.; Zhang, Y.; Hess, H., Reversibly bound kinesin-1 motor proteins propelling microtubules demonstrate dynamic recruitment of active building blocks. *Nano letters* **2018,** *18* (2), 1530-1534.

209. Yokokawa, R.; Takeuchi, S.; Kon, T.; Nishiura, M.; Sutoh, K.; Fujita, H., Unidirectional transport of kinesin-coated beads on microtubules oriented in a microfluidic device. *Nano Letters* **2004,** *4* (11), 2265-2270.

210. Fujimoto, K.; Morita, Y.; Iino, R.; Tomishige, M.; Shintaku, H.; Kotera, H.; Yokokawa, R., Simultaneous Observation of Kinesin-Driven Microtubule Motility and Binding of Adenosine Triphosphate Using Linear Zero-Mode Waveguides. *ACS nano* **2018,** *12* (12), 11975-11985.

211. Wieczorek, M.; Chaaban, S.; Brouhard, G. J., Macromolecular crowding pushes catalyzed microtubule growth to near the theoretical limit. *Cellular and Molecular Bioengineering* **2013,** *6* (4), 383-392.

212. Sozański, K.; Ruhnow, F.; Wiśniewska, A.; Tabaka, M.; Diez, S.; Hołyst, R., Small crowders slow down kinesin-1 stepping by hindering motor domain diffusion. *Physical review letters* **2015,** *115* (21), 218102.

213. Cassimeris, L.; Pryer, N. K.; Salmon, E., Real-time observations of microtubule dynamic instability in living cells. *The Journal of Cell Biology* **1988,** *107* (6), 2223-2231.

214. Howard, J.; Hyman, A. A., Growth, fluctuation and switching at microtubule plus ends. *Nature Reviews Molecular Cell Biology* **2009,** *10* (8), 569.

215. Mandelkow, E.-M.; Mandelkow, E.; Milligan, R. A., Microtubule dynamics and microtubule caps: a time-resolved cryo-electron microscopy study. *The Journal of cell biology* **1991,** *114* (5), 977-991.

216. Jordan, A.; Hadfield, J. A.; Lawrence, N. J.; McGown, A. T., Tubulin as a target for anticancer drugs: agents which interact with the mitotic spindle. *Medicinal research reviews* **1998,** *18* (4), 259-296.

217. Jordan, M. A.; Wilson, L., Microtubules as a target for anticancer drugs. *Nature Reviews Cancer* **2004,** *4* (4), 253.

218. Gascoigne, K. E.; Taylor, S. S., How do anti-mitotic drugs kill cancer cells? *Journal of cell science* **2009,** *122* (15), 2579-2585.

219. Keates, R. A., Effects of glycerol on microtubule polymerization kinetics. *Biochemical and biophysical research communications* **1980,** *97* (3), 1163-1169.

220. Himes, R. H.; Burton, P. R.; Gaito, J., Dimethyl sulfoxide-induced self-assembly of tubulin lacking associated proteins. *Journal of Biological Chemistry* **1977,** *252* (17), 6222-6228.

221. Robinson, J.; Engelborghs, Y., Tubulin polymerization in dimethyl sulfoxide. *Journal of Biological Chemistry* **1982,** *257* (10), 5367-5371.

222. Algaier, J.; Himes, R. H., The effects of dimethyl sulfoxide on the kinetics of tubulin assembly. *Biochimica et Biophysica Acta (BBA)-Protein Structure and Molecular Enzymology* **1988,** *954*, 235-243.

223. Fenimore, P.; Frauenfelder, H.; McMahon, B.; Young, R., Proteins are paradigms of stochastic complexity. *Physica A: Statistical Mechanics and its Applications* **2005,** *351* (1), 1-13.

224. Fenimore, P. W.; Frauenfelder, H.; McMahon, B. H.; Parak, F. G., Slaving: solvent fluctuations dominate protein dynamics and functions. *Proceedings of the National Academy of Sciences* **2002,** *99* (25), 16047-16051.

225. Ebbinghaus, S.; Kim, S. J.; Heyden, M.; Yu, X.; Heugen, U.; Gruebele, M.; Leitner, D. M.; Havenith, M., An extended dynamical hydration shell around proteins. *Proceedings of the National Academy of Sciences* **2007,** *104* (52), 20749-20752.

226. Bellissent-Funel, M.-C.; Hassanali, A.; Havenith, M.; Henchman, R.; Pohl, P.; Sterpone, F.; van der Spoel, D.; Xu, Y.; Garcia, A. E., Water determines the structure and dynamics of proteins. *Chemical reviews* **2016,** *116* (13), 7673-7697.

227. Pokorný, J.; Hašek, J.; Jelínek, F., Electromagnetic field of microtubules: effects on transfer of mass particles and electrons. *Journal of Biological Physics* **2005,** *31* (3-4), 501-514.

228. Pokorný, J., Excitation of vibrations in microtubules in living cells. *Bioelectrochemistry* **2004,** *63* (1-2), 321-326.

229. Sahu, S.; Ghosh, S.; Fujita, D.; Bandyopadhyay, A., Live visualizations of single isolated tubulin protein self-assembly via tunneling current: effect of electromagnetic pumping during spontaneous growth of microtubule. *Scientific Reports* **2014,** *4*, 7303.

230. Behrens, S.; Wu, J.; Habicht, W.; Unger, E., Silver nanoparticle and nanowire formation by microtubule templates. *Chemistry of materials* **2004,** *16* (16), 3085-3090.

231. Haghshenas, E.; Madrakian, T.; Afkhami, A.; Nabiabad, H. S., A label-free electrochemical biosensor based on tubulin immobilized on gold nanoparticle/glassy carbon electrode for the determination of vinblastine. *Analytical and bioanalytical chemistry* **2017,** *409* (22), 5269-5278.

232. Kerssemakers, J. W.; Munteanu, E. L.; Laan, L.; Noetzel, T. L.; Janson, M. E.; Dogterom, M., Assembly dynamics of microtubules at molecular resolution. *Nature* **2006,** *442* (7103), 709.

233. Mozziconacci, J.; Sandblad, L.; Wachsmuth, M.; Brunner, D.; Karsenti, E., Tubulin dimers oligomerize before their incorporation into microtubules. *PLoS One* **2008,** *3* (11), e3821.

234. Giambaşu, G. M.; Luchko, T.; Herschlag, D.; York, D. M.; Case, D. A., Ion counting from explicit-solvent simulations and 3D-RISM. *Biophysical journal* **2014,** *106* (4), 883-894.

235. Andreu, J. M.; Timasheff, S. N., Tubulin bound to colchicine forms polymers different from microtubules. *Proceedings of the National Academy of Sciences* **1982,** *79* (22), 6753-6756.

236. Bordas, J.; Mandelkow, E.-M.; Mandelkow, E., Stages of tubulin assembly and disassembly studied by time-resolved synchrotron X-ray scattering. *Journal of molecular biology* **1983,** *164* (1), 89-135.

237. Krouglova, T.; Vercammen, J.; Engelborghs, Y., Correct diffusion coefficients of proteins in fluorescence correlation spectroscopy. Application to tubulin oligomers induced by Mg2+ and Paclitaxel. *Biophysical journal* **2004,** *87* (4), 2635-2646.

238. Pearlman, D. A.; Case, D. A.; Caldwell, J. W.; Ross, W. S.; Cheatham III, T. E.; DeBolt, S.; Ferguson, D.; Seibel, G.; Kollman, P., AMBER, a package of computer programs for applying molecular mechanics, normal mode analysis, molecular dynamics and free energy calculations to simulate the structural and energetic properties of molecules. *Computer Physics Communications* **1995,** *91* (1-3), 1-41.

239. Smilgies, D.-M.; Folta-Stogniew, E., Molecular weight–gyration radius relation of globular proteins: a comparison of light scattering, small-angle X-ray scattering and structure-based data. *Journal of applied crystallography* **2015,** *48* (5), 1604-1606.

240. Looyenga, H., Dielectric constants of heterogeneous mixtures. *Physica* **1965,** *31* (3), 401-406.

241. Wieczorek, M.; Bechstedt, S.; Chaaban, S.; Brouhard, G. J., Microtubule-associated proteins control the kinetics of microtubule nucleation. *Nature cell biology* **2015,** *17* (7), 907.

242. Wilson, L., Action of drugs on microtubules. *Life sciences* **1975,** *17* (3), 303-309.

243. Capriotti, K.; Capriotti, J. A., Dimethyl sulfoxide: history, chemistry, and clinical utility in dermatology. *The Journal of clinical and aesthetic dermatology* **2012,** *5* (9), 24.

244. Smith, R., A comprehensive macrophage-T-lymphocyte theory of schizophrenia. *Medical hypotheses* **1992,** *39* (3), 248-257.

245. Salim, A. S., Role of oxygen-derived free radical scavengers in the management of recurrent attacks of ulcerative colitis: a new approach. *The Journal of laboratory and clinical medicine* **1992,** *119* (6), 710-717.

246. Salim, A. S., Allopurinol and dimethyl sulfoxide improve treatment outcomes in smokers with peptic ulcer disease. *Translational Research* **1992,** *119* (6), 702-709.

247. Deng, R.; Wang, S.-m.; Yin, T.; Ye, T.-h.; Shen, G.-b.; Li, L.; Zhao, J.-y.; Sang, Y.-x.; Duan, X.-g.; Wei, Y.-q., Dimethyl sulfoxide suppresses mouse 4T1 breast cancer growth by modulating tumor-associated macrophage differentiation. *Journal of breast cancer* **2014,** *17* (1), 25-32.

248. Goto, I.; Yamamoto-Yamaguchi, Y.; Honma, Y., Enhancement of sensitivity of human lung adenocarcinoma cells to growth-inhibitory activity of interferon alpha by differentiation-inducing agents. *British journal of cancer* **1996,** *74* (4), 546.

249. Kim, Y. S.; Tsao, D.; Siddiqui, B.; Whitehead, J. S.; Arnstein, P.; Bennett, J.; Hicks, J., Effects of sodium butyrate and dimethylsulfoxide on biochemical properties of human colon cancer cells. *Cancer* **1980,** *45* (S5), 1185-1192.

250. Cyran, C. C.; Sennino, B.; Chaopathomkul, B.; Fu, Y.; Rogut, V.; Shames, D. M.; Wendland, M. F.; McDonald, D. M.; Brasch, R. C., Magnetic resonance imaging assays for dimethyl sulfoxide effect on cancer vasculature. *Investigative radiology* **2008,** *43* (5), 298.

251. Wang, F.; He, L.; Dai, W.-Q.; Xu, Y.-P.; Wu, D.; Lin, C.-L.; Wu, S.-M.; Cheng, P.; Zhang, Y.; Shen, M., Salinomycin inhibits proliferation and induces apoptosis of human hepatocellular carcinoma cells in vitro and in vivo. *PloS one* **2012,** *7* (12), e50638.

252. Memet, E.; Hilitski, F.; Morris, M. A.; Schwenger, W. J.; Dogic, Z.; Mahadevan, L., Microtubules soften due to cross-sectional flattening. *Elife* **2018,** *7*, e34695.

253. Deriu, M. A.; Soncini, M.; Orsi, M.; Patel, M.; Essex, J. W.; Montevecchi, F. M.; Redaelli, A., Anisotropic elastic network modeling of entire microtubules. *Biophysical journal* **2010,** *99* (7), 2190-2199.

254. Dogterom, M.; Yurke, B., Measurement of the force-velocity relation for growing microtubules. *Science* **1997,** *278* (5339), 856-860.

255. van den Heuvel, M. G.; Butcher, C. T.; Smeets, R. M.; Diez, S.; Dekker, C., High rectifying efficiencies of microtubule motility on kinesin-coated gold nanostructures. *Nano Letters* **2005,** *5* (6), 1117-1122.

256. Fischer, T.; Agarwal, A.; Hess, H., A smart dust biosensor powered by kinesin motors. *Nature nanotechnology* **2009,** *4* (3), 162.

257. Groß, H.; Heil, H. S.; Ehrig, J.; Schwarz, F. W.; Hecht, B.; Diez, S., Parallel mapping of optical near-field interactions by molecular motor-driven quantum dots. *Nature nanotechnology* **2018,** *13* (8), 691-695.

258. Chaudhuri, S.; Korten, T.; Korten, S.; Milani, G.; Lana, T.; te Kronnie, G.; Diez, S., Label-Free Detection of Microvesicles and Proteins by the Bundling of Gliding Microtubules. *Nano Letters* **2018,** *18* (1), 117-123.

259. Lin, C.-T.; Kao, M.-T.; Kurabayashi, K.; Meyhofer, E., Self-contained, biomolecular motor-driven protein sorting and concentrating in an ultrasensitive microfluidic chip. *Nano Letters* **2008,** *8* (4), 1041-1046.

260. Liu, J.-H.; Hsia, K.-C.; Yokokawa, R.; Lu, Y.-W., Microtubule polymerization in alignment by an on-chip temperature gradient platform. *Sensors and Actuators B: Chemical* **2019,** *298*, 126813.

261. Farhana, T. I.; Kaneko, T.; Yokokawa, R. In *The Cooperative Motility of Microtubules on Nano-Patterned Kinesin-1 Turf*, 2019 20th International Conference on Solid-State Sensors, Actuators and Microsystems & Eurosensors XXXIII (TRANSDUCERS & EUROSENSORS XXXIII), IEEE: 2019; pp 1056-1058.

262. Kaneko, T.; Furuta, K. y.; Oiwa, K.; Shintaku, H.; Kotera, H.; Yokokawa, R., Different motilities of microtubules driven by kinesin-1 and kinesin-14 motors patterned on nanopillars. *Science Advances* **2020,** *6* (4), eaax7413.

263. Nicolau, D. V.; Lard, M.; Korten, T.; van Delft, F. C.; Persson, M.; Bengtsson, E.; Månsson, A.; Diez, S.; Linke, H., Parallel computation with molecular-motor-propelled agents in nanofabricated networks. *Proceedings of the National Academy of Sciences* **2016,** *113* (10), 2591-2596.

264. Nogales, E.; Wolf, S. G.; Downing, K. H., Erratum: Structure of the αβ tubulin dimer by electron crystallography. *Nature* **1998,** *393* (6681), 191-191.

265. Tuszynski, J. A.; Carpenter, E. J.; Huzil, J. T.; Malinski, W.; Luchko, T.; Luduena, R. F., The evolution of the structure of tubulin and its potential consequences for the role and function of microtubules in cells and embryos. *International Journal of Developmental Biology* **2006,** *50* (2/3), 341.

266. Sheliakina, M.; Mostert, A. B.; Meredith, P., Decoupling ionic and electronic currents in melanin. *Advanced Functional Materials* **2018,** *28* (46), 1805514.

267. Kvakovszky, G.; McKim, A.; Moore, J. C., A review of microelectronic manufacturing applications using DMSO-based chemistries. *ECS transactions* **2007,** *11* (2), 227-234.

268. WAXMAN, P. G.; DEL CAMPO, A. A.; LOWE, M. C.; HAMEL, E., Induction of Polymerization of Purified Tubulin by Sulfonate Buffers: Marked Differences between 4-Morpholineethanesulfonate (Mes) and 1, 4-Piperazineethanesulfonate (Pipes). *European journal of biochemistry* **1981,** *120* (1), 129-136.

269. Rossini, E.; Netz, R. R.; Knapp, E.-W., Computing p K a Values in Different Solvents by Electrostatic Transformation. *Journal of chemical theory and computation* **2016,** *12* (7), 3360-3369.

270. Rossini, E.; Bochevarov, A. D.; Knapp, E. W., Empirical Conversion of p K a Values between Different Solvents and Interpretation of the Parameters: Application to Water, Acetonitrile, Dimethyl Sulfoxide, and Methanol. *ACS omega* **2018,** *3* (2), 1653-1662.

271. Fang, R.; Jing, H.; Chai, Z.; Zhao, G.; Stoll, S.; Ren, F.; Liu, F.; Leng, X., Design and characterization of protein-quercetin bioactive nanoparticles. *Journal of nanobiotechnology* **2011,** *9* (1), 19.

272. Ellis, R. J.; Minton, A. P., Join the crowd. *Nature* **2003,** *425* (6953), 27-28.

273. Junker, N. O.; Vaghefikia, F.; Albarghash, A.; Höfig, H.; Kempe, D.; Walter, J.; Otten, J.; Pohl, M.; Katranidis, A.; Wiegand, S., Impact of Molecular Crowding on Translational Mobility and Conformational Properties of Biological Macromolecules. *The Journal of Physical Chemistry B* **2019,** *123* (21), 4477-4486.

274. Roosen-Runge, F.; Hennig, M.; Zhang, F.; Jacobs, R. M.; Sztucki, M.; Schober, H.; Seydel, T.; Schreiber, F., Protein self-diffusion in crowded solutions. *Proceedings of the National Academy of Sciences* **2011,** *108* (29), 11815-11820.

275. Rivas, G.; Minton, A. P., Macromolecular crowding in vitro, in vivo, and in between. *Trends in biochemical sciences* **2016,** *41* (11), 970-981.

276. Kuznetsova, I. M.; Turoverov, K. K.; Uversky, V. N., What macromolecular crowding can do to a protein. *International journal of molecular sciences* **2014,** *15* (12), 23090-23140.

277. Kumar, P.; Boukherroub, R.; Shankar, K., Sunlight-driven water-splitting using two-dimensional carbon based semiconductors. *Journal of Materials Chemistry A* **2018,** *6* (27), 12876-12931.

278. Haskins, K. M.; Zombola, R. R.; Boling, J. M.; Lee, Y. C.; Himes, R. H., Tubulin assembly induced by cobalt and zinc. *Biochemical and biophysical research communications* **1980,** *95* (4), 1703-1709.

279. Burton, P. R.; Himes, R. H., Electron microscope studies of pH effects on assembly of tubulin free of associated proteins. Delineation of substructure by tannic acid staining. *The Journal of cell biology* **1978,** *77* (1), 120-133.

280. LeBel, R. G.; Goring, D. A. I., Density, Viscosity, Refractive Index, and Hygroscopicity of Mixtures of Water and Dimethyl Sulfoxide. *Journal of Chemical & Engineering Data* **1962,** *7* (1), 100-101.

281. Yang, L.-J.; Yang, X.-Q.; Huang, K.-M.; Jia, G.-Z.; Shang, H., Dielectric Properties of Binary Solvent Mixtures of Dimethyl Sulfoxide with Water. *International Journal of Molecular Sciences* **2009,** *10* (3), 1261-1270.

282. Segur, J.; Association, G., Physical properties of glycerine and its solutions. *Aciscience. Org* **1953**, 1-27.

283. Ott, C.; Reiter, F.; Baumgartner, M.; Pielmeier, M.; Vogel, A.; Walke, P.; Burger, S.; Ehrenreich, M.; Kieslich, G.; Daisenberger, D., Flexible and Ultrasoft Inorganic 1D Semiconductor and Heterostructure Systems Based on SnIP. *Advanced Functional Materials* **2019,** *29* (18), 1900233.

284. Wang, Y.; Di, Y.; Antonietti, M.; Li, H.; Chen, X.; Wang, X., Excellent Visible-Light Photocatalysis of Fluorinated Polymeric Carbon Nitride Solids. *Chemistry of Materials* **2010,** *22* (18), 5119-5121.